ROYAL SOCIETY
OF CHEMISTRY

REVIEW ARTICLE

Check for updates

Towards high performance and durable soft tactile actuators

Matthew Wei Ming Tan,[ab] Hui Wang,[a] Dace Gao,[a] Peiwen Huang[a] and Pooi See Lee [ID] *[ab]

Soft actuators are gaining significant attention due to their ability to provide realistic tactile sensations in various applications. However, their soft nature makes them vulnerable to damage from external factors, limiting actuation stability and device lifespan. The susceptibility to damage becomes higher with these actuators often in direct contact with their surroundings to generate tactile feedback. Upon onset of damage, the stability or repeatability of the device will be undermined. Eventually, when complete failure occurs, these actuators are disposed of, accumulating waste and driving the consumption of natural resources. This emphasizes the need to enhance the durability of soft tactile actuators for continued operation. This review presents the principles of tactile feedback of actuators, followed by a discussion of the mechanisms, advancements, and challenges faced by soft tactile actuators to realize high actuation performance, categorized by their driving stimuli. Diverse approaches to achieve durability are evaluated, including self-healing, damage resistance, self-cleaning, and temperature stability for soft actuators. In these sections, current challenges and potential material designs are identified, paving the way for developing durable soft tactile actuators.

1. Introduction

The sense of touch shapes our daily interaction with the world, allowing us to experience textures, pressure, vibrations, temperature, and even pain. The importance of tactile sensations became more apparent after the COVID-19 pandemic, as touch plays a vital role in social and emotional communication.[1] Recognizing the significance of touch, there is a growing interest in developing devices that provide tactile feedback, going beyond typical audio and visual cues to convey information. However, many of these devices use rigid tactile actuators.[2] These actuators differ from the soft and compliant nature of our skin, making it difficult to transmit realistic tactile sensations. Additionally, their size and bulkiness limit their practicality for wearables.[3]

In response to these challenges, soft tactile actuators have emerged as a promising solution. These actuators share similar properties with soft biological materials with moduli ranging from 10^4 to 10^9 Pa and often utilize materials such as fluids, hydrogels, elastomers, and plastic films.[4] Their compliant nature allows them to interact safely with the human body

and adapt to their environment, leading to success in recreating realistic tactile sensations. Owing to these features, soft tactile actuators have attracted attention in various fields, including healthcare, virtual reality, augmented reality, robotics, and wearables.[2,3,5–8]
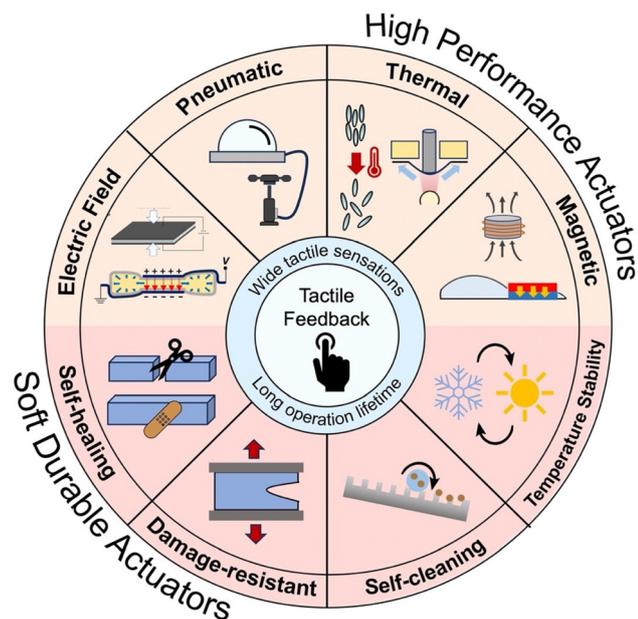
Nevertheless, a critical issue in the practical application of these soft tactile actuators is their durability.[9] Here, durability is referred to as the ability to withstand operational failure. Due to their soft nature, these actuators are prone to premature failures caused by factors like overloading, punctures, tears, and cuts from external sources.[9,10] This vulnerability is particularly concerning since tactile actuators are in constant direct contact with their external environment. Furthermore, environmental factors like moisture, dust, and temperature could compromise their long-term use, affecting their actuation performance stability.[11–13] These factors may easily be encountered in common scenarios such as sweaty hands, humid environments, poor storage conditions, and changing seasons. When these actuators fail, they are often discarded, contributing to electronic waste and the depletion of resources required for manufacturing. Thus, as industries move towards circular economy practices to minimize waste, designing soft and durable tactile actuators becomes critically important.[14] This remains challenging as the pursuit of durability may compromise their soft features and actuation capabilities.

In this review, we present strategies of fabricating soft tactile actuators with both high performance and durability

a School of Materials Science and Engineering, Nanyang Technological University, 50 Nanyang Avenue, Singapore, 639798, Singapore. E-mail: pslee@ntu.edu.sg

b Singapore-HUJ Alliance for Research and Enterprise (SHARE), Smart Grippers for Soft Robotics (SGSR), Campus for Research Excellence and Technological Enterprise (CREATE), Singapore, 138602, Singapore

This journal is © The Royal Society of Chemistry 2024

Chem. Soc. Rev., 2024, **53**, 3485–3535 | **3485**

Scheme 1 Summary of this review to achieve high performance and durable soft tactile actuators.

(Scheme 1). The scope of the study will focus on actuators that create tactile sensations by applying mechanical stimuli to the skin. We start by exploring the fundamental principles behind human tactile sensations, and then use that knowledge to establish the performance criteria for soft tactile actuators. Moving forward, we discuss the mechanisms, advancements, and strategies for enhancing the performance of soft tactile actuators, categorized according to the primary driving stimuli that drive them. To make soft tactile actuators more durable, we evaluate material and design approaches that enable self-healing, damage resistance, self-cleaning, and temperature stability. Concluding our review, we offer insights into recent advancements that can potentially enhance these soft and durable tactile actuators. To our knowledge, this review is the first comprehensive evaluation of soft tactile actuators that distinctively emphasize on durability. Thus, the scope of this review differs from those that are focused on soft robotics,[4,15] haptic devices,[2,7] and designing soft materials with self-healing capabilities or extreme mechanical properties.[10,16,17] With the aim of addressing the common challenges in designing better soft actuators to meet real-world conditions,[9] our review provides in-depth evaluation of the material and design strategies to achieve high performance and durability for tactile soft actuators. We hope this review will derive new ideas to advance the field and encourage collaboration between researchers working on materials and devices.

2. Overview of tactile feedback

2.1 Anatomical origin of tactile sensation

The numerous mechanoreceptors in our skin mediate human tactile sensation.[18] From the anatomical point of view (Fig. 1a),

a mechanoreceptor is a morphologically specialized and stress-responsive receptor that is typically located at the peripheral axon terminal of a sensory neuron (dorsal root ganglion). Tactile sensing relies on the mechano-responsive ion channels on the sensory axon terminal that rapidly transduce mechanical inputs into electrical signals.[19] When a mechanical stimulus deforms a receptor, the mechano-coupling between the receptor and the enclosed axon terminal causes the terminal to depolarize. An action potential is generated and transmitted along the primary afferent axon until reaching the central nervous system (spinal cord and brain). In a real-world touch event, numerous mechanoreceptors at the touch site would be activated, and the signals would be integrated to form a conscious sensation in the brain.

Human skin is either hairy or glabrous. Hair skin covers most of the human body, while glabrous skin, having the highest density of mechanoreceptors, covers the palmar surface of our hands and feet. Most state-of-the-art haptic devices are designed to be worn on hands or around fingers,[2] as we use them most frequently when exploring the external world. The presence of fingerprints, or the array of papillary ridges, also plays a role in enhancing and amplifying tactile sensations.[20] Wearable haptic devices targeting larger skin areas and featuring the coverage of hairy skin have also been developed,[21,22] enhancing the immersiveness of virtual reality (VR). The glabrous skin of humans (*e.g.*, palm/finger skin) contains four types of mechanoreceptors (Fig. 1e), with each type specialized in its morphology, innervated neuron type, and spatial distribution in the skin sublayers (epidermis, dermis, and subcutaneous tissue). Consequently, these mechanoreceptors respond to mechanical stimuli in different neural spiking submodalities,[23] which in concert allow us to perceive complex tactile information that intermixes pressure, motion, vibration, and texture. Here, we briefly describe the morphology and stimulus responsiveness of these mechanoreceptors to reveal how these factors can have an influence on the design of haptic actuators. Readers may refer to biological literature for greater details on human tactile perception.[24]

2.2 Classification of mechanoreceptors

Four primary types of mechanoreceptors reside within the glabrous skin: Merkel disks, Meissner corpuscles, Ruffini endings, and Pacinian corpuscles. These mechanoreceptors exhibit different time-domain spiking patterns in response to mechanical stimuli. They are broadly classified as slow-adapting (SA) and rapid-adapting (RA) afferents (Fig. 1b). SA afferents are capable of continuously firing action potentials under steady stress conditions, such as normal pressure or lateral stretch. Also, the firing frequency positively correlates with the applied stress level (Fig. 1c).[25,26] SA afferents mainly detect static skin deformations, allowing the identification of the object shape, surface texture, and hardness upon contact. In contrast, RA afferents quickly adapt to constant stimuli, generating spikes solely during transient moments of stress variation. This renders them sensitive to motion and vibration yet unresponsive to constant stress. For vibrational sensations, a RA afferent would
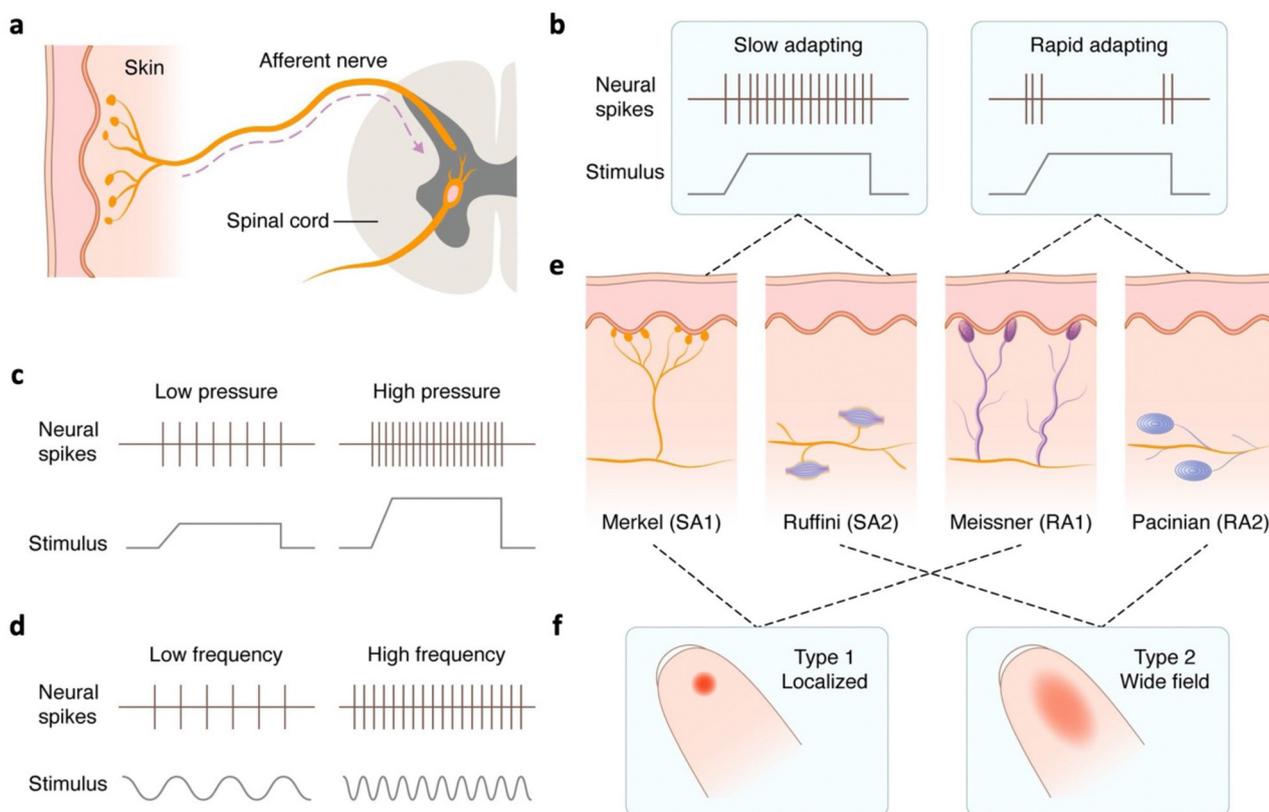
3486 | *Chem. Soc. Rev.*, 2024, **53**, 3485–3535

This journal is © The Royal Society of Chemistry 2024

Fig. 1 Anatomical origin of tactile sensation. (a) Neural signalling pathway from mechanoreceptors to the central nervous system. (b) Spiking patterns of slow and rapid adapting mechanoreceptors. (c) Firing frequency of slow adapting (SA) receptors under different pressure levels. (d) Firing frequency of rapid adapting (RA) receptors under different vibrational frequency. (e) Schematic illustrations of the four major mechanoreceptors. (f) Receptive fields of type 1 and type 2 receptors.

spike in synchrony with the vibration (one spike signaling one vibrating cycle, Fig. 1d). The firing rate of RA and SA spikes serves as an essential cue for tactile perception. The differing adaptation rates can be due to the different ion-channel-activation modes in the axon terminals.

Mechanoreceptors are also classified according to their receptive fields (Fig. 1f). This refers to the specific skin area where a receptor responds to mechanical stimulus and conveys a neural response. Type 1 afferents are distinguished by their small receptive fields and dense skin innervation.[27] They are situated below the surface of the skin, specifically within the boundary between the epidermis and dermis, at depths less than 1 mm. These attributes impart tactile acuity to type 1 afferents to convey neural images of surface events at high spatial resolutions.[27,28] In contrast, Type 2 afferents possess larger receptive fields, resulting in transmitted information having a more global nature. These receptors are typically embedded deeply within the skin in the dermal and subcutaneous layers.[29]

Merkel disks, classified as slow-adapting type 1 (SA1) afferents, are located in the basal layer of the epidermis, and innervate the skin densely. SA1 afferents yield pressure-like sensations in response to static or slowly moving stimuli. In particular, their sensitivity to specific sections of the local stress–strain field endows them with sensitivity to points,

edges, and curvatures.[27,30] Individual SA1 receptors can resolve spatial details as fine as 0.5 mm and exhibit a linear response with indentation depths up to 1.5 mm. Owing to these attributes, SA1 receptors are often associated with form and texture perception.[27] Meissner corpuscles, characterized as rapid-adapting type 1 (RA1) afferents, are at the dermal papillae. In comparison to SA1 receptors, RA1 afferents densely innervate the skin (approximately 150 per cm^2 at the fingertips) and demonstrate heightened sensitivity to dynamic skin deformations. Notably, RA1 afferents excel in detecting and discriminating at low frequencies, exhibiting optimal responses within the 30 to 60 Hz range.[31,32] Heights of 2 mm can be detected on a flat surface when there is movement between the skin and surface.[30] This allows RA1 afferents to sense minute skin motions effectively, facilitating the detection of slippage and sudden changes in loading essential for grip control.[27] Slow-adapting type 2 (SA2) afferents, or Ruffini endings, possess large receptive fields with indistinct borders.[27] Although they exhibit approximately six times lower skin indentation sensitivity compared to SA1 afferents, SA2 afferents demonstrate higher sensitivity (two to four times higher) to skin stretching. Working with muscle spindles and joint afferents, SA2 afferents contribute to perceiving hand motions.[27,30] Pacinian corpuscles, identified as rapid-adapting type 2 (RA2) afferents, reside within the deep layers of the dermis. They

This journal is © The Royal Society of Chemistry 2024

Chem. Soc. Rev., 2024, **53**, 3485–3535 | **3487**

display remarkable sensitivity to high-frequency vibrations, extending up to 1000 Hz (most sensitive between 200 and 300 Hz),[30,33] and can detect vibrations at the nanometer scale (approximately 10 nm in amplitude) at 200 Hz.[1] RA2 afferents enable responses to distant events through transmitted vibrations.[27] This vibratory sensation proves vital for tool utilization; for instance, when writing with a pen, vibrations from the pen tip are transmitted along the pen body and are detected by RA2 afferents to perceive the paper texture.

Given the intricate nature of tactile perception, mechanoreceptors often function in combination to execute tasks.[34,35] The perception of roughness across various textures relies on the combined contributions of SA1, RA1, and RA2 afferents, with coarse textures effectively resolved by SA1 afferents and fine features triggering RA1 and RA2 afferents.[35] Furthermore, in real world tasks such as object manipulation, mechanoreceptor responses change across stages from object contact and force loading to lifting and unloading. To create a tactile device that activates multiple mechanoreceptors for a diverse range of sensations, the integration of distinct actuating systems and modes is promising.

Whilst the tactile sensation of glabrous skin, particularly that of human hands, is essential for exploring the environment through touch, the hairy skin that covers 90% of the human body surface also plays a significant role in tactile sensation and is crucial for performing daily activities. The hairy skin contains all mechanoreceptors except for the Meissner corpuscles. Merkel cells (SA1) in hairy skin form small clusters known as touch domes, while Ruffini endings (SA2) and Pacinian corpuscles (RA2) have a similar morphology and spatial distribution to those in glabrous skin. It is important to note that the hairy skin contains proportionally fewer mechanoreceptors compared to smooth, glabrous skin, resulting in a lower level of sensitivity. While Meissner corpuscles are absent in hairy skin, RA2 tactile perception is instead mediated by innervated hair follicles.[36,37] Hair follicles are miniature organs where hair resides and are densely innervated by afferent nerve fibers. These fibers respond to hair movement when stimuli are applied and removed, indicating that they are rapid-adapting and not sensitive to static pressure. The different types of hair and their association with different nerve fibers have been discussed in previous literature in greater detail,[38–40] and are not the focus of this review. Other mechanoreceptors in hairy skin include the field receptors, which respond to skin movements, and the C-tactile nerve endings, which are relevant to pleasant sensations during slow stroking.

The difference in mechanoreceptor type and density between glabrous and hairy skin results in varying tactile sensing abilities. When designing a tactile actuator, it is important to consider the specific region of the body for which the actuator is intended and to tailor the design parameters to match the tactile sensing capabilities of that particular skin type and body part.

2.3 Implications for tactile actuator design

Comprehending the diverse spatiotemporal tactile sensing capabilities of mechanoreceptors provides pivotal insights for designing soft tactile actuators. One crucial parameter to address is the absolute threshold, denoting the minimal tactile stimulation required for an individual to perceive or detect a sensory input.[30] The absolute threshold establishes the minimum performance level necessary for a soft tactile actuator. Furthermore, any operation signal noise from actuation is deemed acceptable only if it remains beneath this threshold. The fingertips and lips tend to have the highest tactile acuity, displaying lower thresholds than other body parts.[41,42] When subjected to static stimuli, the fingertip skin deformation, force, and pressure thresholds amount to 10 μm, 0.8 mN, and 0.2 N cm^{-2}, respectively. When permitted to move, the skin can discern surface structures of 0.85 μm height.[30] Upon exposure to dynamic stimuli, peak sensitivity emerges between 200 and 300 Hz, and the absolute threshold during normal stimulation varies from 0.1 to 0.2 μm.[30] To elicit tactile sensation in the hairy skin, a higher level of displacement and pressure will be required given the low density of mechanoreceptors. However, the threshold of hairy skin has not been thoroughly explored and demands further research to guide the design and development of tactile actuators specifically tailored for use on hairy skin.

Tactile devices frequently incorporate arrays of actuators to transmit spatial information. Consequently, the just noticeable difference (JND) is significant in the device design. The JND signifies the smallest detectable difference in tactile stimulation perceivable by an individual.[30] In terms of force, this pertains to the augmentation amount an individual experiences before realizing that augmentation has occurred.[43,44] Notably, the two-point discrimination threshold determines the distance between two tactile stimulus points required for an individual to perceive them as separate and distinct. This threshold varies across body parts and is dominated by the size of receptive fields of SA1 afferents, with the fingertips exhibiting the smallest thresholds.[24] On average, humans can discriminate two points placed approximately 1–2 mm apart on their fingertips.[30] For the proximal and distal body parts (e.g. back, forearm, thigh, etc.), the threshold is as much as ∼40 mm due to the lower density of SA1 mechanoreceptors in hairy skin.[24]

In general, absolute thresholds and JNDs differ appreciably across various sources, and the values provided serve as design guidelines for soft tactile actuators. These thresholds can vary due to multiple factors, including temperature, age, and contact area.[41,45,46] In addition, the differences in the type and density of mechanoreceptors across different body regions lead to distinct tactile sensory thresholds, thus necessitating different design considerations for tactile actuators. For haptic devices intended for the glabrous fingertips and palms, a high density of tactile pixels and finely graded output force levels are essential, given the small JND of the fingertips. In this context, the maximum displacements and forces can be moderated. On the other hand, for haptic interfaces covering a large body area with hairy skin, the actuators should be capable of delivering larger forces and displacements, while the requirements for force and spatial resolution are less stringent. In summary,

3488 | Chem. Soc. Rev., 2024, 53, 3485–3535

This journal is © The Royal Society of Chemistry 2024

when designing these tactile devices, specific operating conditions, the intended user demographic, the targeting body regions, and indenter dimensions must be taken into account. Such considerations ensure that soft tactile devices are tailored for optimal performance and sensory experiences.

3. Soft tactile actuators

Soft actuators operate by exerting mechanical forces and displacements onto the skin. However, their inherent softness introduces a challenge, often resulting in limited force generation. Over time, innovative employment of soft materials and novel design concepts have promoted rapid advancements in soft tactile actuators, allowing them to be effectively used to generate a wide range of sensations. A diverse array of driving mechanisms have been harnessed for these actuators, including electric fields, air pressure, thermal stimuli, and magnetic fields. In this section, we discuss their working principles and advancements, and explore potential avenues for enhancing their performance further.

3.1 Electric field

Electrical stimulation to drive soft actuators for tactile feedback offers a high degree of control, allowing for modulation of signal phase, amplitude, and frequency.[47,48] This approach provides significant advantages, as these electrically driven actuators can be integrated with commercial power sources and drivers, creating portable and untethered tactile devices. Generally, soft actuators driven by electrical stimulation can be categorized as electronic or ionic. Electronic actuators, where the primary driving force for actuation is generated by electric fields, encompass dielectric elastomer, electrohydraulic, piezoelectric, and electrostrictive actuators. The actuation performance of these electronic actuators designed for tactile feedback, typically requiring moderate to high applied voltages (10^2 to 10^4 V), is summarized in Table 1. On the other hand, ionic actuators, also called electrochemical actuators, operate effectively with lower voltage requirements ($<10^1$ V). This section highlights the working principles and progress of electrically stimulated actuators for tactile feedback, along with potential improvement strategies.

3.1.1 Dielectric elastomer actuators.
Dielectric elastomer actuators (DEAs) are comprised of a soft dielectric elastomer layer sandwiched between two compliant electrodes (Fig. 2a).[66] The region with two overlapping electrodes is the active region of DEAs. Upon applying an electric field, opposite charges accumulate on the electrodes, leading to their attraction due to the generated electrostatic pressure, also known as the Maxwell pressure (P). Actuation is achieved as the Maxwell pressure compresses the active region of the dielectric elastomer along the thickness direction, causing area expansion. Owing to their soft nature (elastic modulus below several MPa), DEAs can achieve safe tactile interactions with humans, as the mechanical impedance of DEAs matches that of human skin.[50] Notable advantage of these actuators includes high

actuation strains, wide frequency bandwidths, rapid response, low weight, easy miniaturization, and design flexibility.[67–69]

Actuation strain, a key performance indicator, correlates to the Maxwell pressure and the elastic modulus (Y) of dielectric elastomers. Along the thickness direction of dielectric elastomers, the actuation strain s_z is expressed as

$$s_z = -\frac{P}{Y} = -\frac{\varepsilon_0 \varepsilon_r E^2}{Y} \quad (3.1)$$

where ε_0, ε_r, and E are the vacuum permittivity, dielectric constant, and electric field, respectively. This implies that actuation strain can be elevated by increasing the dielectric constant and reducing the elastic modulus at a given electric field. DEAs offer a range of working modes, depending on their configurations.[70] Framed DEAs involve pre-straining the elastomer onto a rigid frame to achieve in-plane expansion. Diaphragm or buckling DEAs adopt planar constructions, utilizing a rigid ring or passive regions to limit area expansion, thereby achieving out-of-plane displacements. Unimorph DEAs, affixed to a flexible passive layer, achieve bending with voltage application.

DEAs have the potential to operate over a wide frequency range from 10^{-1} Hz to 10^4 Hz, aligning with the stimulation frequencies of mechanoreceptors.[71] Positive results of vibrotactile perception threshold tests evidence their suitability for tactile feedback.[72–74] The frequency bandwidth is influenced by the RC time constant of DEA charging and discharging as well as the viscoelastic response of dielectric elastomers.[66] The RC time constant refers to the product of the resistance and capacitance of the circuit. By using compliant electrodes with high conductivity, low RC constants are attained, at which the frequency bandwidth becomes limited by viscoelastic losses. Commonly employed very high bond (VHB) acrylic tapes tend to reach equilibrium actuation states around 0.1 Hz. However, due to high viscoelastic losses, these DEAs exhibit limited repeatability at frequencies exceeding several tens of Hz. In contrast, DEAs using silicone elastomers with low viscoelastic losses, like polydimethylsiloxane (PDMS), have demonstrated stable actuation at frequencies up to $\sim 10^4$ Hz, rendering them suitable for tactile feedback.[75] Despite these benefits, the dielectric constant of PDMS is low (2.5 to 3 at 1 kHz) and thus requires larger electric fields and voltages for actuation.[70] To broaden the choices of dielectric elastomers, strategies such as incorporating crosslinkers into elastomers, blending with carbon nanospring fillers, or introducing an elastic interlayer can be applied.[76–78] Huang et al. designed a DEA with low viscoelastic losses and high dielectric constants (18.9 at 1 kHz) by introducing cyanoethyl cellulose into plasticized PVC gels.[79] Low viscoelastic losses resulted from multiple molecular interactions, such as electrostatic interactions and hydrogen bonds that restricted chain mobility. The resultant elastomer exhibited minimal relative displacement shifts after 1000 cycles (7.78%), outperforming VHB (136.09%) and closely matching PDMS (5.70%).

In addition to the working frequency, voltage is an essential concern of DEA haptics. In pursuit of commercialization and

This journal is © The Royal Society of Chemistry 2024

Chem. Soc. Rev., 2024, **53**, 3485–3535 | **3489**

Table 1 Actuation performance of dielectric elastomer, electrohydraulic, piezoelectric, and electrostrictive actuators designed for tactile feedback

Actuator type	Dielectric material	Configuration	Maximum actuation displacement	Maximum blocking force	Operating frequency	Displacement at maximum frequency	Ref.
DEA	Silicone	Stacked (18 layers)	1.8 mm @ 3 kV, 10 Hz	~23 mN @ 3 kV, 10 Hz	0–300 Hz	~70 μm @ 2 kV	49
DEA	Silicone	Stacked (3 layers)	6 μm @ 0.45 kV, 10 Hz	~9 mN @ 0.45 kV, 10 Hz	1–500 Hz	~0.2 μm @ 0.45 kV	50
DEA	Silicone	Stacked (2 layers) with indenter	0.46 mm @ 4 kV, 245 Hz	8.48 N @ 4 kV, 304 Hz	0–400 Hz	~60 μm @ 4 kV	51
DEA	VHB 4905	Stacked (2 layers) with indenter	0.33 mm @ 4 kV, 0.1 Hz	6.79 N @ 4 kV, 321 Hz	0–400 Hz	~17 μm @ 4 kV	51
DEA	Silicone	Stacked (4 layers) with indenter	0.35 mm @ 6 kV, 1 Hz	150 mN @ 6 kV, 1 Hz	0.1–10 Hz	140 μm @ 6 kV	52
DEA	Silicone–ionic liquid composite	Stacked (900 layers)	0.16 mm @ 0.2 kV, DC	N. A	3–800 Hz	~12 μm @ 0.2 kV	53
DEA	Silicone–ionic liquid composite	Stacked (900 layers) with indenter	~0.15 mm @ 0.2 kV, 1 Hz	N. A	1–200 Hz	9.5 μm @ 0.2 kV	53
DEA	VHB 4910	Stacked (3 layers) with coupling fluid	3.5 mm @ 4 kV, DC	800 mN @ 0.7 kV, DC	N. A	N. A	54
DEA	Silicone	Rolled (7 turns of 10 layers stack)	~0.3 mm @ 1 kV, DC	~600 mN @ 1 kV, DC	0–300 Hz	~65 μm @ 1 kV	55
Electrohydraulic	P(VDF–TrFE–CTFE) and FR3 dielectric oil	PET and silicone shell; square seal; 3 mm inner diameter	0.36 mm @ 0.5 kV, 200 Hz bipolar square signal	300 mN @ 1.4 kV, 200 Hz bipolar square signal	0–200 Hz	~7 μm @ 1.4 kV	56
Electrohydraulic	P(VDF–TrFE–CTFE) and FR3 dielectric oil	PET and silicone shell; square seal; 2.5 mm inner diameter	0.5 mm @ 0.8 kV, 200 Hz bipolar square signal	160 mN @ 1.4 kV, 200 Hz bipolar square signal	0–200 Hz	100 μm @ 1.4 kV	56
Electrohydraulic	P(VDF–TrFE–CTFE) and FR3 dielectric oil	PET and silicone shell; square seal; 15 mm outer diameter	0.85 mm @ 1 kV, 200 Hz bipolar square signal	770 mN @ 1.3 kV, 200 Hz bipolar square signal	N. A	N. A	57
Electrohydraulic	Silicone and FR3 dielectric oil	Silicone shell, circular design	0.2 mm @ 4 kV, 100 Hz bipolar square signal	~22 mN @ 4 kV, 100 Hz bipolar square signal	1–1000 Hz	~22 μm	58
Electrohydraulic	Silicone and FR3 dielectric oil	Silicone shell, square design	~0.1 mm @ 4 kV, 100 Hz bipolar square signal	40 mN @ 4 kV, 100 Hz bipolar square signal	N. A	N. A	58
Electrohydraulic	BOPP and FR3 dielectric oil	Inner BOPP shell; outer silicone insulation	2.2 mm @ 8 kV, DC	~680 mN @ 8 kV, DC	N. A	N. A	59
Piezoelectric	Cellulose	Stacked (32 layers); unimorph	~82.5 μm @ 35 V, 0.1 Hz	N. A	0.1–10 Hz	75 μm @ 35 V	60
Piezoelectric	P(VDF–TrFE)–SWCNT composite	Unimorph (25 μm thick substrate)	5 mm @ 0.5 kV, 0.01 Hz	N. A	0.01–100 Hz	~360 μm @ 0.5 kV	61
Piezoelectric	P(VDF–TrFE)	Stacked (5 layers)	0.21 mm @ 50 V, 320 Hz	600 mN, @ 50 V, 320 Hz	N. A	N. A	62
Electrostrictive	P(VDF–TrFE–CFE) –P(VDF–TrFE) blend	Gap between dielectric and bottom electrode.	15.5 μm @ 0.2 kV, 1 Hz	N. A	1–500 Hz	1.6 μm @ 0.2 kV	63
Electrostrictive	P(VDF–TrFE–CTFE)	Unimorph (188 μm thick cover)	~2.2 μm @ 0.16 kV, 220 Hz	N. A	0–280 Hz	~0.2 μm @ 140 V	64
Electrostrictive	P(VDF–TrFE–CTFE)	Stacked (2 layers)	3.3 μm @ 0.1 kV, 220 Hz	N. A	N. A	N. A	64
Electrostrictive	P(VDF–TrFE–CFE) –P(VDF–CTFE) blend	Rolled (2 layers stack)	~0.8 mm @ 0.4 kV, DC	~1.8 N @ 0.5 kV, DC	N. A	N. A	65

~ : Estimated from figures; N.A.: not available; DEA: dielectric elastomer actuator; VHB: very high bond; DC: direct current. P(VDF–TrFE–CTFE): poly(vinylidene fluoride–trifluoroethylene–chlorotrifluoroethylene); PET: polyethylene terephthalate; BOPP: biaxially oriented polypropylene; P(VDF–TrFE): poly(vinylidene fluoride–trifluoroethylene); SWCNT: single walled carbon nanotube; P(VDF–TrFE–CFE): poly(vinylidene fluoride–trifluoroethylene–chlorofluoroethylene); P(VDF–CTFE): poly(vinylidene fluoride–trifluoroethylene–chlorofluoroethylene).
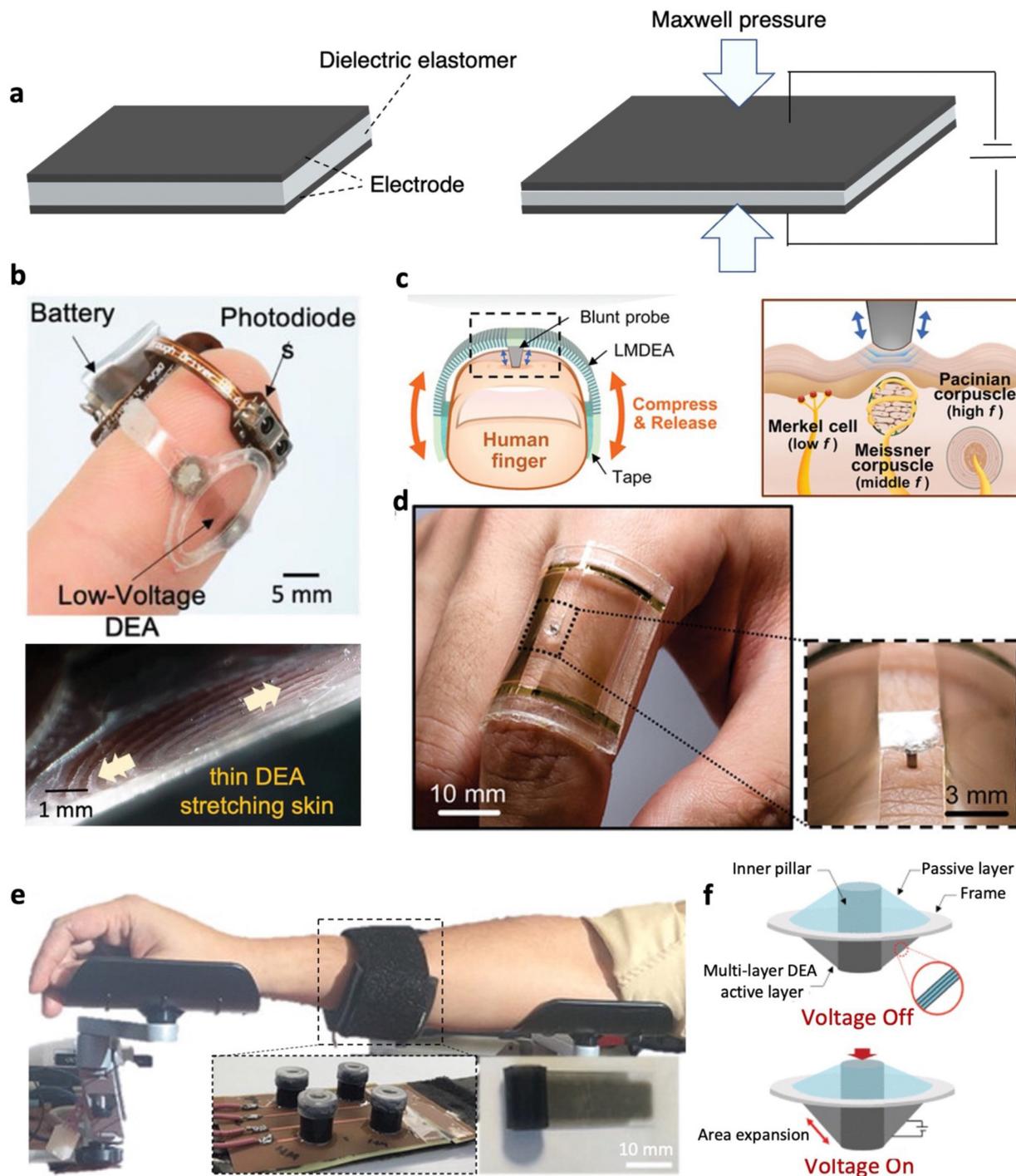
Fig. 2 Dielectric elastomer actuators (DEA) for tactile feedback. (a) Illustration of the working principle of DEAs. (b) Untethered ultrathin and lightweight DEA tactile device (top). Skin stretched by the DEA upon voltage application (bottom). Adapted with permission from ref. 50. Copyright 2020, Wiley-VCH. (c) Working principle of a vibrotactile device using two multilayer DEAs and a blunt probe for stimulating various mechanoreceptors. (d) Photograph of the vibrotactile device attached on a human finger. (c) and (d) Are adapted with permission from ref. 53. Copyright 2023, Wiley-VCH. (e) A wearable haptic communicator applied on the volunteer arm for location and direction identification. The communicator comprises a 2 × 2 array of rolled DEAs mounted onto a flexible circuit. Adapted with permission from ref. 55. Copyright 2020, Mary Ann Liebert, Inc. (f) Working principle of double-cone configured DEAs with a rigid indenter. Adapted from ref. 51 and published by IEEE under Creative Commons CC BY License.

portability, DEAs are expected to operate at lower voltages (below kV) while achieving actuation outputs sufficient for tactile feedback.[47] As such, extensive efforts have focused on enhancing the dielectric constant or reducing the elastic modulus of dielectric elastomers. Strategies include incorporating high-dielectric-constant fillers,[80,81] chemically modifying the

This journal is © The Royal Society of Chemistry 2024

Chem. Soc. Rev., 2024, 53, 3485–3535 | 3491

elastomer backbones,[82,83] adding plasticizers,[84,85] and thermally softening elastomers.[86] The detailed optimization methods and their influence have been discussed in reviews.[47,87] When tuning these parameters, the dielectric breakdown strength generally decreases, highlighting the need for careful optimization to balance actuation performance and dielectric breakdown. Strategies to prevent dielectric breakdown are discussed in Section 4.2.2.

Multilayer configurations are commonly employed to fulfil the demands of generating tactile feedback, which increases the overall Maxwell stresses and amplifies the capabilities of DEAs. Generally, two multilayer setups are employed for tactile devices: stacked and rolled configurations. Stacked DEAs are fabricated by vertically stacking numerous layers of dielectric elastomers and electrodes in series. Early works by Koo *et al.* led to the development of a wearable tactile display comprising eighteen silicone dielectric layers in diaphragm configurations, inducing out-of-plane displacements to generate tactile sensations.[49] Capitalizing on the simplicity of these configurations, a large DEA array (10 × 10) can be easily demonstrated. The device successfully met the tactile display requisites, delivering output displacements and forces of 1.8 mm and ∼23 mN, respectively, at 3 kV and 10 Hz. Subsequent refinement of the frequency performance of similar designs was further achieved by introducing a high voltage switching circuit that expedited discharging times, resulting in a twofold enhancement of displacements at 100 Hz.[88]

While these early demonstrations hold promise for tactile devices, they require high driving voltages that limit portability and risk dielectric breakdown. This may be addressed by reducing the thickness of individual layers within stacks.[47] For instance, Ji *et al.* presented an untethered, ultrathin (18 μm), and lightweight (1.3 g) DEA that produced vibrotactile sensations at the fingertip at relatively low voltages (Fig. 2b).[50] The tactile device, comprised of three stacked layers (each 6 μm thick), required 450 V to achieve actuation performances surpassing sensation thresholds. The ultrathin feature enabled the device to be mechanically transparent, enabling unrestricted finger movement and direct feeling of objects. Designed to be in skin contact, the DEA compressed the skin at rest. Upon voltage application, the DEA expanded, causing the skin to stretch and move perpendicularly to the DEA plane. Haptic testing on eleven volunteers affirmed the device efficacy, reporting identification rates from 73% to 97% at varying frequencies and waveforms. Nonetheless, manually stacking multiple layers for enhanced actuation output can be tedious, especially at reduced thickness. Instead, Son *et al.* utilized photolithography and secondary sputtering to achieve a multilayer DEA composed of 900 elastomer layers (PDMS blended with ionic liquid EMIM TFSI fillers, each layer measuring 10 μm in thickness).[53] Upon voltage application, the resultant Maxwell pressure on individual layers induced compression throughout the entire DEA. This design led to notable improvements, achieving lateral displacements of approximately 160 μm at 200 V (20 V μm^{-1}) and blocking forces up to 250 mN at 250 V (25 V μm^{-1}). The importance of material design is highlighted

as the addition of ionic liquid fillers provided a combination of low modulus and high dielectric constants that enabled high actuation displacements at the sensitive frequency (200 Hz) for vibration perception. The developed vibrotactile device comprised two multilayer DEAs (450 elastomer layers each) with a connecting probe, generating mechanical indentations on the skin (Fig. 2c and d). Measurements on a fingertip model indicated that actuation displacements at 200 V from 1 to 200 Hz were 5 to 15 times higher than perception thresholds. Moreover, the device displayed the capacity to operate with intricate tactile signals of varying amplitudes, frequencies, and patterns, implying its potential to encompass a broad spectrum of tactile sensations.

Rolled DEAs are fabricated by rolling multiple stacked layers into a cylindrical structure. Upon voltage application, the biaxial actuation is translated into linear motion along the cylinder's axial direction. The design relies on adequate friction and adhesion between individual layers to counteract unwinding and ensure that displacements occur along the axial direction. By adjusting factors like the number of turns, height, and thickness, force output can be amplified.[89,90] Zhao *et al.* performed such optimization, resulting in rolled DEAs producing free actuation displacements, blocking forces, and operating frequencies of up to 1 mm, 1 N, and 200 Hz, respectively.[90] Due to their suitability to stimulate less sensitive areas, such as the arm, these rolled DEA designs could be practically applied as a wearable haptic communicator (Fig. 2e).[55] The forearm comprised of a 2 × 2 rolled DEA array was employed for perception threshold and identification tests. During these tests, the DEA was randomly and sequentially triggered across a range of frequencies (10, 60, and 200 Hz), prompting volunteers to distinguish the location and direction of the actuation. The performance of the haptic communicator displayed considerable potential, achieving high identification accuracy rates of 82.8% (location) and 88.2% (direction).

For enhanced safety considerations, several works have integrated DEAs with rigid indenters, thus preventing direct contact between the skin and the actuator.[51,52] This design commonly involves positioning the indenter perpendicular to the plane of the dielectric elastomer. When voltage is applied, the area expansion of the DEA causes the indenter to retract. Subsequent removal of the voltage leads to the recovery of the DEA, pushing the indenter outward to contact the skin. Based on this principle, Youn *et al.* achieved a fingertip tactile device capable of applying a high force of 8.48 N at 304 Hz and 4 kV.[51] This was accomplished using double-cone geometries, where a two-layer Elastosil P7670 DEA and a passive layer were prestrained onto circular frames and then bonded with the indenter in between, forming a conical structure (Fig. 2f). The high force output was attributed to the use of rigid couplings, minimizing force losses. Additionally, for maximal tactile feedback, the mass of the indenter was adjusted to shift the resonance frequency of the device to around 250 Hz—the sensitive range for fingertip vibrations. These devices demonstrate the capability of DEAs to stimulate body parts or individuals with high perception thresholds.

3492 | *Chem. Soc. Rev.*, 2024, **53**, 3485–3535

This journal is © The Royal Society of Chemistry 2024

However, when the rigid indenter interfaces with the skin, the pressure distribution and skin deformation are inadequate to replicate compliance.[91] This implies that to mimic the softness of a virtual object, a soft interface between the tactile device and skin is required. Hydrostatically coupled DEAs have been proposed to address this, wherein actuation is transferred from the DEA to the passive layer in contact with the skin, facilitated by an insulating fluid such as sealing corn oil or silicone grease.[54,92,93] During actuation, lateral expansion is constrained due to the support of the rigid frame, causing the DEA to buckle outward while the passive layer moves inward *via* hydrostatic transmission. Another significant advantage of coupling with liquids is their ability to redistribute internal fluid when force is applied to the passive membrane. This ensures that the active DEA does not experience local changes in thickness from external forces that might promote dielectric breakdown. Efforts to enhance these hydrostatically coupled DEAs have included increasing the force output to 1 N through multilayer DEAs.[93] The size was also reduced to create a wearable tactile device suitable for multi-finger operations. Furthermore, the tactile device was integrated with commercial hand-tracking sensors, simulating virtual interactions with computer-generated objects. Psychophysical studies demonstrated the effectiveness of hydrostatically coupled DEAs for wearable tactile devices, with 15 volunteers successfully distinguishing between varying stimuli generated by the device.

While reducing the thickness of films has led to moderate driving voltages (200–1000 V), obtaining high forces and substantial displacements often necessitates the incorporation of multiple layers, a process that may be labour-intensive or require intricate procedures. The majority of these tactile actuators remain reliant on large high voltage power supplies, highlighting the need for more work that integrates DEAs with portable power sources, as demonstrated by Ji *et al.*[50] Achieving this would promote the application of DEAs for wearable tactile devices. Despite the high voltages being utilized, due to the low current being applied, low amount of power is consumed in the milliwatt range. DEAs have been designed with low modulus properties, which enable them to achieve large actuation strains. While this is advantageous, it comes with the drawback of increased susceptibility to external damage, which can result in premature failures. Hence, future works may focus on developing elastomers and designs that exhibit improved frequency response, demand lower voltage requirements, and prioritize durability. It is crucial to achieve a balance between these factors while ensuring that DEAs can deliver sufficient actuation force and displacement to simulate a diverse range of tactile feedback sensations effectively.

3.1.2 Electrohydraulic actuators. The structure and working principle of electrohydraulic actuators are similar to those of DEAs. Sandwiched between two electrodes, these actuators replace dielectric elastomers with dielectric fluids that are encapsulated within a flexible shell. Unlike DEAs, stretchable membranes and electrodes are not required, preventing performance degradation associated with strain.[94] When high voltages are applied, opposite charges on the electrodes attract

each other and generate electrostatic force, which compresses the dielectric fluid and its shell, redistributing the fluid (Fig. 3a). The electrostatic force (F) can be expressed as the following equation:[95]

$$F = \frac{\frac{1}{2}\varepsilon_0\varepsilon_{\text{medium}}AV^2}{\left(\frac{\varepsilon_{\text{medium}}}{\varepsilon_{\text{insulator}}}t_{\text{insulator}} + t_{\text{medium}}\right)^2} \tag{3.2}$$

where $\varepsilon_{\text{medium}}$ and $\varepsilon_{\text{insulator}}$ are the dielectric constant of the medium (dielectric fluid) and insulator (shell), respectively, at which t_{medium} and $t_{\text{insulator}}$ are their corresponding thickness. A is the active area of electrodes and V is the operating voltage. When $t_{\text{insulator}}$ is much lower than t_{medium}, $t_{\text{insulator}}$ can be omitted and eqn (3.2) can be simplified as

$$F = \frac{\frac{1}{2}\varepsilon_0\varepsilon_{\text{medium}}AV^2}{t_{\text{medium}}^2} \tag{3.3}$$

Hydraulically amplified self-healing electrostatic (HASEL) actuators, a type of electrohydraulic actuator, have garnered significant attention due to their impressive performance attributes, including high output force, power density, efficiency ($\sim 40\%$), and wide frequency bandwidth (~ 200 Hz).[94] Notably, when the operating voltage increases, there is a critical point known as the "pull-in transition" during which the electrostatic force overcomes the mechanical restoring force, leading to a rapid increase in actuation performance and pulling the electrodes together.[96] To mitigate pull-in instability, various electrohydraulic actuators have deviated from parallel electrode configurations and employed electrostatic zipping, with overlapping electrodes placed at the sides of the shell.[97,98] When voltages are applied, the electrodes are progressively drawn together in a zipping motion, starting from the sides where the electrodes are the closest and the electric fields are the highest. Subsequently, the dielectric liquid is displaced to regions without electrodes. Based on zipping mechanisms, electrohydraulic actuators have achieved rapid response, high actuation strains, and large force outputs.[98,99]

Given the performance capabilities of electrohydraulic actuators, they have found natural application in tactile devices. To improve mechanical transmission to the skin, Shao *et al.* designed a large area haptic display that provided increased skin contact (Fig. 3b).[59] By integrating six pairs of parallel hydrogel electrodes, static and dynamic patterns for tactile feedback can be obtained. For instance, activating the electrodes in sequence to move the liquid from one end to the other yielded directional tactile motions that volunteers could perceive. However, the use of an inextensible shell, such as biaxially oriented polypropylene (BOPP), may constrain actuation displacements. To address this limitation, hydraulically amplified taxels (HAXELs) comprised of a fluid-filled cavity enclosed by a shell composed of both stretchable and non-stretchable components were developed.[56] Large actuation displacement could be achieved as the stretchable elastomer made up the top central region meant to contact the skin. Voltage

This journal is © The Royal Society of Chemistry 2024

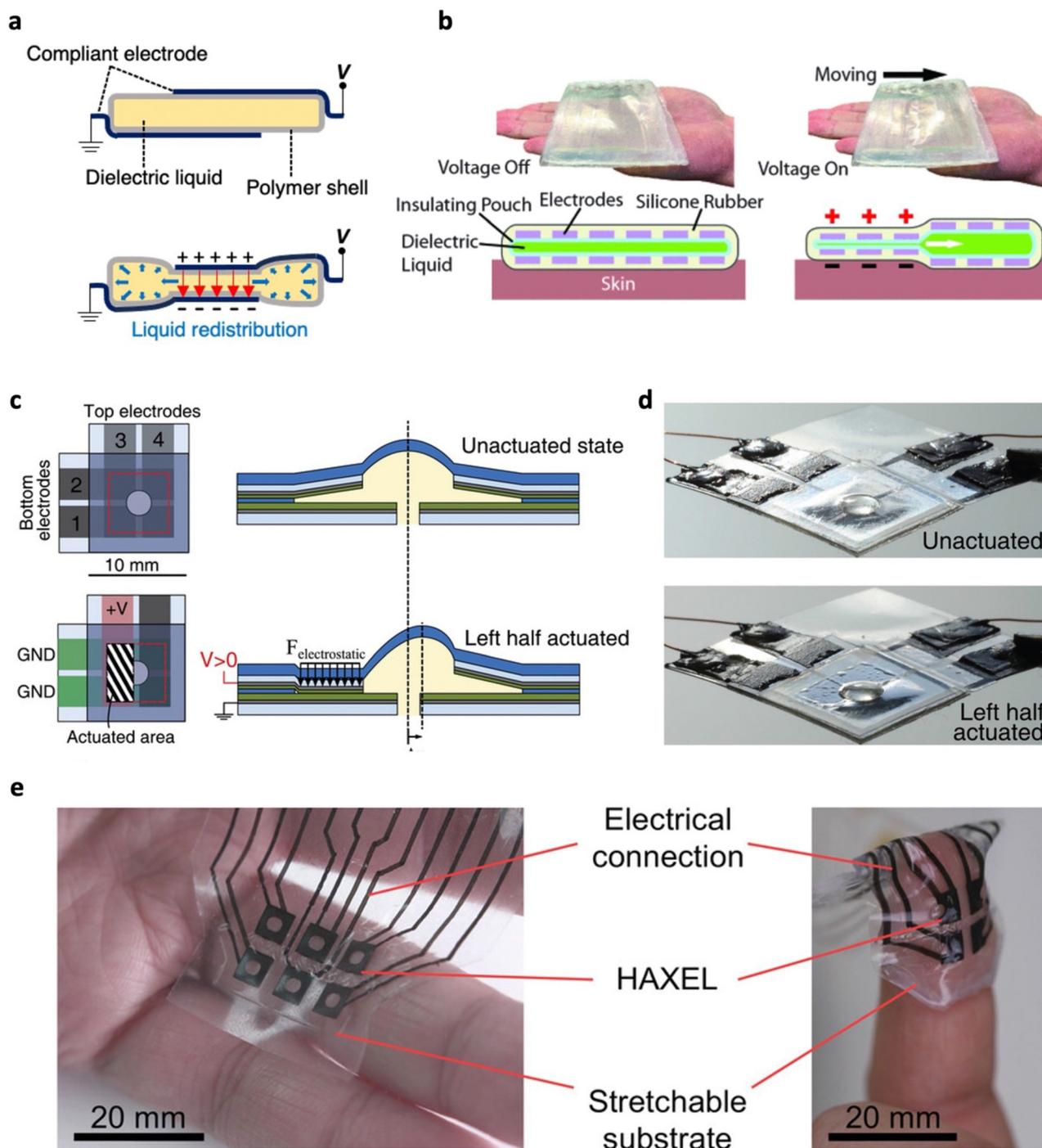*Chem. Soc. Rev.*, 2024, **53**, 3485–3535 | **3493**

Fig. 3 Electrohydraulic actuators for tactile feedback. (a) Illustration of the working principle of electrohydraulic actuators. (b) A large area haptic display consisting of electrohydraulic actuators and six pairs of hydrogel electrodes (top). Operating principle of the large area haptic display (bottom). Adapted with permission from ref. 59. Copyright 2020, IEEE. (c) Schematic and (d) photograph of selective activation of segregated electrodes which enables HAXEL actuators to generate in-plane motions. Left half of the electrodes were activated to shift the bump in the right direction. (c) and (d) Are adapted with permission from ref. 56. Copyright 2020, Wiley-VCH. (e) A fully printable, soft, and stretchable 2 × 3 array of HAXELs before and after mounting on the fingertip. Adapted from ref. 58 and published by Wiley-VCH under Creative Commons CC BY License.

application led to electrostatic zipping in non-stretchable regions, displacing the fluid into the central area and creating a raised bump. Furthermore, the incorporation of poly (vinylidene fluoride–trifluoroethylene–chlorotrifluoroethylene)

(P(VDF–TrFE–CTFE)) as the dielectric layer increased electrostatic pressure at a given voltage. By selectively activating segmented electrodes, both in-plane and out-of-plane displacements of the bump could be achieved (Fig. 3c and d). This

3494 | *Chem. Soc. Rev.*, 2024, **53**, 3485–3535

This journal is © The Royal Society of Chemistry 2024

enabled the transmission of shear and normal forces to users, broadening the range of sensations and applications, including texture recognition. HAXEL actuators demonstrated the ability to operate over a wide frequency range, achieving forces of 300 mN at 80 Hz and 100 μm at 200 Hz. Coupled with a rapid response time of less than 5 ms, these actuators exhibited great potential for wearable haptic devices characterized by minimal lag and realistic touch sensations. User tests further demonstrated their application, as participants accurately identified normal and shear forces with over 80% accuracy. Due to the highly thin form factor and flexible nature, 5 × 5 HAXEL arrays could be mounted onto the body. This concept was refined through fabrication process modifications for greater yield and performance.[57] 5 × 5 HAXEL arrays were tested on regions with different sensitivities (palm, back of hand, and the lower back), at which volunteers reported high average pattern recognition of 84%, 89%, and 47%, respectively. To further enhance identification accuracy, it is suggested to utilize HAXELs with higher force outputs. To achieve high stimulation at the fingertips, Grasso *et al.* fabricated soft, compliant, and stretchable HAXEL arrays entirely through inkjet printing (Fig. 3e).[58] Driven by 4 kV, these arrays exhibited free displacements and blocking forces of 200 μm and ∼22 mN, respectively. Even at 1 kHz, the displacement remained above 20 μm, surpassing perception thresholds. Trials on 12 volunteers showed a high identification accuracy of 85% with no significant deterioration in performance over 9 days, which indicates the effectiveness and reliability of HAXEL actuators for wearable haptics. Testing involving 12 volunteers yielded an identification accuracy of 85%, with no notable decline in performance observed over 9 days. This outcome underscores the effectiveness and reliability of HAXEL actuators for wearable haptic applications.

Although electrohydraulic tactile actuators have shown promises for tactile devices with high output forces and displacements, the operating voltage is relatively high. This may be addressed by increasing the dielectric constant of the shell to generate larger electrostatic forces.[94] Stacking multiple electrohydraulic actuators could potentially improve force outputs at lower voltages.[100] The advancement of high voltage power supplies may further enable electrohydraulic actuators to become untethered and portable, allowing them to be better suited for portable or wearable devices. For instance, a battery powered, pocket sized, 10-channel power supply has been designed with each having an output of 10 kV and was further demonstrated to drive an array of ten HASEL actuators.[101] Nonetheless, power input remains low in the milliwatt range due to the low current applied. While research has demonstrated electrical self-healing of the dielectric liquid, the possibility of shell puncture and subsequent liquid leakage remains. To tackle this challenge, the utilization of self-healing materials is discussed in Section 4.1.

3.1.3 Piezoelectric and electrostrictive actuators

When subjected to an electric field, intrinsic electromechanical coupling within dielectric materials enables polymers to undergo actuation *via* piezoelectric effects and electrostriction.

Piezoelectric and electrostrictive actuators offer several advantages for generating tactile feedback, including flexibility, high-frequency operation, rapid response, and moderate driving voltages. While these polymers may share similarities in the device structure and characteristics, their underlying working principles remain distinct. The piezoelectric effect is often exhibited in non-centrosymmetric polymers and arises from changes in polarization due to mechanical stress, generating charges (Fig. 4a).[102,103] This implies that dielectric polymers with greater dipole moments exhibit larger piezoelectric effects. Conversely, a mechanical strain is induced when an electric field is applied to a piezoelectric polymer. Notably, the piezoelectric effect is linear, with actuation strain proportional to the applied electric field. Commonly employed piezoelectric polymers for actuators include poly(vinylidene fluoride) (PVDF)[104] and poly(vinylidene fluoride–trifluoroethylene) (P(VDF–TrFE)).[61]

On the other hand, electrostriction occurs as dipoles within the dielectric polymer align themselves along the direction of the electric field. This alignment induces changes in the chain conformations of the material, resulting in alterations in their dimensions (Fig. 4b).[102,103] This mechanism differs from Maxwell pressures, originating from the Coulombic interactions between oppositely charged electrodes. However, in the case of polar polymers with a low modulus, actuation results from the combined effects of Maxwell pressure and electrostriction.[106,107] When polar polymers have a high modulus, actuation is primarily driven by electrostriction effects. Polymers known to utilize electrostriction for actuation include poly(vinylidene fluoride–trifluoroethylene–chlorofluoroethylene) (P(VDF–TrFE–CFE)),[65] poly(vinylidene fluoride–trifluoroethylene–chlorotrifluoroethylene) (P(VDF–TrFE–CTFE)),[105] and polyurethane elastomers.[108] As shown in eqn (3.4), for linear dielectrics, the electrostrictive strain (S_E) is proportional to the square of the electric field (E).[109,110]

$$s_E = QP^2 = Q(\varepsilon_r - 1)^2 \varepsilon_0^2 E^2 \qquad (3.4)$$

ε_r and ε_0 are the dielectric constant of the dielectric polymers and vacuum permittivity, respectively; and Q, P, and E represent the electrostrictive coefficient, polarizability, and electric field, respectively.

In recent years, there has been significant progress in developing and commercializing piezoelectric polymer actuators, particularly those based on materials like PVDF and its copolymers.[111] To improve output performance and ease of fabrication, multilayer piezoelectric polymer actuators and screen-printing techniques are typically employed.[62,104] Microsoft Applied Sciences demonstrated a soft haptic device utilizing PVDF films that were screen-printed with conductive silver electrodes.[104] Stacking the films to 25 layers and modulating the voltage from 100 to 300 V led to significant improvements in force output (3.7 to 6.7 mN) and displacement (1.2 to 4.1 μm). Only 150 V was required to deliver perceptible stimulation when tested on nine volunteers. Furthermore, the device flexibility enables the device to be mounted on various surfaces, including furniture, garments, and the human body.

This journal is © The Royal Society of Chemistry 2024

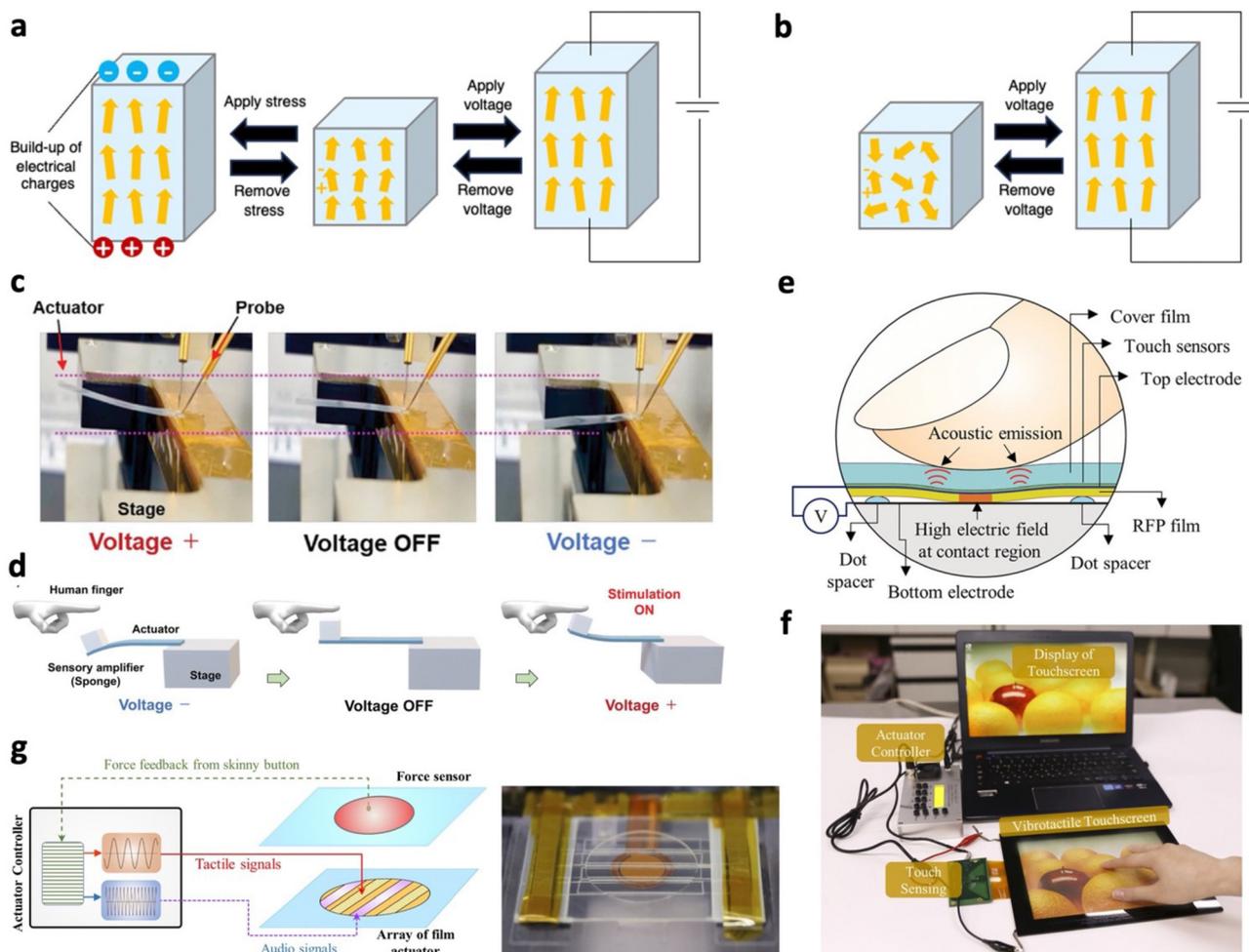*Chem. Soc. Rev.*, 2024, **53**, 3485–3535 | 3495

Fig. 4 Piezoelectric and electrostrictive actuators for tactile feedback. (a) Working principle of the piezoelectric effect. Mechanical stress on the piezoelectric polymer generates charges. The inverse piezoelectric effect occurs when an electric field induces physical strain in the polymer. (b) Working principle of electrostriction. Alignment of dipoles induces changes in electrostrictive polymer chain conformations, altering the dimensions. The yellow arrows represent electric dipoles. (c) Photograph of a piezoelectric actuator operating under positive, zero and negative voltage. (d) Schematic illustrating the proposed application of a bending piezoelectric actuator for generating tactile feedback. (c) and (d) Are adapted from ref. 61 and published by Wiley-VCH under Creative Commons CC BY License. (e) Working principle of a fretting vibrotactile display. (f) Photograph of a large area pressure-responsive fretting vibrotactile touchscreen. (e) and (f) Are adapted with permission from ref. 105. Copyright 2019, American Chemical Society. (g) Control system of a skinny button that generates tactile and audio feedback (left). Photograph of an audio-tactile skinny button (right). Adapted from ref. 63 and published by Springer Nature under Creative Commons CC BY License.

Combining capacitive sensing to detect force with vibrotactile actuation, the haptic device demonstrated its utility in various applications, such as training medical personnel to control the fluid injection rates and enhancing user interactions with virtual environments. Researchers have introduced fillers into the polymer matrix to enhance the piezoelectric effects of PVDF-based polymers further.[61,112] These fillers promote the formation of crystalline structures, particularly the β-phase, which has the highest dipolar moment per unit cell. Shouji et al. introduced single-walled carbon nanotube (SWCNT) fillers to P(VDF–TrFE), enhancing actuation displacements from 0.8 to 1.5 mm at 50 mV m^{-1} and 1 Hz (Fig. 4c).[61] This is attributed to improved crystallization due to hydrogen bonding between the nanocarbon surface and P(VDF–TrFE). Furthermore, composite actuators showed enhanced frequency

characteristics and extended cycling lifetime, operating up to 100 Hz and enduring over 6×10^5 cycles. With these features, the piezoelectric composite actuator was proposed to provide vibrotactile feedback to human fingertips by dynamic touching and untouching (Fig. 4d).

Electrostrictive polymer actuators have garnered increasing attention due to their large electrostrictive strains achievable at moderate voltages and high frequencies. Notably, Duong et al. designed a fretting vibrotactile display using electrostrictive actuators, consisting of a blend of P(VDF–TrFE–CTFE) and P(VDF–TrFE).[105] In principle, the operation relies on applying an alternating voltage across the top and bottom electrodes. When pressure from the fingertip causes the film to bend, the top electrode and polymer film encounter the bottom layer. This action creates a localized high electric field, generating an

3496 | Chem. Soc. Rev., 2024, 53, 3485–3535

This journal is © The Royal Society of Chemistry 2024

electrostrictive strain that provides tactile feedback (Fig. 4e and f). Based on this principle, the display demonstrated operability within a wide frequency range, from 1 to 500 Hz, achieving varying vibration amplitudes, ranging from 3.5 to 1 μm, respectively, at 200 V. Furthermore, the inclusion of P(VDF–TrFE) (VDF : TrFe = 55 : 45) enhances the actuation performance at elevated temperature (60 °C), by preventing modulus reduction. The authors also demonstrated the high frequency capabilities of these actuators by designing a skinny button capable of generating fretting vibrations to offer tactile (50 to 300 Hz) and audible feedback (500 Hz to 20 kHz) (Fig. 4g).[63] Electrodes composed of a similar electrostrictive polymer were patterned to form an array of ribbon-shaped actuators, allowing for activation and control of multiple areas simultaneously. This design led to larger vibration amplitudes (5.4 μm), outperforming haptic buttons with uniform electrodes (1.2 μm), when subjected to a sinusoidal voltage of 200 V and 200 Hz. This superior performance can be attributed to variations in localized electric fields and active areas, influencing the resistance of the top layer. Combining audio feedback with tactile sensations can better simulate the "click" sensation, enhancing the user interface.

Stacking multiple layers of electrostrictive polymers presents a promising avenue to reduce the required driving voltage, enhancing the practicality of haptic devices for generating high-output tactile feedback using portable power sources. For example, stacking two layers of 4 μm thick P(VDF–TrFE–CTFE) actuators yielded a vibration amplitude of ∼3.3 μm at 100 V and 220 Hz.[64] This amplitude is notably larger compared to single-layer actuators and single-layer actuators with a similar thickness to the stack, which achieved vibrational amplitudes of 0.6 μm and 1.3 μm, respectively. The stacked design was subsequently fabricated as a large flexible touchscreen display and tested on 50 users, who provided feedback indicating that the vibrations produced were sufficient for effective tactile sensations. Alternatively, rolled configurations have been adopted, wherein the device exhibited elevated actuation performance, with free displacements and force outputs of 0.5 mm and 1.1 N, respectively, at a voltage of 300 V.[65]

Compared with other electric field-driven soft tactile actuators, piezoelectric and electrostrictive actuators stand out due to their ability to operate at moderate driving voltages and high frequencies while providing sufficient displacements and forces for tactile feedback. Nonetheless, these actuators are restricted in the range of sensations offered due to their lower maximum force and displacement capabilities. In addition, the temperature sensitivity and hysteresis of these actuators should be improved for stable output performances.

3.1.4 Electrochemical actuators. Among various electrically driven actuators, electrochemical actuators (ECAs) require the lowest driving voltage, often ranging below 10 V.[47,113] These actuators are flexible, lightweight, simple to fabricate, and can achieve large deformations. For in-air operation, ECAs are composed of an ion exchange membrane sandwiched between two electrodes. During electric field application, actuation is achieved by generating volumetric or pressure gradients between the electrodes via electrical double layer (EDL) formation or redox reactions (Fig. 5a). To achieve high actuation performance (deformation, force output, and response time), the components selected should enable high electrochemical charge storage and fast ion transport for ECAs. Typically, ion exchange membranes may be composed of ionic polymers such as Nafion and Flemion,[114,115] or polymer-liquid electrolyte blends such as polyvinylidene fluoride with ionic liquids.[116–118] A wide range of electrodes have been developed for ECAs from metals,[114,119] conductive polymers,[120,121] and carbon-based materials.[118]

To date, various works have applied ECAs to generate tactile stimulation.[121–127] This can be attributed to their low driving voltage (<10 V) that provides greater safety to users and compatibility with off-the-shelf batteries, making devices portable. Their simple fabrication makes ECAs easily shaped and miniaturized, achieving tactile stimulation with high spatial resolution.[122,124,128] Early works of tactile displays utilizing ECAs were demonstrated by Konyo et al.,[122,124,125] who generated delicate sensations of touching cloth (Fig. 5b). ECAs were tilted at an angle of 45° to provide tactile stimulation in normal and tangential directions, at which modulating the voltage amplitude and frequency generated static and active touch sensations of roughness, pressure, and friction. However, water loss from the device limits the operation in air to only several minutes. To minimize water evaporation from tactile devices, a tactile device was designed with a PDMS bump attached to the top surface of ECA cantilever beams.[123,126] The bump provided partial coverage of the upper surface, minimizing the evaporation rate for better stability, and acted as an insulative contact interface between the ECA and the fingertip. During initial contact with the user, the bump remains below the fingertip, and during actuation, it encounters the fingertip with a normal contact force (Fig. 5c).[126] The range of tactile stimulation can be further extended by attaching the bump to a pair of ECAs at which activating two and one ECAs leads to normal and shear forces, respectively (Fig. 5d).[123]

For improved operation stability, tactile devices may apply encapsulation strategies to ECAs.[129] This includes techniques such as manual application,[130] dip-coating,[131,132] spray coating,[132–134] and chemical vapor deposition[135,136] to apply materials like silicones,[136,137] parylene,[135,136] and poly(styrene-*block*-isobutylene-*block*-styrene).[131,133,134] The impact of encapsulation was highlighted by Kim et al., who utilized parylene to encapsulate an ECA composed of Nafion with platinum electrodes, extending the lifetime (time taken for actuation displacement to reach 60% of maximum) from 400 s to 6500 s.[136] While the thickness of these parylene coatings showed negligible changes to the maximum actuation displacement, thicker coatings took longer to reach this maximum. This highlights the need to carefully select the encapsulation thickness and modulus to reduce the restriction to actuation.[129] Alternatively, abundant works on ECAs have replaced water with various ionic liquids. These ionic liquids have low vapor pressure, wide electrochemical windows, and high conductivity, allowing selection as a solvent for ECAs to provide high actuation

This journal is © The Royal Society of Chemistry 2024

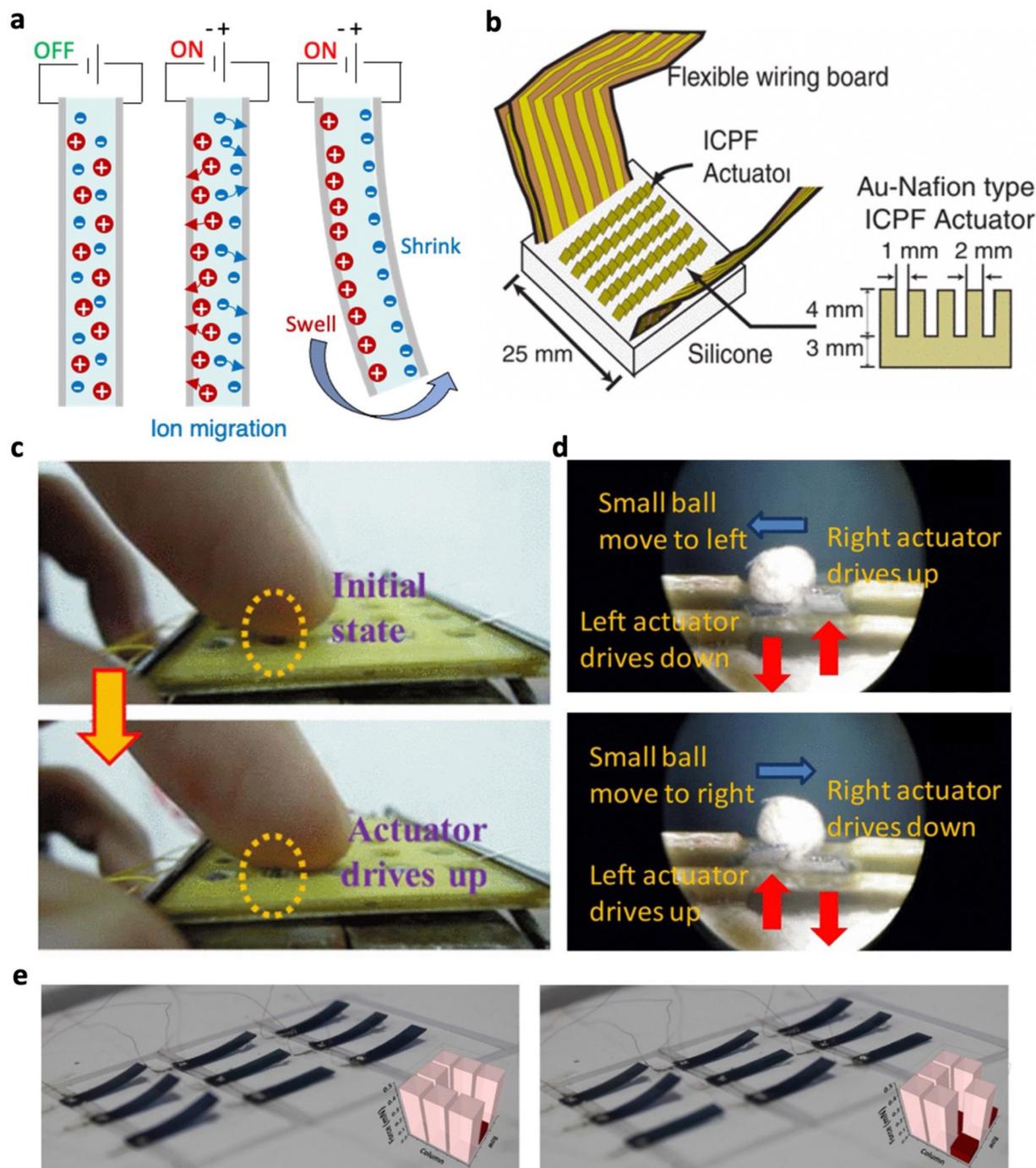Chem. Soc. Rev., 2024, **53**, 3485–3535 | **3497**

Fig. 5 Electrochemical actuators for tactile feedback. (a) Illustration of the working principle of electrochemical actuators. (b) Schematic representation of a wearable tactile display comprised of ionic conductive polymer gel film (ICPF) actuators that generate tactile sensations. Adapted with permission from ref. 122. Copyright 2005, IEEE. (c) Photograph capturing the operation of the tactile device. (d) Photograph showing an object manipulated by two ionic polymer metal composite (IPMC) actuators. Directional shear motion is achieved through selective activation of IPMC actuators. (c) and (d) Are adapted with permission from ref. 123. Copyright 2015, IEEE. (e) Photograph of an array of ionic actuators demonstrating tactile rendering of the alphabet through the selective application of voltage. Adapted with permission from ref. 121. Copyright 2019, American Chemical Society.

stability and performance.[47,113,138] With a polyurethane and $[EMIM]^+[TFSI]^-$ ionic liquid membrane, Kim et al. designed a tactile device that demonstrated tactile rendering of the alphabet (Fig. 5e).[121] High loading (80 wt%) of $[EMIM]^+[TFSI]^-$ was introduced to improve the ionic conductivity (~ 0.18 S m^{-1}) of

the membrane. Spray coating of ionic PEDOT:PSS electrodes on the membrane formed an interpenetrating nanofibrillar network at the interface, leading to a higher effective EDL. As a result, high actuated bending displacements and blocking forces of 5.1 mm and 0.4 mN, respectively, were achieved at

3498 | Chem. Soc. Rev., 2024, 53, 3485–3535

This journal is © The Royal Society of Chemistry 2024

2 V, DC. Also, the device showed long-term stability with negligible changes to the bending strain after 30 000 cycles. These ECAs can operate over a wider frequency range due to rapid ion transport, retaining a strain of ~0.01% at a frequency of 200 Hz, which is crucial for generating tactile feedback. With a tactile array, the actuation of each pixel can be controlled individually by varying the frequency to generate various textures.

Moving forward, to widen the range of tactile sensations provided by ECAs, approaches that improve the frequency performance of ECAs can be considered; the performances of ECAs are summarized in Table 2. These approaches include tuning the nano/micro-structure of ion exchange membranes,[116,120] or employing 2D nanomaterials such as covalent organic frameworks (COFs),[139,140] metal organic frameworks (MOFs),[141,142] graphdiyne[118] and MXene[142] to obtain rapid ion transport. ECAs are mostly shown to realize bending motions, limiting their tactile devices. Patterned electrodes have been introduced to ECAs to realize complex deformations through photolithography[143] and electroplating combined with electroless chemical reduction.[144,145] 3D printing may be further employed to obtain ion exchange membranes with customized shapes and features.[146–148] Also, to ensure that ECAs can be effectively made untethered in the future, the power consumption of the actuator should be monitored. In some cases, large driving currents are used, leading to power consumption of tens to hundreds of milliwatts.[114,149] This may be addressed by tuning the waveform of the applied voltage.[150]

3.2 Pneumatic

Soft pneumatic actuators (SPAs) have emerged as a dominant class of soft actuators, mainly due to their lightweight, high force and displacement, safe and soft contact, and easy implementation.[154] Owing to these advantages, SPAs have been a compelling choice for generating tactile feedback. In general, SPAs harness air pressure to inflate or deflate hollow chambers within elastomeric bodies, achieving mechanical motion. The fundamental components encompass a deformable elastomer housing an air chamber, connecting pipes, and external pumps. While air pressure is isotropic within the chamber, directional actuation is accomplished through external constraints that guide their movement.

Similar to other soft actuators, silicone rubber has commonly served as the primary material for fabricating SPAs in tactile devices. This choice is attributed to their low modulus, large strains, and low hysteresis.[154] These benefits are seen in the design of a refreshable Braille display consisting of an array of pneumatic microbubble actuators fabricated from either polyurethane or PDMS.[155] When comparing these materials at 0.2 Hz with pressure inputs to maintain maximum displacement, the low hysteresis exhibited by PDMS enables Braille dots to recover more during deflation. Furthermore, PDMS Braille dots demonstrated the ability to sustain peak-to-peak displacements of 0.265 mm when actuated at frequencies up to 200 Hz, making them a viable choice for vibrotactile feedback applications.

Table 2 Actuation performance of low voltage electrochemical actuators with wide frequency operation and long-term stability

Active electrodes	Ion exchange membrane	Maximum peak-to-peak displacement (strain)	Frequency range (Hz)	Peak-to-peak displacement (strain) @ maximum frequency	Maximum blocking force (mN)	Long-term stability (retention %, cycle)	Ref.
PEDOT:PSS/EMIM-TFSI/DMSO	TPU/EMIM-TFSI	4.8 mm (0.61%) @ ±2 V, 0.1 Hz	0.1–200	N.A. (0.01%) @ 200 Hz	0.40	~97%, 40 000	121
PEDOT:PSS	LC electrolyte/PVC/PVDF-HFP	N.A. (0.63%) @ ±2 V, 0.1 Hz	0.1–80	2.6 mm (N.A.) @ 80 Hz	0.35	~114%, 14 400	120
Graphdiyne	PVDF/EMIM-BF$_4$	~33.2 mm (0.78%) @ ±2.5 V, 0.1 Hz	0.1–30	~2.2 mm (0.07%) @ 30 Hz	3.37	~96%, 100 000	118
Ni-CAT NWAs/CNF	PVDF/EMIM-TFSI	12.1 mm (0.36%) @ ±3 V, 0.1 Hz	0.1–20	~0.09 mm (N.A.) @ 20 Hz	1.45	~109%, 10 000	141
BP-CNTs/CNTs	PVDF-HFP/EMIM-BF$_4$	21.4 mm (1.67%) @ ±2.5 V, 0.1 Hz	0.1–20	~2.5 mm (0.29%) @ 20 Hz	6.0	90%, 500 000	151
PEDOT:PSS	COF-DT-SO$_3$NA	12.1 mm (~0.44%) @ ±0.5 V, 8 Hz	0.1–20	0.4 mm (0.016%) @ 20 Hz	1.20	~99%, 23 000	139
Si/graphene	Nafion/Li$^+$	15 mm (N.A.) @ ±0.8 V, 1 Hz	1–20	~3.6 mm (N.A.) @ 20 Hz	71.0	90%, 10 000	152
Ti$_3$C$_2$T$_x$-MnBTC/PEDOT:PSS	Nafion/EMIM-BF$_4$	~28.0 mm (N.A.) @ ±1 V, 0.1 Hz	0.1–10	~0.6 mm (N.A.) @ 10 Hz	5.88	98%, 43 200	142
PEDOT:PSS/DMSO	FCBC/PPy/EMIM-BF$_4$	13.8 mm (0.93%) @ ±0.5 V, 0.1 Hz	0.1–10	~1.1 mm (~0.11%) @ 10 Hz	~0.58	96%, 1800	153
BS-COF-C900	Nafion/EMIM-BF$_4$	8.6 mm (0.62%) @ ±0.5 V, 0.1 Hz	0.1–10	~0.83 mm (~0.06%) @ 10 Hz	N.A.	90%, 21 600	140

~: Estimated from figures; N.A.: not available; PEDOT:PSS: poly(3,4-ethylenedioxythiophene) polystyrene sulfonate; EMIM-TFSI: 1-ethyl-3-methylimidazolium bis(trifluoromethylsulfonyl)imide; DMSO: dimethyl sulfoxide; TPU: thermoplastic polyurethane; PVC: poly(vinyl chloride); PVDF-HFP: poly(vinylidene fluoride-co-hexafluoropropylene); PVDF: polyvinylidene fluoride; EMIM-BF$_4$: 1-ethyl-3-methylimidazolium tetrafluoroborate; Ni-CAT NWA: nickel triphenylene-fused catecholate nanowire arrays; CNF: carbon nanofibers; BP: black phosphorus; CNTs: carbon nanotubes; COF-DT-SO$_3$NA: two-dimensional ionic covalent organic framework; Ti$_3$C$_2$T$_x$-MnBTC: MXene electrode anchoring manganese-based 1,3,5-benzenetricarboxylate metal–organic framework; FCBC: functional carboxylated bacterial cellulose; PPy: polypyrrole; BS-COF-C900: covalent organic framework derived boron and sulfur co-doped porous carbon.
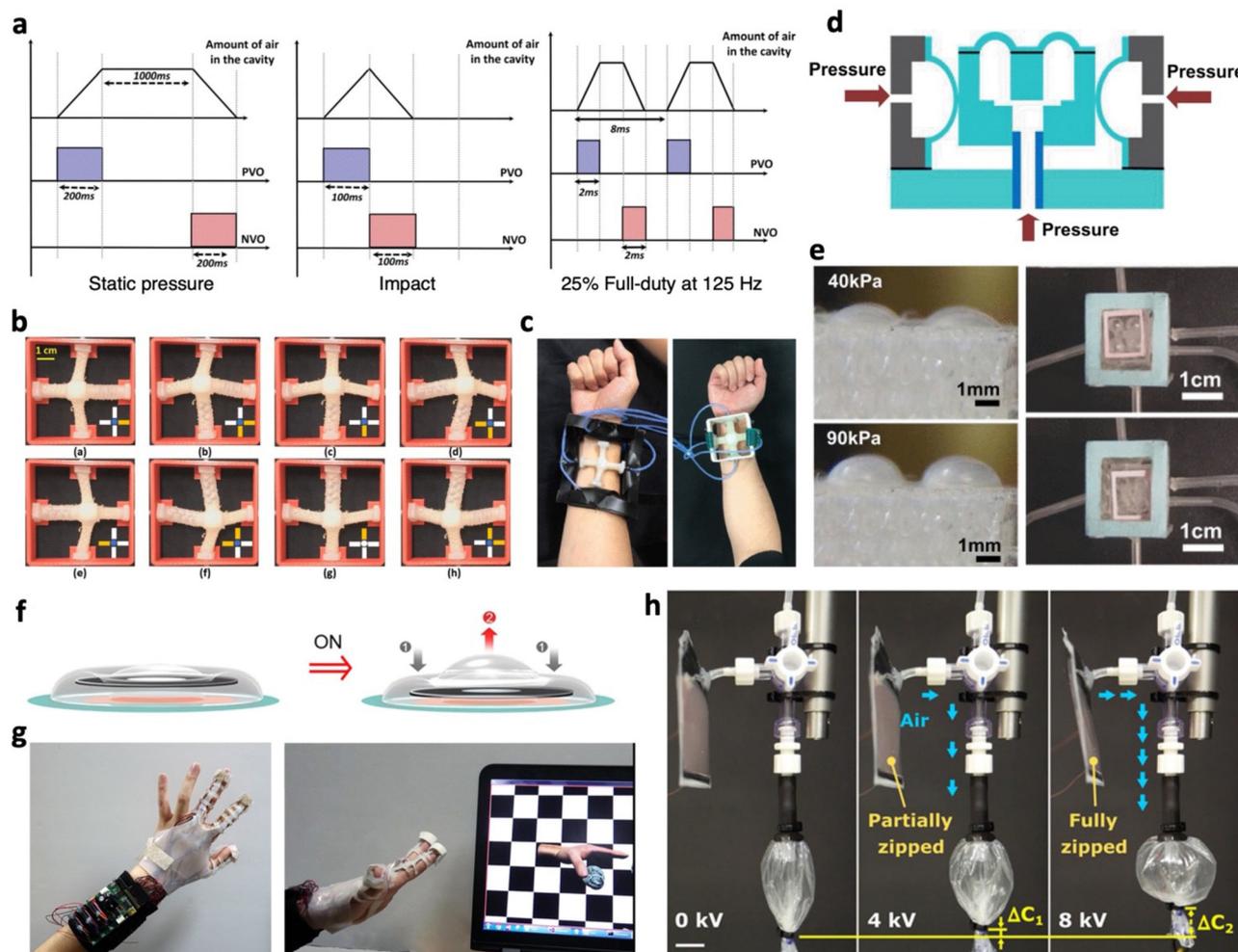
This journal is © The Royal Society of Chemistry 2024

Chem. Soc. Rev., 2024, **53**, 3485–3535 | **3499**

Fig. 6 Pneumatic actuators for tactile feedback. (a) Control pattern illustrating the positive valve open (PVO) and negative valve open (NVO) sequences used to achieve various types of tactile feedback. Adapted from ref. 156 and published by IEEE under Creative Commons CC BY License. (b) Photograph displaying a central tactor shifted in different directions through various combinations of pressurizing and depressurizing soft linear pneumatic actuators. (c) Wearable haptic device with either soft or rigid housing. (b) and (c) Are adapted with permission from ref. 157. Copyright 2019, IEEE. (d) Schematic depicting the structure and operating mechanism of a 3-axis PDMS pneumatic actuator for vibrotactile feedback. (e) Photographs demonstrating normal and shear actuation. (d) and (e) Are adapted with permission from ref. 158. Copyright 2011, IEEE. (f) Illustration of the operation of an electropneumatic actuator for tactile feedback. (g) Photograph showcasing a VR glove equipped with integrated pneumatic actuators used for interacting with virtual objects. (f) and (g) Are adapted from ref. 159 and published by Springer Nature under Creative Commons CC BY License. (h) Photograph of an electropneumatic pump operating a contractile soft pneumatic actuator at different applied voltages. Adapted with permission from ref. 160. Copyright 2021, The American Association for the Advancement of Science.

With the objective of providing a diverse range of tactile sensations, innovative SPA tactile devices have been developed. This is accomplished by controlling pressure sequences, adjusting inflation and deflation durations, and varying pressure amplitudes.[156] By adopting this strategy, a ring-shaped SPA was designed to deliver multi-mode tactile feedback, encompassing static pressure, impact, and vibrational sensations to the user finger (Fig. 6a).[156] Static pressure generation depended on the positive pressure valve opening duration. On the other hand, impact feedback is achieved by inflating the chamber, followed by a sequence involving the immediate closing and opening of positive and negative pressure valves, respectively. Vibration feedback was generated by alternately opening and closing the positive and negative valves, resulting in

accelerations of 1.17 m s^{-2} at a high frequency of 250 Hz, higher than the human perception threshold (0.08 to 0.1 m s^{-2}). The ability to achieve such high-frequency vibration was attributed to lightweight moving parts with minimal inertia, rapid valve control mechanisms, and highly compressed air. Apart from generating normal forces for tactile feedback, several studies have focused on providing shear forces to simulate skin stretch.[157,158] For instance, Kanjanapas *et al.* developed a two-degree-of-freedom tactile device consisting of four linear SPAs arranged in a cross-shape with a tactor in the middle, which contacted the user forearm.[157] By pressurizing and depressurizing each linear SPA in various combinations, the tactor could be directed in eight distinct motions (Fig. 6b). User tests revealed that rigid housings provided better

3500 | *Chem. Soc. Rev.*, 2024, **53**, 3485–3535

This journal is © The Royal Society of Chemistry 2024

identification accuracies (86%) for the skin stretch direction compared to soft housings (66.5%) (Fig. 6c). This was attributed to minimized reaction forces that shifted the housing, preventing user confusion regarding the tactor direction. However, the trade-off of increased bulkiness with rigid housings compromised user comfort, highlighting the importance of additional design aspects when creating wearable tactile devices imparting shear forces. For practical applications, shear and normal tactile feedback play crucial roles, particularly in fields like surgical robotics, where surgeons require a sense of touch to interact better with patients. To address this need, a 3-axis SPA-based tactile device was developed and integrated into the grasp of a surgical robot, offering surgeons both shear and normal tactile feedback.[158] This tactile device consisted of a central structure surrounded by four side walls (Fig. 6d). Normal forces were applied through the central structure, utilizing four SPAs arranged in a 2 × 2 array on the top surface. On the other hand, shear forces were generated by independently activating SPAs located on each side wall, resulting in horizontal movement of the central structure (Fig. 6e). This allowed for maximum lateral and horizontal deformations of 3.5 mm at 40 kPa and 1.7 mm at 90 kPa, respectively, enabling the finger to perceive actuation successfully.

Despite the capabilities of SPAs to achieve high actuation forces and displacements while remaining soft and compliant, one of their notable limitations lies in the reliance on bulky external pumps to generate the necessary air pressure. This hinders the portability and wearability of SPA-based tactile feedback devices. Electropneumatic actuators that rely on internal pressures have been utilized to address this issue.[159] These electropneumatic actuators typically consist of a pouch with air that is sandwiched between two overlapping electrodes. Upon voltage application, electrostatic attraction between the electrodes causes them to move closer, compressing the pouch and redistributing the air within. Song *et al.* utilized this principle to achieve an electropneumatic actuator where electrostatic attraction occurred in an outer ring region, facilitating the redistribution of air to the central region for tactile feedback (Fig. 6f).[159] The actuator was integrated with a piezoelectric sensor, interface board, and batteries to achieve a VR glove that enabled interactions with virtual objects (Fig. 6g).

Moreover, there has been a growing interest in developing soft portable pumps to replace the bulky external ones used with SPAs. These portable pumps can operate based on electropneumatic principles, where air is redistributed to connected SPAs during activation.[160] For instance, an electropneumatic pump weighing only 5.3 grams utilized dielectric fluid-amplified electrostatic zipping to generate a pressure output of 2.34 kPa while consuming only 0.5 W.[160] The pump successfully operated a contractile SPA (Fig. 6h), achieving contraction changes of 32.4% and lifting a maximum load of 100.4 g at 8 kV. When paired with miniature high voltage power sources, these pumps can potentially be applied for portable and wearable tactile devices. Alternatively, portable pumps have relied on microscale combustion of methane–oxygen mixtures, where liquid metal electrodes generate sparks to ignite the mixture,

resulting in rapid pressurization and SPA activation.[161] This approach led to SPAs achieving displacements of 6 mm within 1 ms, and ∼100 mm at an operational frequency of 1.2 kHz. Additionally, soft portable pumps have utilized electrochemical reduction of water to generate hydrogen gas for inflating SPAs.[162] These advancements in soft portable pumps hold promise to miniaturize SPA-based tactile systems and enhance their wearability in various applications.

While SPAs have made substantial advancements in tactile devices, their durability under real-world conditions remains a concern. When SPAs are inflated, their membrane becomes thinner, making them susceptible to damage when in contact with rough particles and surfaces. To enhance the durability of SPAs, methods discussed in Section 4 can be employed, ensuring that these innovative SPA applications can withstand the challenges of practical use.

3.3 Thermal

Thermally triggered soft tactile actuators are known for their versatility, being responsive to various thermal sources, including infrared light, Joule heating, and thermal radiation. To achieve on-demand mechanical responses for haptic communications, it is crucial to employ effective and controllable heating strategies to design these devices. One effective strategy is Joule heating, also known as resistive heating, which involves passing current through a conductive material. However, the conductive material must possess sufficiently high electrical conductivity to enable Joule heating at low voltages. This property brings a significant advantage to the Joule heating method, consuming lower power and making these actuators easily portable through readily available commercial batteries for activation.[163,164]

Alternatively, another approach directly incorporates photothermal agents into thermal actuators, providing a pathway to untethered heating and activation. Photothermal agents, such as CNTs,[165–168] graphene flakes,[169,170] and metal nanofillers,[171,172] have typically been employed. These agents are dispersed within the polymer matrix, effectively absorbing visible and/or infrared light. This absorption generates localized heat, which is then transferred into the polymer matrix to induce thermal actuation.[167,170] To enable high loading and uniform heat distribution, there has to be compatibility between the polymer matrix and fillers. This can be improved through surface modification of fillers, ensuring covalent or physical bonding between the two components that provides uniform dispersion of the fillers within the polymer matrix.[173]

During the operation of these actuators, it is preferred that surface temperatures of the tactile device remain below 60 °C, the temperature at which humans can contact it for up to 5 s without getting burnt.[174] In this section, we review the utilization of these thermally triggered soft actuators for generating tactile feedback, with a focus on technologies involving shape memory polymers (SMPs), liquid crystal elastomers (LCEs), thermo-responsive hydrogels, and liquid–vapor phase transitions.

This journal is © The Royal Society of Chemistry 2024

Chem. Soc. Rev., 2024, **53**, 3485–3535 | **3501**

3.3.1 Shape memory polymers. The shape-memory effect in SMPs arises from the coexistence of permanent and switching phases within the polymeric matrix.[175–177] This permanent phase, formed through crosslinking during polymer processing, maintains stable physical properties within the relevant temperature range. The network stores elastic energy upon deformation, dictating the permanent shape of SMPs. Conversely, the switching phase comprises polymeric segments with temperature-dependent chain mobility or flexibility. Switching mechanisms can involve glass–rubbery phase transitions, melting/crystallization, or reversible covalent bonds. As illustrated in Fig. 7a, when an SMP is heated beyond a specific transition temperature (T_{trans}), the switching segments become softened and compliant, enabling macroscopic deformation. When cooled to temperatures below T_{trans} the switching phase

becomes locked, temporarily fixing the SMP in the deformed shape. This process is defined as programming and can be performed repetitively. Subsequently, re-heating to temperatures above T_{trans} releases the locking points in the switching phase, while the stored elastic energy in the permanent phase restores the SMP to its original shape.

Typically, SMPs applied for tactile devices only exhibit one-way effects, implying that actuation is not reversible as heating only triggers the recovery process. Nonetheless, this quality makes SMPs well-suited for scenarios necessitating stable and long-term shape changes, such as Braille displays,[183] as they can maintain temporary shapes without requiring a continuous power supply. However, SMPs are less suitable for dynamic haptics. In practical usage, they are frequently combined with another actuating mechanism to achieve reversibility. Besse
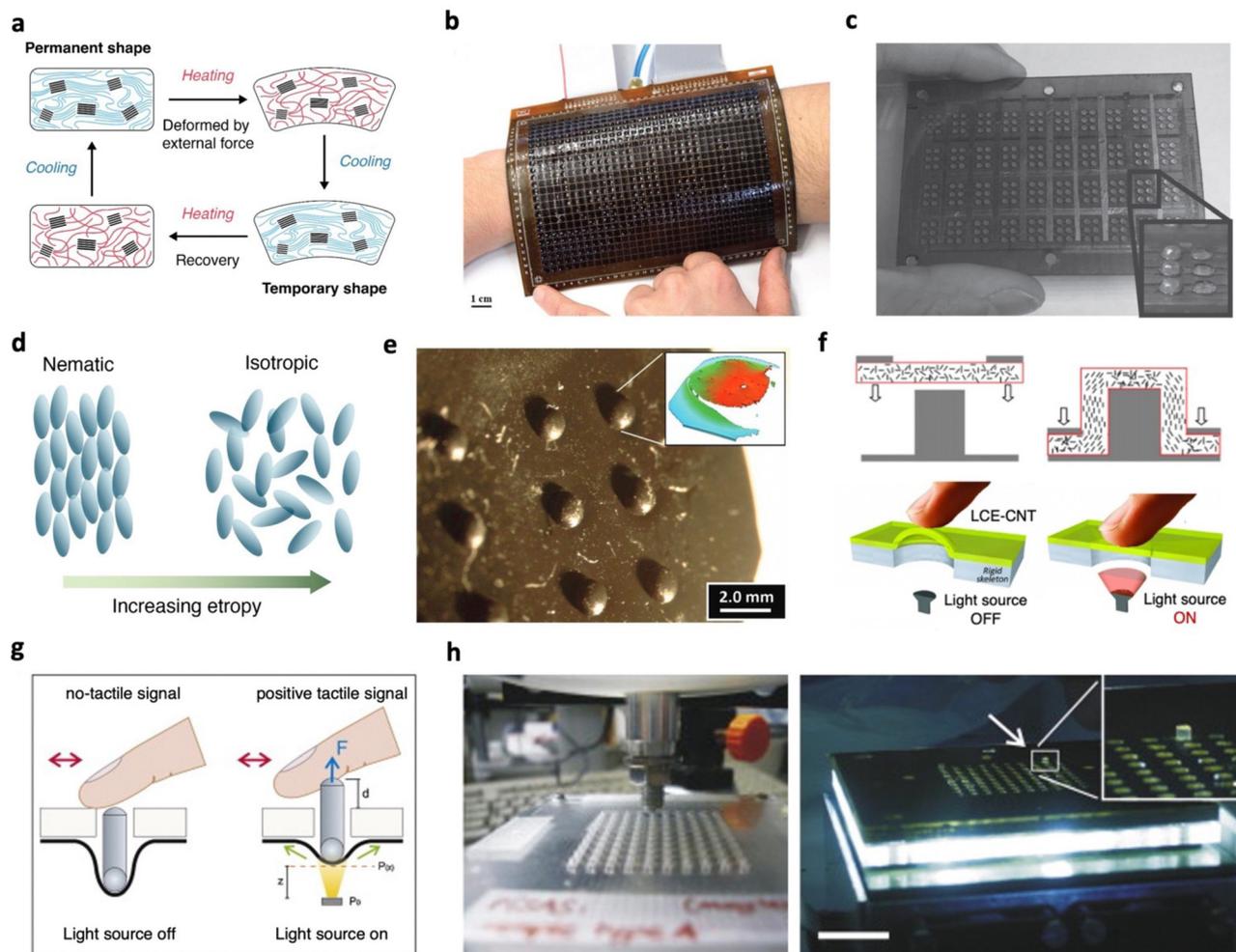

Fig. 7 Thermal tactile actuators based on SMP and LCE. (a) Schematic illustration of the operational mechanism for shape memory polymers. (b) Photograph of the haptic display based on pneumatic programming and shape-memory refreshing. Adapted with permission from ref. 178. Copyright 2017, Wiley-VCH. (c) Photograph of the Braille display panel enabled by the bistable DEA. Adapted with permission from ref. 179. Copyright 2012, Wiley-VCH. (d) Schematic illustration of the nematic–isotropic phase transition of LCEs. (e) Photograph of the Braille blister array produced from the LCE–CNT composite. Inset: Confocal image of a blister unit. Adapted with permission from ref. 180. Copyright 2011, Wiley-VCH. (f) Illustrations of the die molding process for producing LCE–CNT blisters (top). The blister can reduce its height upon illumination (bottom). Adapted with permission from ref. 181. Copyright 2012, IOP Publishing Ltd. (g) Schematic illustrations showing the pin movements triggered by the actuation of the LCE–CNT composite with light on and off. (h) Photographs of the 10 × 10 Braille device comprising the actuator and LED arrays. (g) and (h) Are adapted with permission from ref. 182. Copyright 2014, Elsevier B.V.

3502 | *Chem. Soc. Rev.*, 2024, **53**, 3485–3535

This journal is © The Royal Society of Chemistry 2024

et al. demonstrated a high-resolution haptic display (32 × 24 taxels, Fig. 7b) by synchronizing thermal stimulus with pneumatic actuation.[178] The authors patterned an array of compliant heaters on a thin SMP membrane, allowing each SMP taxel to be independently addressed *via* resistive heating. Given that the stiffness of the SMP can reduce significantly (over 100 times) upon heating beyond T_{trans}, only selected pixels are heated to undergo deformation by pneumatic pressure, leaving unheated pixels unaffected. By coupling localized heating with global pneumatic pressure (either positive or negative), the taxel matrix can be programmed to convey diverse haptic feedback. Heating the taxels without pressure refreshes them back to the flat state. Operating under 70 °C and 30 kPa activation conditions, a taxel rendered 400 μm displacement and 1 N holding force after cooling. A complete actuation cycle—transitioning from one stable state to another—takes 5 s, including 2.5 s of heating and 2.5 s of passive cooling under pressure. In a recent study, Hu *et al.* achieved a triple-shape memory effect in a PDMS composite by harnessing the different melting points of polycaprolactone (PCL) and high temperature liquid metal.[184] A 9 × 9 Braille display was constructed based on this composite SMP. A heating platform and NIR laser were utilized to activate the Braille dots while refreshing the display required external mechanical compression. Another example involves a multi-stable SMP, specifically poly(*tert*-butyl acrylate) (PTBA), which was employed as the active dielectric elastomer in a DEA (Fig. 7c), combining electrostatic actuation with bistable shape retention.[179] This strategy allows high voltage (in the kV range) induced strains to be preserved for safe Braille recognition. By integrating SMPs with other actuation mechanisms, haptic displays can be tailored to cater to diverse user experiences.

To eliminate the need for manual re-programming and reliance on additional actuation mechanisms that could complicate the design, future endeavors may investigate the utilization of two-way SMPs for tactile devices. This could be achieved by implementing semi-crystalline networks,[185] interpenetrating networks,[186] and SMP laminates.[187] Such advancements hold the potential to enhance the versatility of soft thermal actuators for tactile devices by enabling reversible actuation.

3.3.2 Liquid crystal elastomers.

LCEs are a subset of liquid crystalline polymers that combine rubber elasticity with anisotropic liquid crystallinity. These liquid crystals are comprised of rigid molecules known as mesogens that tend to self-organize, leading to local order.[188] These mesogens can be incorporated into the polymer as main-chains or side-chains. A typical liquid crystal phase is the nematic phase, at which mesogens display long-range orientational order. Initially, LCEs are in the polydomain state at which nematic phases exist as locally disordered domains without macroscopic alignment. These polydomain LCEs are unable to achieve reversible actuation without external stresses. Thus, various alignment methods, such as mechanical and surface-enforced, have been employed to achieve macroscale alignment, forming monodomain LCEs.[189,190] This alignment imparts responsiveness through nematic–isotropic phase transitions triggered by temperature changes (Fig. 7d). When heated beyond this transition

temperature, the mesogens undergo a process of disordering, triggering a significant contraction parallel to their director orientation. Reversing the temperature realigns the mesogen units and elongates the LCE, facilitating reversible thermal actuation.[191]

The large, thermally induced actuation in LCEs can be used to trigger surface haptic devices.[192,193] For instance, multiple Braille displays have been devised by Camargo *et al.* based on the LCE–CNT composite.[180,181] A pair of pillar-die molds were employed to stamp an LCE–CNT composite film, resulting in an array of Braille blisters that retain a distinctive "dome" shape at room temperature (400 μm in height, 1.5 mm in diameter, Fig. 7e). The mechanical stretching involved during the molding process aligns the mesogens on the side walls of the blisters, enabling them to contract when exposed to light stimuli (Fig. 7f). With a light power input of 38.5 mW (658 nm laser), each blister undergoes ~10% contraction in height within ~4 s, followed by a subsequent recovery to its initial shape within ~5.6 s. However, direct exposure of the actuator to users and the environment could potentially lead to material degradation caused by dust and skin secretions. This was addressed by Torras *et al.*,[182] who inverted the orientation of LCE–CNT blisters and harnessed the contractile stress generated by the heated LCE to trigger the vertical displacement of a pin (Fig. 7g). This configuration enables the device to output non-Braille signals when the light is off, and Braille characters and pixelated images with programmed illumination. The authors assembled a 10 × 10 Braille interface, assembling a white-light LED and a focusing micro-lens beneath each actuator (Fig. 7h). To enhance the dynamic response of the device, LED power outputs were carefully tuned. This involved initially illuminating the pins at high intensity to rapidly raise them, followed by a reduction in intensity to maintain pin stability. With the pins capable of achieving average displacements of 0.8 ± 0.2 mm and maintaining a stable force output of 26.2 ± 0.2 mN throughout 100 actuation cycles, the criteria for effective Braille devices were realized.

Although LCE composites have demonstrated their ability to generate sufficient displacements and blocking forces, enabling precise tactile perception, their application is hindered by their slow response time. This delay arises from elevated phase-transition temperatures and relatively low energy conversion efficiency, limiting their practical usage to Braille applications that require high refreshing rates. Developing LCEs with lower phase-transition temperatures would significantly expand their use in real-time haptic interfaces.[194]

3.3.3 Thermo-responsive hydrogels.

Hydrogels consist of hydrophilic polymer networks that swell in water and shrink upon drying. This swelling and deswelling behavior can be harnessed for reversible actuation.[195,196] Moreover, programmable shape morphing behaviors can be realized based on localized swelling anisotropy.[197] The stimuli responsiveness of a hydrogel is determined by the chemical structure of the constituent polymer. For instance, the hydrophobicity of poly(*N*-isopropylacrylamide) (PNIPAAm) drastically varies with temperature due to thermally induced conformational changes
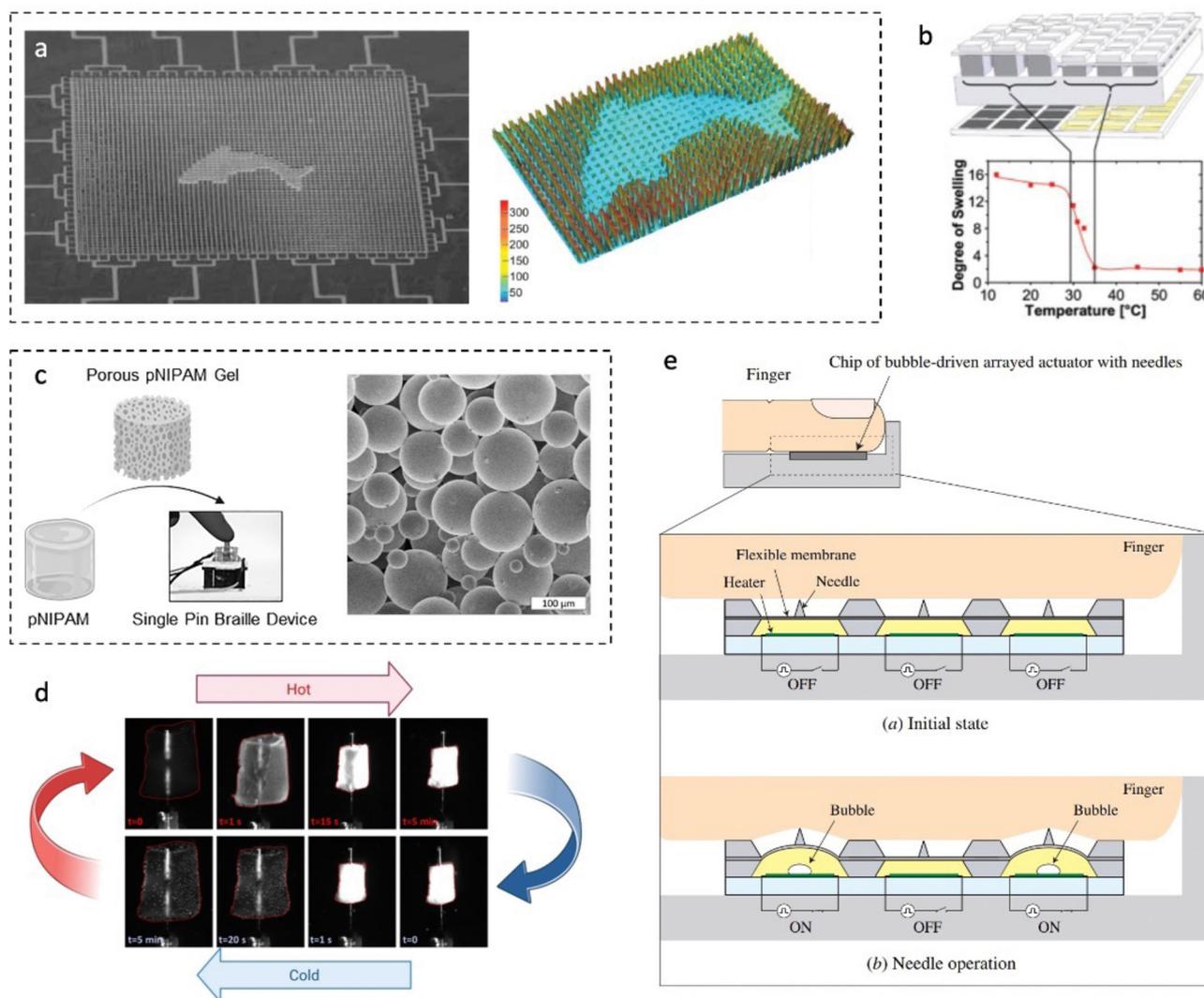
This journal is © The Royal Society of Chemistry 2024

Chem. Soc. Rev., 2024, **53**, 3485–3535 | 3503

Fig. 8 Thermal tactile actuators enabled by hydrogel swelling and liquid–vapor transition. (a) Photograph and topological image of the hydrogel actuator array displaying a dolphin pattern by activating selected hydrogel pixels. The pattern shows sharp contours and single-pixel accuracy. (b) Swelling and deswelling behavior of PNIPAAm micro-gels. (a) and (b) Are adapted with permission from ref. 199. Copyright 2009, Wiley-VCH. (c) Illustrations of the porous hydrogel and the single-pin Braille device (left). SEM image of the PMMA microspheres (right). (d) Photographs recording the shrinking–reswelling cycle of the porous hydrogel. (c) and (d) Are adapted with permission from ref. 200. Copyright 2023, American Chemical Society. (e) Schematic illustration depicting the operational principle of the bubble-driven tactile display. Adapted with permission from ref. 201. Copyright 2008, IOP Publishing Ltd.

in the polymer chain.[198] This allows a typical PNIPAAm hydrogel to actuate from a completely swollen state to a shrunken state (>90% volumetric change) upon a small increment in temperature (from 29 °C to 35 °C).[199]

Due to its high swelling capability, the PNIPAAm hydrogel is well-suited for thermally controlled tactile interfaces. However, the response rate of bulk hydrogels is commonly slow because they rely on the mass transport of water molecules to switch between swollen and shrunken states. At the micrometer scale, an increased surface-to-volume ratio enhances solvent transfer, significantly improving the response time of hydrogel actuation. Based on this principle, Richter *et al.* developed an array of PNIPAAm hydrogel micro-actuators (Fig. 8a),[199] with a footprint of 300×300 μm^2 and a pitch of 580 μm. A digital

projector was employed to provide accurate photothermal heating for individual pixels and to reversibly control the height of each hydrogel pixel between 500 μm (swollen) and 250 μm (shrunken). With a temperature change of only 10 °C (Fig. 8b), the micro-actuator can shrink completely within 0.9 s, followed by reswelling within a few seconds. This thermal actuation produces perceivable information based on pixel height and softness variations, with swollen hydrogel pixels having a low elastic modulus of 13 kPa. In comparison, the shrunken ones were significantly stiffer by one magnitude (100 kPa). The distinct difference in softness can enable visually impaired individuals to perceive the shape of a monochromic image and may assist remote palpation for diagnostic practices. The actuation speed of macroscopic PNIPAAm hydrogels has also

3504 | *Chem. Soc. Rev.*, 2024, **53**, 3485–3535

This journal is © The Royal Society of Chemistry 2024

been improved by morphological engineering. Yilmaz *et al.* introduced porosity into a bulky hydrogel (Fig. 8c) by using poly(methyl methacrylate) (PMMA) microspheres as a sacrificial template.[200] These interconnected pores facilitated rapid water diffusion, resulting in a 50% volume reduction in just 4 s. However, reswelling remained relatively slow due to hysteresis in the collapsed pores, taking 18 s for the sample to reach 80% of its fully swollen volume (Fig. 8d). To demonstrate the potential for tactile feedback, a single-pin Braille setup was developed using the porous hydrogel. Operated by resistive heating and active Peltier cooling, the Braille pin tip achieved maximum recoverable displacements of 1.4 mm and generated stable force outputs of 0.9 g over ten cycles.

Despite these advancements, one of the main challenges these hydrogel actuators face is their poor mechanical properties,[198] limiting their durability and operational lifespan under real-world conditions. Approaches to bolster the resistance of soft actuators against mechanical damage are further explored in Section 4.2.1.

3.3.4 Liquid–vapour phase transition. The liquid–vapor phase transition is a fundamental occurrence in nature and a crucial engineering method with diverse applications for refrigeration, thermal management, micro-fluidic, and microelectromechanical systems. According to classical nucleation theory,[202,203] the process of liquid boiling is initiated when tiny thermal bubbles nucleate and grow within a liquid due to superheating. Nucleation can proceed either homogeneously within the liquid environment itself or heterogeneously at the interface between the liquid and its surrounding materials.

Utilizing the controlled generation of thermal bubbles within a sealed and unilaterally deformable chamber presents a viable solution for creating surface haptic experiences. Shikida *et al.* developed a 3 × 3 tactile display using resistive heating-induced bubbles (Fig. 8e).[201] The actuator was configured with a top PDMS membrane, a bottom Au/Cr heater, and an in-between cavity that encloses the driving liquid. When a voltage pulse is applied to the heater, the electrothermal effect drives phase transition, causing the volume to increase and pushing the PDMS membrane upwards, resulting in the generation of haptic feedback. The actuation displacement positively correlates with the energy input. Specifically, an energy supply of 457 mJ (28.7 V, 15 ms) induces a displacement of 60.7 μm. However, the same performance cannot be sustained in the following cycles as the thermal bubbles cannot effectively evanesce. Moving forward, to provide a reliable tactile interface, significant advancements in this technology are required in terms of energy efficiency and cycling performance.

3.3 Magnetic

Magnetic field as a driving stimulus can impart remote actuation to soft tactile actuators, along with precise and rapid control over variables such as magnitude, alignment, phase, and frequency.[204] These soft magnetic actuators typically incorporate magnetic fillers into a soft polymer matrix. These fillers align with the applied field upon exposure to magnetic fields,

triggering actuation. Furthermore, these actuators can be programmed to have a particular magnetization profile, facilitating the realization of intricate shapes and movements.[205,206] To achieve tactile feedback, electromagnetic and magnetorheological actuators are commonly employed, and we highlight their mechanisms and advancements.

3.4.1 Electromagnetic actuators. Commercial tactile actuators, such as eccentric motors and linear resonance actuators, have long utilized electromagnetic principles to deliver tactile feedback. These electromagnetic actuators primarily consist of a permanent magnet and a conductive coil.[207,208] When an electric current flows through the coil, a magnetic field is generated around it, interacting with the magnetic field of the permanent magnet. This interaction between the two magnetic fields results in electromagnetic actuation. These actuators offer advantages like high-frequency vibrations, rapid response, and significant displacements and forces achievable at low voltages.[207,208] However, their inherent rigidity prevents them from emulating the compliant nature of human skin. As a result, research efforts have shifted towards advancing soft electromagnetic actuators.

A direct approach involves integrating conventional electromagnetic actuator designs with a soft membrane layer that interfaces with the skin.[21,209,210] This endows the tactile device with the force outputs typically associated with rigid components while ensuring soft interactions with the skin. To effectively control an array of electromagnetic actuators, electromagnetic shielding is often introduced to prevent crosstalk within the array due to strong interactions between magnets.[209,210] Yu *et al.* integrated near field communication electronics and electromagnetic actuators to achieve a wireless, battery-free platform coupled with haptic interfaces.[211] Haptic actuators were designed by mounting a permanent magnet onto a thin disk of polyimide that acts as a cantilever-like platform, whereas a silicone layer was used to interface with the skin. When time-varying currents are applied to the coil that surrounds the magnet, interactions between the two led to actuation. Guided by computational modelling, varying the material and design parameters, such as the thickness of the polyimide or the slit angle that the magnet is mounted on, allowed the haptic actuator to achieve notable tactile feedback at only 1.75 mW with minimal crosstalk between adjacent actuators. Similar electromagnetic actuators have further been miniaturized to have 5 mm diameter and 1.45 mm thickness, allowing nine actuators to be integrated within a small area and mounted on a thumb tip.[212] The effectiveness of the miniature actuators is seen when utilized for Braille pattern recognition with five testers, at which an 85.4% recognition accuracy was reached for distinguishing seven letters. To accommodate deformations from stretching, bending or twisting within these devices, it is critical to design copper connections with serpentine geometries.[211,212] With the goal of transmitting touch between two users, Li *et al.* realized electromagnetic actuators with both tactile sensing and haptic feedback.[213] When the device is being pressed at a particular speed, the actuator is deformed to change the relative distance between the magnet

This journal is © The Royal Society of Chemistry 2024

Chem. Soc. Rev., 2024, **53**, 3485–3535 | **3505**

and the coil. Based on Faraday's law of electromagnetic induction, a current is generated. When pressure is released, the magnet moves away from the coil, generating an induced current in the opposite direction. These electrical signals can be utilized to provide information on tactile strength and duration. The superior wearability of these electromagnetic actuators mounted on soft silicone is further shown through finite element simulations with no noticeable applied stresses on the skin being found. The effectiveness of these actuators is shown when tested on low sensitivity areas, particularly the back of twelve individuals, at which the recognition accuracy of dynamic patterns reached 88.75%. However, these electromagnetic actuators still predominantly consist of rigid components, which can accelerate failure. This is attributed to the compliance mismatch between soft and rigid components, resulting in stress concentrations at the soft–rigid interface.[214,215] A

possible solution to address this is to introduce modulus graded structures between these components.[214,215]

Soft electromagnetic actuators coupled with fluids have shown promise in enhancing force outputs.[216] This involves a setup where a magnet and an electromagnet are separated by a polypropylene shell that encapsulates fluids (Fig. 9a). Upon applying current, the permanent magnet is drawn towards the electromagnet, compressing the shell, and redistributing the fluid to generate output. This hydraulic amplified soft electromagnetic actuator (HAPSEA) achieved substantial force outputs (1.3 N at 4 A) and displacements (10 μm at 200 Hz, 1 A) capable of stimulating tactile sensations. Moreover, the encapsulated fluid acts as a thermal reservoir, removing heat from the coil and enabling operation at a maintained temperature of 36 °C after continuous 2 A operation. These attributes highlight the potential of the HAPSEA to create safe tactile devices, operating
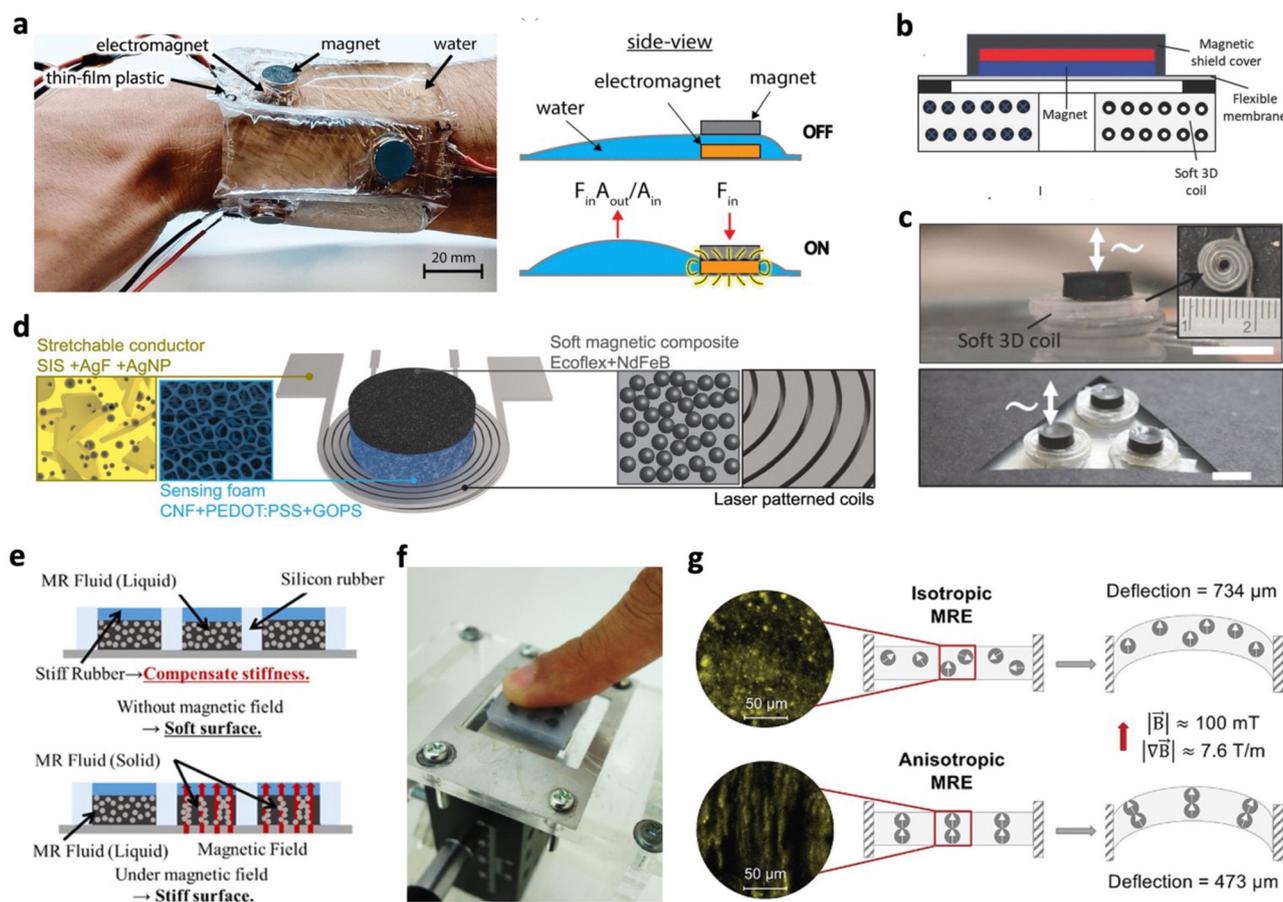

Fig. 9 Magnetic actuators for tactile feedback. (a) Photographs of multiple hydraulically amplified soft electromagnetic actuators (HAPSEAs) (left). Illustration of the operating principle of a HAPSEA (right). Adapted with permission from ref. 216. Copyright 2023, IEEE. (b) Schematic and (c) photograph depicting electromagnetic vibrotactile actuators with a soft coil. Scale bar: 5 mm. (b) and (c) Are adapted with permission from ref. 217. Copyright 2018, Wiley-VCH. (d) Schematic representation of entirely soft haptic electromagnetic actuators composed of stretchable conductors, pressure-sensitive conductive foams, and soft magnetic composites. Adapted from ref. 218 and published by American Chemical Society under Creative Commons CC BY License. (e) Working principle of a magnetorheological fluid (MRF) tactile display with variable stiffness. (f) Photograph of a tactile display during sensory evaluation. (e) and (f) Are adapted with permission from ref. 219. Copyright 2017, IOP Publishing Ltd. (g) Cryo-SEM images of isotropic and anisotropic magnetorheological elastomers (MREs) with nanoparticles (left). Working principle of MREs with soft magnetic particles. Isotropic MREs show that all magnetic moments are aligned in the direction of the electric field (right). Adapted with permission from ref. 220. Copyright 2022, American Chemical Society.

3506 | Chem. Soc. Rev., 2024, 53, 3485–3535

This journal is © The Royal Society of Chemistry 2024

at low voltages (2 V) and temperatures, while offering diverse tactile sensations.

To achieve intrinsically soft electromagnetic actuators, rigid metal coils can be replaced with flexible alternatives such as liquid metal encapsulated in a polymer,[217,221] whereas rigid permanent magnets can be substituted with soft magnetic composites.[222,223] Do et al. demonstrated a vibrotactile actuator utilizing soft coils made of liquid metal injected into a hollow silicone filament (Fig. 9b and c).[217] With these soft coils, the actuator could operate at high frequencies (500 Hz) and low voltages (1 V). To prevent damage from heat generated by larger currents driving electromagnetic actuators, soft coils with higher thermal conductivity were designed by incorporating liquid metal colloids into the silicone matrix. An entirely soft haptic electromagnetic actuator was later demonstrated by utilizing stretchable conductors, pressure-sensitive conductive foams, and soft magnetic composites (Fig. 9d).[218] The soft magnetic composites were fabricated by blending NdFeB microparticles with silicone, followed by a magnetization process. During curing, these particles were oriented in a specific direction using a strong permanent magnet. To counteract the effects of Joule heating, the stretchable conductors were designed with high electrical conductivity and aspect ratios, which was achieved through controlled in situ silver nanoparticle formation and laser patterning, respectively. Furthermore, the incorporation of pressure-sensitive conductive foams endowed the actuator with sensing capabilities and introduced an additional parameter (foam thickness and stiffness) for adjusting the device resonance frequency. This comprehensive approach highlights the synergy between components to create a completely soft electromagnetic actuator with enhanced performance attributes.

Despite the advancements of soft electromagnetic tactile devices, operating at elevated currents to achieve high actuation performance may lead to complications. If heat dissipation remains inadequate, it can elevate the device temperature due to Joule heating, potentially causing thermal damage to soft components or discomfort to the skin.[217,218] Thus, soft materials with elevated thermal conductivity may be introduced to enable the safe and efficient operation of soft electromagnetic tactile devices.

3.4.2 Magnetorheological actuators. Magnetorheological (MR) materials typically have magnetic particles embedded within a soft non-magnetic matrix. These materials are categorized based on the non-magnetic matrix employed, including MR fluids (MRFs),[219,224] MR elastomers (MREs),[220,225] MR gels,[226] MR grease,[227] and MR foams.[228] When subjected to a magnetic field, the magnetic particles align themselves with the field, resulting in alterations in their properties, including rheological and mechanical characteristics. Due to these features, MR actuators have often been employed to generate tactile feedback.

Several studies have showcased the utility of MR actuators in tactile displays with tuneable surface stiffness by varying magnetic fields. For instance, Ishizuka et al. developed displays with high stiffness resolution (5 mm) by incorporating an array

of encapsulated MRFs within silicone rubber chambers (Fig. 9e).[219] In this setup, each chamber acted as a Braille dot, and increasing the magnetic field strength transitioned the dot stiffness from that resembling healthy (33 kPa) to diseased breast tissues (93 kPa). Sensory trials demonstrated that volunteers could perceive the approximate position of the stiff dots (Fig. 9f), indicating the potential application of such stiffness displays in minimally invasive surgery systems designed for palpating and detecting small tumors. While MRFs offer rapid response, noiseless operation, resistance to small content of dust and contaminants, and substantial stress improvements, particular challenges limit their use in tactile displays.[229] These challenges encompass the requirement for containers to seal the liquids, limiting flexibility and design options. Additionally, sedimentation is caused by the density mismatch between the magnetic particles and the fluid, limiting long-term performances. To address these challenges, researchers have turned to solid carrier media like MREs.

The influence of magnetic particle size and alignment on the actuation performance of MREs was investigated by Cestarollo et al.[220] Anisotropic MREs with nanoparticles were observed to achieve larger actuation displacements compared to MREs with larger magnetic microparticles. This was attributed to the higher flexibility of thinner nanoparticle chains formed during magnetic alignment. In contrast, isotropic MREs showed minimal dependence on particle size due to their random dispersion. In the context of soft magnetic particles, isotropic MREs demonstrated better actuation displacement than anisotropic MREs, primarily due to the greater contribution from magnetic particles whose moments can all align with the applied field (Fig. 9g). Utilizing an optimized nanoparticle based isotropic MRE, a refreshable Braille interface was successfully demonstrated. When designing MRE tactile displays for practical applications, providing users with sufficient access space is crucial. Alkhalaf et al. addressed this by applying magnetic fields perpendicularly to the loading direction.[225] While this configuration led to lower MR effects, bilayer composites consisting of MRE and non-MRE layers effectively compensated for this loss. By varying the combinations of MRE and non-MRE layers, the initial modulus of the composite could be tuned to mimic various biological tissues.

However, there are trade-offs to consider in advancing MRE actuators for tactile feedback. To achieve a wide range of tactile sensations, MRE actuators should have both high absolute (difference in modulus between on and off states) and relative (percentage change from the initial modulus) MR effects. However, it is generally observed that MRE actuators with soft matrices only display high relative MR effects.[230,231] When MREs have a strong polymer network, the mobility of particles with the magnetic field becomes limited, leading to lower MR effects. This will be a critical factor to address especially when designing durable MRE tactile actuators. Additionally, MRE devices tend to require substantial power consumption for magnetic saturation, leading to the use of bulky power sources and limited portability. These challenges represent areas for further development of MREs for tactile feedback applications.

This journal is © The Royal Society of Chemistry 2024

Chem. Soc. Rev., 2024, **53**, 3485–3535 | 3507

4. Approaches to durable actuators

Practically, to expand the use of soft tactile actuators in the real world, these devices need to be durable to achieve long operation lifetime and stability.[9,232] Improving the lifetime of these devices will minimize the production of electronic waste, avoiding the mistakes from traditional actuators technology.[9] These devices should be durable in terms of withstanding and recovering from damage, maintaining operation after exposure to moisture and dirt, and achieving stable performance under various environmental temperatures. This section will discuss the approaches to realizing durability, highlighting soft actuators with self-healing, damage-resistant, self-cleaning, and temperature-stable features. Also, material strategies will be introduced to guide the design of soft tactile actuators to achieve elevated durability.

4.1 Self-healing actuators

Tactile actuators are highly susceptible to physical damage due to their soft nature, making them vulnerable to punctures, cuts and overloading.[9,10] Apart from this mechanical damage, dielectric breakdown commonly occurs for electrically driven actuators due to high operating voltages.[17,233] Once damaged, these actuators lose their functionality and are discarded. This leads to more waste generation that is detrimental to the environment, repeating the mistakes of traditional electronics. To circumvent this, imparting soft actuators with self-healing capabilities is promising, enabling the continued operation of the actuator after damage. Herein, we highlight the diverse approaches to design self-healable soft actuators and their potential application for tactile devices. In addition, given the potential of electrical actuators for tactile applications, self-healing after dielectric breakdown will be included in the scope of this section.

4.1.1 Design of self-healing actuators. To recover from mechanical damage such as cuts, punctures, and tears, various works have applied self-healing polymers to soft actuators, enabling them to regain their performance.[234] Self-healing can be classified as either extrinsic or intrinsic. Extrinsic self-healing relies on healing agents stored within microcapsules or vascular networks that, when ruptured, are released at the damaged region to trigger a healing reaction. However, microcapsules are often limited to a single healing operation since the healing agents are depleted upon release. On the other hand, vascular networks allow for multiple healing operations but require challenging and time-consuming fabrication.[235,236] As a result, extrinsic healing mechanisms have found limited applications for soft actuators. In contrast, intrinsic self-healing does not require healing agents and depends on the physical movement of polymer chains at the damaged site and the rearrangement of reversible bonds. These reversible bonds may be distinguished as supramolecular interactions or dynamic covalent bonds, with the main difference being their binding energies (Fig. 10a).[237] Thus, the mechanical properties of self-healing polymers are determined by both the type of the reversible bond and the crosslinking densities. For deeper

insights into the chemical reactions of these reversible bonds for self-healing polymers, readers may refer to extensive reviews by Yang *et al.*[238–240] and Chakma *et al.*[241] With increasing work being focused on developing novel self-healing polymers, soft actuators have been identified as a potential application of these materials. In Table 3, we present the self-healing capabilities of some of these actuators. However, self-healing soft actuators are in the nascent stages, at which we discuss the various strategies that have adapted these materials for soft actuators.

Self-healing through supramolecular interactions can provide fast healing, usually under ambient conditions or with diverse stimuli such as solvents and mild temperatures. These interactions for self-healing polymers include hydrogen bonding,[246,257] metal–ligand coordination,[258,259] host–guest interaction,[260] hydrophobic association,[261] ionic interactions,[262] and π–π stacking.[263] Realistically, self-healing actuators should recover their properties rapidly with minimal performance loss. Pena-Francesch *et al.* designed squid-inspired biosynthetic proteins with hydrogen-bonded cross-linking nanostructures.[242] Proteins were hydrated to enable the diffusion of polymer chains, and during self-healing, proteins retained their physical crosslinks without needing to melt and reform. This was key to maintaining mechanical stability and ensuring the rapid recovery of their properties during healing. Under mild temperatures, healing was accelerated due to greater chain mobility, with bisected samples healed in under 1 second at 50 °C. Moreover, when applied as a pneumatic actuator, minimal changes were observed in actuation displacements and force outputs before and after recovering from puncture damage (Fig. 10b and c). In most cases, these self-healable supramolecular polymers cannot be effectively healed in water. Water molecules may disrupt the reconnection of physical interactions for healing through saturating hydrogen bonds, coordinating with metal cations, or solvating ions.[17,264,265] This is crucial to address for tactile devices that may encounter sweat or high humidity. To overcome this, hydrophobic polymers with supramolecular interactions have been utilized.[243,257,265,266] Zhang *et al.* developed an ionic conductive elastomer with underwater healing capabilities.[243] The elastomer was based on PVDF-HFP, which contains CF_3 dipoles and hydrophobic multication ionic liquids (Fig. 10d). Due to the strong ion–dipole interactions and hydrophobic design, the polymer can heal underwater or in saline solution, regaining 34% of its mechanical toughness in both cases. Remarkably, when broken parts were immersed in water for two weeks before being brought together in the air to heal for 24 hours, 66% of the mechanical toughness was repaired. With ionic conductivity, the elastomer was utilized as a self-healable electrode for DEAs and exhibited complete restoration of actuation performance after underwater healing, even when the electrode was bisected (Fig. 10e).

To advance the use of self-healing polymers for soft actuators, it will be advantageous to utilize functional groups that impart self-healing capabilities and enhance actuation performance simultaneously. For instance, functionalities that form

3508 | *Chem. Soc. Rev.*, 2024, **53**, 3485–3535

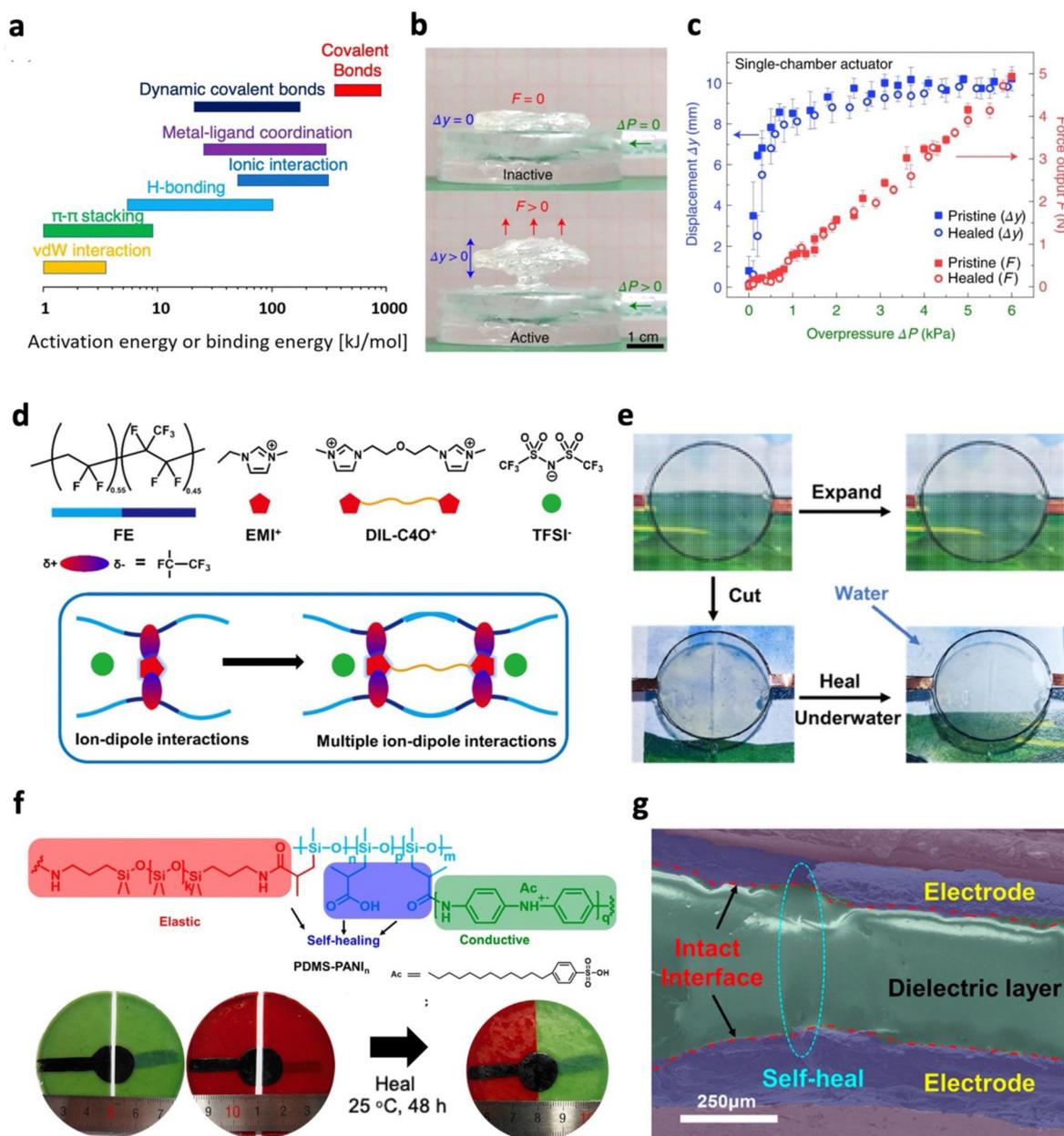This journal is © The Royal Society of Chemistry 2024

Fig. 10 Self-healing actuators based on supramolecular interactions. (a) Activation energy or binding energy of various bonds and interactions. Adapted with permission from ref. 237. Copyright 2021, American Chemical Society. (b) Photograph of inactive and active single-chamber pneumatic actuators composed of synthetic proteins. (c) Actuation performance of the pneumatic actuator before and after puncture, showing complete performance recovery. (b) and (c) Are adapted with permission from ref. 242. Copyright 2020, Springer Nature. (d) Schematic illustrating multiple ion–dipole interactions between poly(vinylidene fluoride-co-hexafluoropropylene) (FE) and multication ionic liquids. (e) Photograph of a DEA with self-healable ionic electrodes capable of underwater healing. (d) and (e) Are adapted with permission from ref. 243. Copyright 2020, American Chemical Society. (f) Chemical structure of self-healable polydimethylsiloxane with carboxylic acid and polyaniline functional groups (top). Photograph depicting bisected DEAs brought together for self-healing (bottom). (g) Digitally rendered SEM image of self-healed DEAs showing bonding of the bisected electrode and dielectric layers. (f) and (g) Are adapted with permission from ref. 244. Copyright 2020, American Chemical Society.

supramolecular interactions are often polar in nature, providing films with a higher dielectric constant.[86,244,246] This is advantageous for DEAs as having a high dielectric constant generates large Maxwell pressures for elevated actuation performance. Thus, a wide variety of supramolecular elastomers have been applied to achieve self-healing DEAs.[86,244–247,258,267–271] While works on self-healing DEAs have focused on either the self-healable electrodes or the dielectric layer, Duan et al. developed a self-healing DEA based on hydrogen bonding, with carboxyl groups playing a vital role in achieving high dielectric constants (7.6 @ 50 Hz) and facilitating self-healing.[244] By tuning polyaniline (PANi) content in the

This journal is © The Royal Society of Chemistry 2024

Chem. Soc. Rev., 2024, 53, 3485–3535 | 3509

Table 3 Performance of various self-healing actuators based on supramolecular interactions or dynamic covalent bonds

Bonding type	Elastic modulus (MPa)	Healing condition	Healing efficiency	Actuator type	Recovered actuation (mechanical damage)	Ref.
Supramolecular (hydrogen bond)	0.08	80 °C, 5 h	115% (σ_b), 85% (W_r)	DEA	70%	245
Supramolecular (hydrogen bond)	1.49	RT, 12 h, IPA addition	59% (σ_b), 80% (S_b), 56% (W_r)	DEA	93%	246
Supramolecular (electrostatic interaction)	2.4	RT, 72 h	27% (S_b)	DEA	46%	247
Supramolecular (hydrogen bond)	2.4	50 °C, 1 s, hydrated	N. A	Pneumatic	100%	242
Supramolecular (halogen bond)	3	80 °C, 5 min	60% (W_r)	LCE	N. A	248
Supramolecular (hydrogen bond)	N. A	40 °C, 48 h	76% (σ_b), 92% (S_b)	LCE	95%	249
Supramolecular (hydrogen bond)	N. A	RT, 24 h	65% (S_b)	MRE	N. A	250
Dynamic covalent (Diels–Alder)	5	80 °C, 40 min	98–99% (E')	Pneumatic	∼95%	251
Dynamic covalent (Diels–Alder)	0.5	70 °C, 30 min	92% (σ_b), 94% (S_b)	Pneumatic	∼131%	252
Dynamic covalent (disulfide bond)	0.11	180 °C, 3 h	80% (S_b)	LCE	N. A	253
Dynamic covalent (diselenide bond)	2.48	120 °C, 2 h	57% (σ_b), ∼100% (S_b)	LCE	N. A	254
Dynamic covalent (boronic ester bond)	N. A	80 °C, 24 h	100% (σ_b)	SMP	N. A	255
Supramolecular and dynamic covalent (hydrogen bond and disulfide bonds)	1.76	RT, 3 h	96% (S_b)	DEA	∼116%	256

∼: Estimated from figures; N.A.: not available; σ_b: tensile strength at break; S_b: tensile strain at break; W_r: work to rupture (mechanical toughness); E': storage modulus; DEA: dielectric elastomer actuator; LCE: liquid crystal elastomer; MRE: magnetorheological elastomer; SMP: shape memory polymer.

matrix, elastomers with even higher dielectric constants (11.11 @ 50 Hz) at 2.5 wt% and conductivity (4.5×10^{-5} S cm^{-1}) at 20 wt% were obtained, serving as the dielectric layer and electrodes, respectively. Since these components were made from the same matrix, robust interfaces formed, allowing polymer chains to diffuse and promote healing between damaged regions (Fig. 10f and g). Although the healed DEAs exhibited slightly lower actuation performances than pristine ones, actuation strains of 1.62% at 15.8 V μm^{-1} can still be achieved. Supramolecular interactions play another vital role in enhancing self-healing actuators by interacting with fillers. These fillers are essential for soft actuation, providing functionalities like magnetic and photothermal effects.[259,272–274] Within self-healing actuators, supramolecular interactions can easily facilitate the coupling of fillers to the polymer matrix, enabling effective filler dispersion and mechanical reinforcement, thereby enhancing soft actuators.[259,263,272–274]

Dynamic covalent bonds (DCBs) have higher mechanical strength and stability compared to supramolecular interactions due to their higher binding strengths. As a result, external stimuli like elevated temperatures are often required to provide sufficient energy to enable self-healing. Examples of DCBs in self-healing polymers are imine bonds,[275,276] oxime bonds,[277,278] disulfide bonds,[256,264] thioester bonds,[279] boronic ester bonds,[275,280] and Diels–Alder (DA) reactions.[251,281] Comprehensive studies on the application of DA polymers for self-healing pneumatic actuators have been performed by Terryn et al.[251,282–284] Owing to improved control over the self-healing process with heat as a trigger, DA polymers were selected. The self-healing process of these actuators was split into five steps – damage, heating, isothermal heating, controlled cooling, and recovery at room temperature (Fig. 11a).[251,282] When heated, retro-DA reaction occurs, causing scission of crosslinks to form furan and maleimide functional groups. Under isothermal conditions (80 °C), polymer chain mobility is promoted with

more broken crosslinks and, when given sufficient time, can seal the damage. The crosslinks are reformed upon cooling as DA reaction occurs, restoring the initial properties. Once ambient conditions are reached, a long waiting time (24 h) is provided. By controlling the cooling rate and allowing a long waiting time at ambient temperature, a balance is achieved between the kinetics of bond formation, which decelerates with decreasing temperature, and the thermodynamic driving force for bond formation. Following this procedure, pneumatic actuators were found to recover from damage, showing minimal changes to actuation after multiple healing cycles (Fig. 11b). Based on these DA reactions, robust interfaces between DA polymers with different properties can also be formed, expanding the designs of soft actuators.[251,284,285] This was demonstrated by Gomez et al., who relied on the dynamic exchange of thioether moieties to achieve a 3D printable self-healing pneumatic actuator.[286] Starting from a mixture of thiol and acrylate monomers, elastomers were formed based on step-growth thiol–acrylate polymerization and chain-growth acrylate homopolymerization occurring concurrently. Increasing the amount of thiol reduced the crosslinking density due to patching abstraction-based intermolecular side reactions. This improved self-healing capacity after thermal treatment of 90 °C for 24 h, highlighting the importance of designing for chain mobility. Also, 3D printed modular components could be healed together to build the pneumatic actuator.

Owing to their thermal stability, DCBs have been extensively applied in LCEs.[254,280,287–290] As thermal effects often trigger these polymeric actuators, it is crucial to tune actuation temperatures to be far from the self-healing temperature. When rapid bond exchange and actuation are occurring concurrently, actuation stability important for tactile applications may be compromised.[288,289] Based on thiourea linkages, Lee et al. designed a robust LCE that showed reprocessability, self-healing and reprogrammable actuation.[287] Isotropization

3510 | Chem. Soc. Rev., 2024, 53, 3485–3535

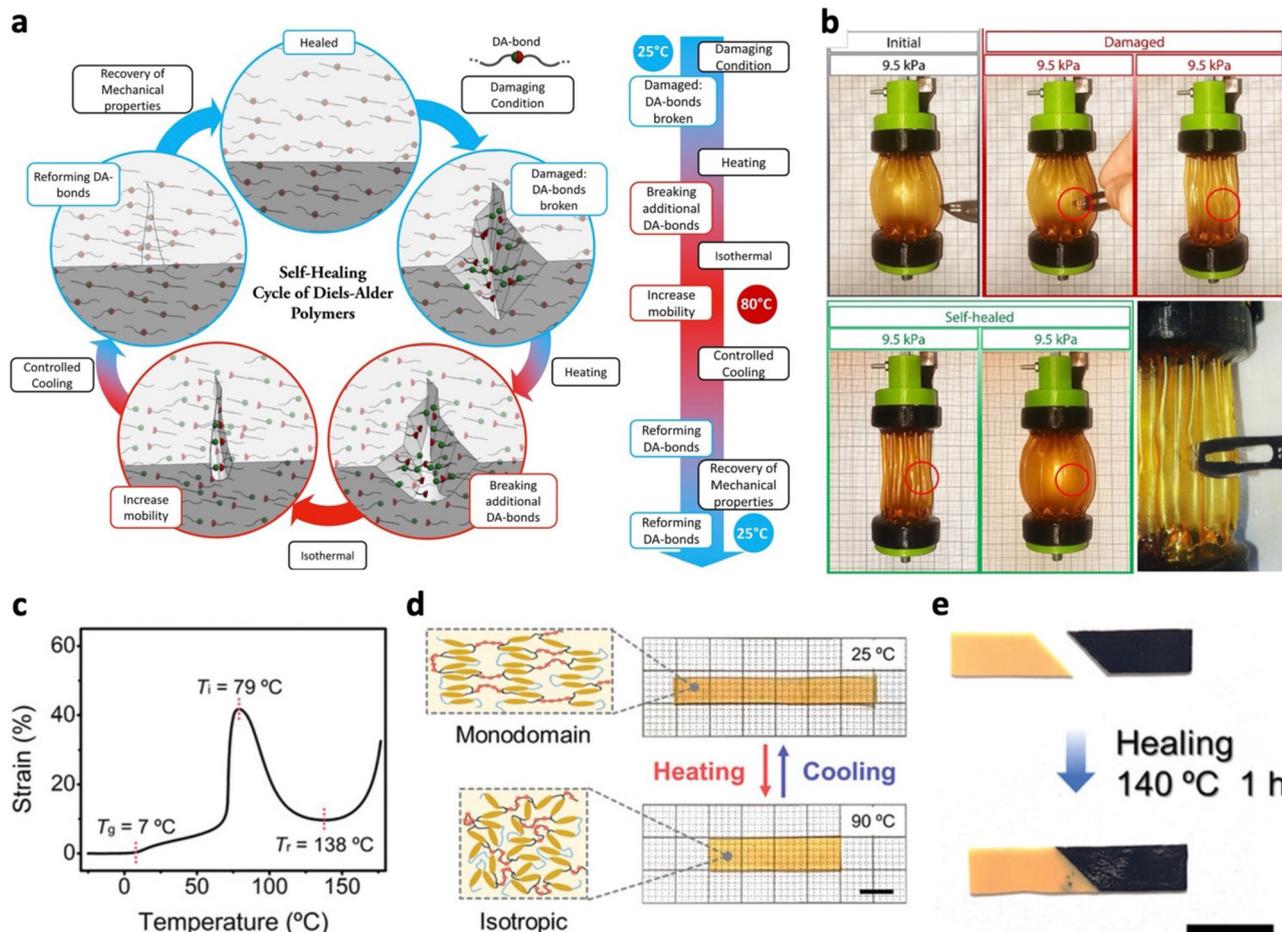This journal is © The Royal Society of Chemistry 2024

Fig. 11 Self-healing actuators with dynamic covalent bonds. (a) Illustration depicting the self-healing process of Diels–Alder polymers. (b) Operation of pleated pneumatic artificial muscle after healing from damage caused by puncture, showcasing regained actuation functionality. (a) and (b) Are adapted with permission from ref. 251. Copyright 2017, The American Association for the Advancement of Science. (c) Iso-stress curve obtained from dynamic mechanical analysis, revealing key temperature points including glass transition (T_g), isotropization (T_i) and reprocessing temperatures (T_r). (d) Thermal actuation and (e) self-healing of a liquid crystal elastomer. (c) and (e) Are adapted with permission from ref. 287. Copyright 2021, Wiley-VCH.

temperature and reprocessing temperature were found to be 79 °C and 138 °C, respectively, allowing stable thermal actuation of monodomain LCEs to take place under repeating heating (90 °C) and cooling (30 °C) (Fig. 11c and d). When cut into two and heated to 140 °C for 1 h (Fig. 11e), the healed LCE could restore 60% of its original tensile strength due to the dynamic nature of thiourea linkages.[287,291] In cases where temperature to trigger bond exchange is not preferred, other triggers such as water[280,290] and light[253,292] can be adopted. LCEs with dynamic covalent boronic ester bonds have shown self-healing with the assistance of water at room temperature by undergoing hydrolysis and dehydration, preventing the temperature overlap of bond exchange and actuation.[280,290] To enable autonomous self-healing, various works have designed polymers and soft actuators with DCBs that can be healed under ambient conditions.[256,281,293] Diarylbibenzofuranone and disulfide bonds were such DCBs that can heal at room temperature due to their lower bond dissociation energies.[256,293,294] Terryn *et al.* lowered the healing temperature

of pneumatic actuators towards room temperature by enhancing the chain mobility of DA polymers.[281] This was realized by increasing the molecular weight of monomer units, reducing DA crosslinks. After severe damage (cut into half) full recovery of actuation performance was attained within 7 days at room temperature.

Apart from mechanical damage, soft actuators may suffer from electrical damage from dielectric breakdown, particularly those driven by high electric fields including DEAs, electrohydraulic actuators as well as piezoelectric and electrostrictive actuators.[17,233] Thus, various self-healing strategies have emerged to enable soft actuators to continue their operation after electrical damage. When breakdown occurs, voltage is discharged between the two electrodes, leading to localized heating and vaporization of the material.[233] To address this, self-clearing electrodes have been adopted. During self-clearing, dielectric breakdown causes decomposition of the electrodes surrounding the defect site, isolating it from the active area for continued operation (Fig. 12a and b).[66,233,295]

This journal is © The Royal Society of Chemistry 2024
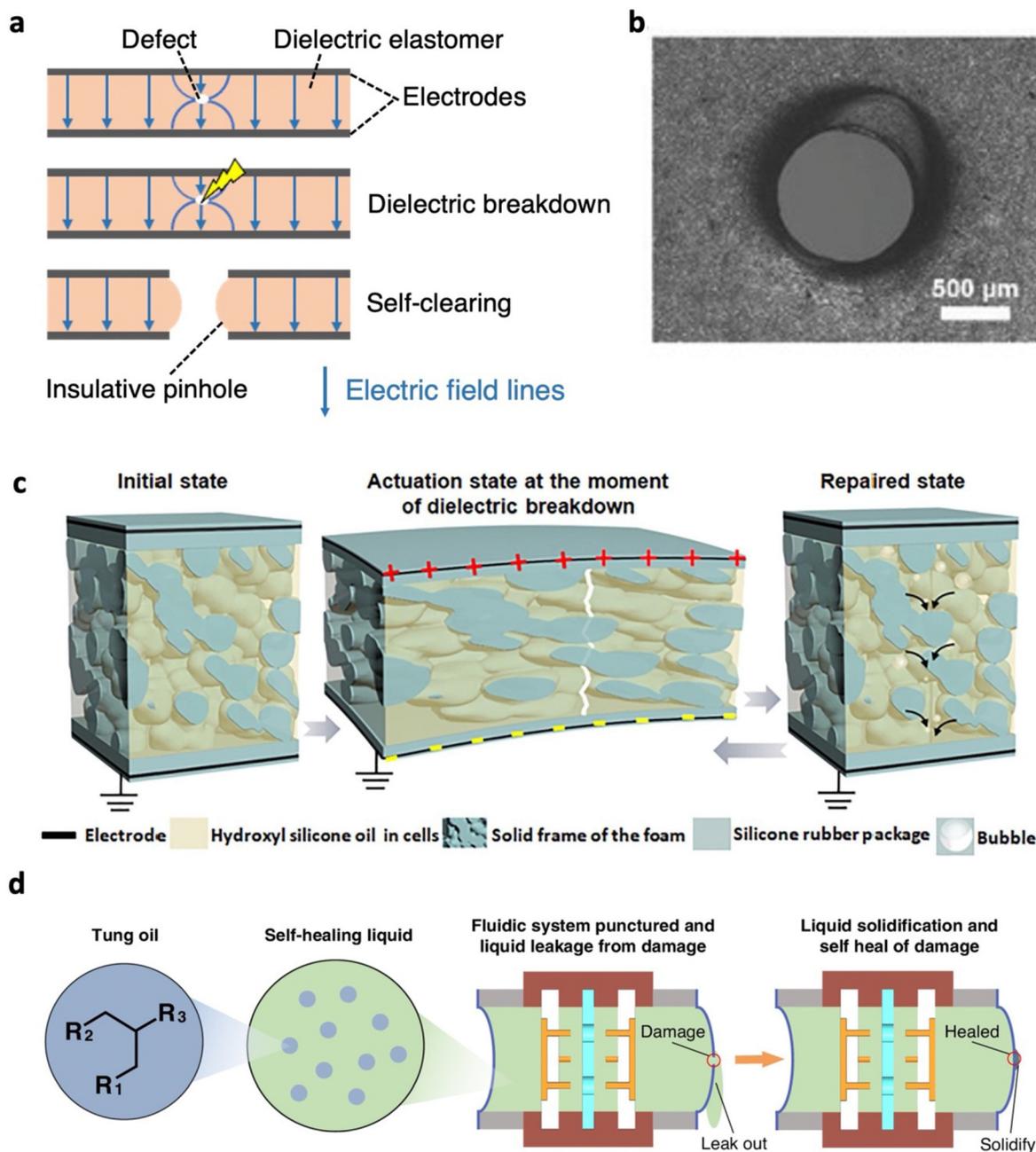
Chem. Soc. Rev., 2024, **53**, 3485–3535 | 3511

Fig. 12 Soft actuators that self-heal after electrical damage. (a) Working principle of self-clearing electrodes. (b) Microscopic image showing a hole formed after undergoing the self-clearing process. Adapted with permission from ref. 295. Copyright 2020, Wiley-VCH. (c) Self-healing mechanism of a DEA with liquid–solid interpenetrating structures. Adapted with permission from ref. 299. Copyright 2021, Elsevier Ltd. (d) Schematic illustrating a self-healing pump that utilizes tung oil to seal damage sustained in the shell, preventing liquid leakage. Adapted from ref. 302 and published by Springer Nature under Creative Commons CC BY License.

These electrodes should be uniformly distributed, have high electrical conductivity and be thin enough for rapid decomposition around the defect site, allowing self-clearing to take place. DEAs have often applied single walled carbon nanotube (SWCNT) electrodes to achieve such self-cleaning effects.[66,296,297] While high actuation performance has been attained with these self-clearing electrodes, the sharp tips of nanotubes may induce corona discharge through the surrounding air that reduces conductivity and actuation performance after multiple self-clearing events. For improved actuation stability, works have coated dielectric oil and water-based polyurethane on SWCNT layers to suppress corona discharges.[295,298] Compared to mechanical damage, electrical damage typical leads to a loss of the dielectric material to form pinholes due to vaporization at breakdown sites. A direct approach to recover from such damage is to use self-healing

polymers as actuators, apply pressure manually to seal the damage, and administer the required healing conditions.[246,269] Another strategy is to employ solid–liquid dielectrics that rely on the flow of dielectric liquids to fill the damaged regions, while solid polymers provide structure. This may take form as an open-cell polymer foam infiltrated with a dielectric liquid.[299,300] Xu et al. designed a DEA with a composite dielectric layer consisting of silicone foam filled with hydroxyl silicone oil, encapsulated within a silicone rubber shell.[299] When dielectric breakdown occurs, the DEA shrinks from its actuated state, driving hydroxyl silicone oil to fill the damage areas (Fig. 12c). As a result, the DEA could sustain multiple dielectric breakdown events, extending its reliability and lifetime. Compared to solid silicone rubber DEAs, the composite DEA exhibited three times higher actuation strains at 25 V μm^{-1}, due to hydroxyl silicone oil that lowered the modulus and increased the dielectric constant. Alternatively, dielectric liquids can be encapsulated in a polymer shell, a structure adopted by HASEL actuators.[94,96,301] Similarly, when dielectric breakdown occurs in the liquid, the liquid redistributes to revert the actuator back to the insulating state. However, for HASEL actuators to achieve longer lifetime, the encapsulating polymer shell can be imparted with self-healing capabilities to prevent liquid leakage from dielectric breakdown. This may be possible by using intrinsic self-healing polymer shells or special functional liquids. Tang et al. demonstrated a self-healing electro-hydrodynamic pump by mixing tung oil with dibutyl sebacate to form the dielectric liquid.[302] When tung oil is exposed to air upon damage of the shell, a solid film is formed as conjugated carbon–carbon double bonds combine with oxygen to undergo free radically initiated homopolymerization. The film formation seals the damage in the shell, preventing further fluid leakage (Fig. 12d).

4.1.2   Practical application of self-healing actuators. While various approaches for self-healing actuators have been developed, practical application of these actuators for tactile devices requires minimal manual intervention. Generally, in the case of large damage within the soft actuator, broken surfaces are manually brought into contact for self-healing to occur. To automate this process, shape memory assisted self-healing (SMASH) is commonly employed, utilizing shape memory effects (SME) to achieve crack closure through shape recovery. However, many shape memory materials exhibit one-way SME, requiring external programming after each healing event to regain SME.[303–305] Fan et al. overcame this limitation by using a two-way shape memory polymer. Their work demonstrated the closure of wide cracks and repeated self-healing without intervention after each healing event.[306] In the polymer composed of crosslinked polycaprolactone based semicrystalline polyurethane (PU) and styrene-butadiene-styrene (SBS) block copolymer elastomer blend, two-way SME was driven by thermally triggered reversible bidirectional transformation of the crystalline phase PU and compressed SBS.[306,307] SME allowed the crack to be closed autonomously and the healing process was facilitated by synchronous fission/radical recombination of dynamic covalent C–ON bonds from alkoxyamine added onto the PU backbone. With two-way SME, the elastomer could even

undergo cutting, autonomous crack closure and healing continuously at the same location with no re-programming (Fig. 13a), achieving 58.5% healing efficiency after three cycles. Another approach to bring damaged parts into contact autonomously involves applying magnetic forces. The magnetic force may be generated by an external magnetic source,[308,309] or be based on the inherent attraction between hard magnetic particles.[310,311] Garica-Gonzalez et al. proposed a concept for autonomous self-healing MREs by embedding hard magnetic particles in a sticky ultra-soft elastomer matrix.[311] The attraction forces between these hard particles promoted crack closure, and dipole–dipole interactions between particles enabled immediate self-healing. Moreover, combinations of soft and hard magnetic particles were explored, observing a synergistic effect where soft particles enhanced magnetization by generating magnetic bridges, thereby improving the healing performance. For further enhancement of healing performances, this concept may be applied in tandem with self-healing polymers.

To enable or accelerate self-healing effects in soft actuators, external stimuli are applied by systems such as ovens[251,286] and NIR lamps.[86] This approach necessitates manual placement of damaged actuators into these systems for the self-healing process to take effect. Furthermore, the lack of localized stimulus application in these external systems reduces energy efficiency and potential interference with neighbouring components. As soft tactile actuators are being increasingly used for wearables, these systems are required to be portable. To solve these issues, stimuli providing systems can be integrated directly into or onto self-healing actuators. Among the various stimuli options, heat is commonly used to trigger self-healing and Joule heating has emerged as a popular choice due to its localized heating capability and portability. Joule heating can be achieved by introducing conductive agents such as CNTs,[306,313] liquid metal,[314] and shape memory alloy wires[315] into self-healing actuators. These conductive components can also provide additional functionality to self-healing actuators; for example, Tabrizian et al. embedded shape memory alloy wires into a self-healable pneumatic actuator. These shape memory alloy wires perform three roles: assisting with damage closure when shape memory is activated, providing Joule heating effects to accelerate healing, and constraining radial expansion and longitudinal extension to achieve bending motions.[315] When conductive agents are embedded into the actuator, filler volume fraction and dispersion must be sufficiently high to form percolative networks for effective electrical conduction.[316] However, in some cases, embedding these conductive components may be unwanted as actuation properties may be compromised from increased stiffness or conductivity.[70] To overcome this, healable heaters may be integrated onto these self-healing actuators.[317] The electrical conductivity of these components also presents the opportunity for sensing capabilities for automated heat stimulation using a microprocessor. For instance, when damage occurs, the sudden increase in electrical resistance is detected that triggers Joule heating for self-healing (Fig. 13b).[306,318] As such, manual intervention can further be eliminated, automating the healing process entirely.

This journal is © The Royal Society of Chemistry 2024

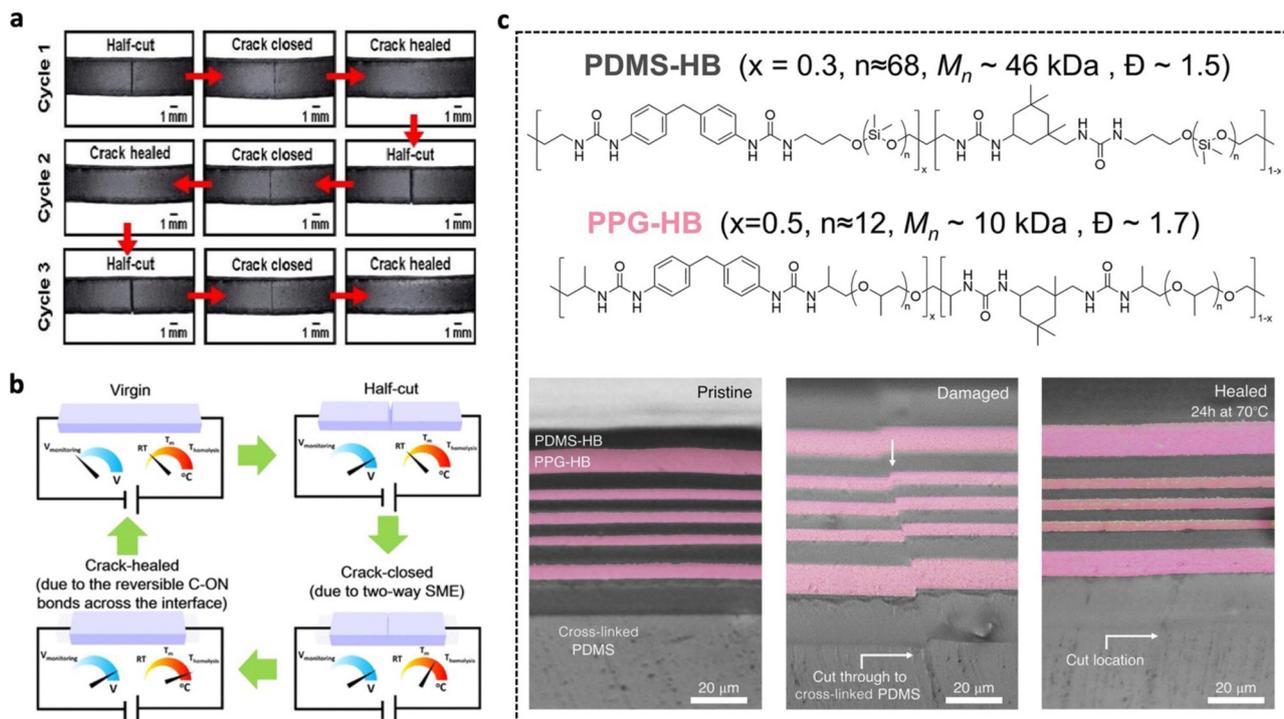Chem. Soc. Rev., 2024, **53**, 3485–3535 | **3513**

Fig. 13 Strategies for minimal external intervention in self-healing. (a) Photograph illustrating the repeated closure of cracks induced by shape memory effects, where damaged parts are naturally brought together for self-healing. (b) Activation of Joule heating to facilitate self-healing, triggered by an increase in electrical resistance during damage. (a) and (b) Are adapted from ref. 306 and published by American Chemical Society under Creative Commons CC BY License. (c) Chemical structure of polydimethylsiloxane (PDMS) and polypropylene glycol (PPG) based polymers with immiscible backbones that share the same type of dynamic bonds. (Top) Optical microscope images of a multilayer film composed of PDMS and PPG based polymers with immiscible backbones, demonstrating autonomous re-alignment of damaged parts (bottom). Adapted with permission from ref. 312. Copyright 2023, The American Association for the Advancement of Science.

When damaged parts are brought into contact, perfect alignment of damage parts is crucial to ensure that the majority of their properties are recovered during the healing process. This becomes even more challenging when tactile actuators incorporate multiple layers to achieve higher force outputs or additional functionalities. To tackle this issue, Cooper et al. proposed a novel approach utilizing two polymers with immiscible backbones but sharing the same dynamic bonds (Fig. 13c).[312] These immiscible polymers were stacked alternatingly to form multilayer films, which would become misaligned upon damage. To minimize the interfacial free energy, directional chain diffusion occurred, allowing autonomous alignment during healing to be achieved. By having similar dynamic bonds, strong interlayer adhesion can be attained between immiscible layers, ensuring optimal performance of stretchable devices. Furthermore, by embedding dielectric, magnetic, and conductive particles into these polymers, various stretchable electronic devices were demonstrated with autonomous alignment capabilities.

The development of self-healing actuators for tactile stimulation holds immense potential to extend operation lifespan, thereby slowing down the consumption of natural resources and minimizing waste accumulation. Moving forward, by automating the healing process, which includes crack closure, alignment, and stimuli application, consistent healing outcomes and added convenience are achieved, encouraging greater commercial adoption.

4.2 Damage-resistant actuators

Soft tactile actuators often come into direct contact with their surroundings to generate tactile feedback, raising the probability of sustaining damage from external factors. When applied as wearables, they may face bending, stretching and impacts even when not operated. The common type of damage within soft tactile actuators includes cuts, tears, and puncture causes by sharp objects, as well as fatigue resulting from cyclic deformations. Also, soft actuators driven at high voltages are prone to dielectric breakdown. While a significant amount of effort has focused on recovering from this damage through self-healing effects, repeated damage may lead to inevitable deterioration of performance over time. Thus, it is equally critical to prioritize preventive measures to avoid pre-mature damage altogether. In this context, we categorize preventive measures into two key areas: mechanical and electrical damage resistance, discussing their principles and approaches employed. Additionally, we include innovative material designs that hold promise in achieving damage-resistant actuators.

Mechanical and electrical failure are often caused by defects within the soft actuators. This begins at the processing stage of polymers, influencing their final quality.[319] To remove trapped

air bubbles, polymer mixtures are degassed in vacuum. Furthermore post curing of fabricated films is required to remove residual volatiles that impact long-term mechanical and electrical stability.[320] If inorganic fillers are to be mixed into the polymer, prior sonication of the fillers in a liquid medium should be performed to break agglomerates. When dispersed into the polymer, fillers must be well dispersed to prevent the formation of defects that can accelerate both mechanical and electrical failure.

4.2.1 Tolerance to mechanical failure. Soft actuators composed of materials with high mechanical toughness tend to better resist puncture, cuts, and tears. Here, mechanical toughness also known as the work to rupture is defined as the ability to absorb mechanical energy and deform without failure. This is derived from the area under the stress–strain curve and the material is assumed to be insensitive to small flaws. However, after experiencing the initial damage (puncture, cuts, and tears), flaw sizes are increased leading to flaw-sensitive rupture. To resist the propagation of cracks (large flaws) that leads to rupture, soft actuators should be imparted with high fracture toughness. Chen et al. showed that this transition from flaw insensitive to flaw sensitive rupture depends on a material-specific length, that is the ratio between fracture and mechanical toughness.[321]

Efforts to enhance mechanical and fracture toughness have typically focused on imparting energy dissipation mechanisms within polymer networks.[16,322,323] This includes introducing sacrificial bonds that break before the covalent bonded backbone or incorporating high functional crosslinks that accommodate hidden lengths.[322–324] Sacrificial bonds such as physical crosslinks or dynamic covalent crosslinks may further impart self-healing capabilities, allowing both damage resistance and recovery. However, incorporating these energy dissipation mechanisms for high toughness leads to an inevitable increase in hysteresis. This may narrow the frequency bandwidths of soft tactile actuators, limiting the range of tactile feedback. To address this, polymers with weak and strong reversible bonds are introduced.[246,325] At low strains, strong bonds are maintained, remaining as crosslinks that suppress contributions to hysteresis. When high strains and stresses are experienced, these reversible bonds are broken to dissipate energy, achieving high toughness for resisting damage and crack propagation. However, the introduction of strong reversible bonds leads to an increase in modulus at low strains due to their contribution to the crosslinking density,[16] limiting the actuation performance. We addressed this through modulating the modulus of liquid metal (LM) nanocomposite DEAs through photothermal effects (Fig. 14a).[86] Carboxyl hydrogen bonds within the nanocomposite provided high mechanical toughness, self-healing capabilities, and recyclability, while LM nanoparticles improved the dielectric constant and imparted photothermal properties. By tuning the intensity of NIR illumination, the dissociation of hydrogen bonds can be controlled, tuning the crosslink density and modulus. As such, under co-stimulation of NIR light and electric field, actuated area strains ($\sim$50%) could be attained at 40% lower electric fields

compared to the pristine. Upon cooling, the DEAs can recover their original mechanical properties, retaining their damage resistance properties. Alternatively, to concurrently achieve low modulus, high mechanical toughness and suppressed hysteresis, optimizing the crosslinking network has been found to be effective.[326,327] For instance, crosslinking agents with varying molecular weight were introduced into the n-butyl acrylate elastomer network.[326] By increasing the crosslinker's molecular weight within the range of 10^4 to 10^5 g mol^{-1}, a more structurally uniform polymer network was realized (Fig. 14b). This resulted in low modulus (0.073 MPa), mechanical toughness (6.77 MJ m^{-3}) and ultimate true strength (32.2 MPa). Selecting a crosslinker with a long aliphatic polyether backbone further suppressed mechanical hysteresis effects as it acted as a spacer among polyacrylate chains, weakening dipole–dipole interactions. The impact of the reduced hysteresis is evident from the dynamic performance of the DEAs. When compared against VHB, the designed polyacrylate network exhibited minimal deterioration in actuated area strain in the frequency range of 1–100 Hz. However, further hysteresis suppression is required to achieve improved actuation performance over a wide frequency range.

Slide ring materials (SRMs) are a distinct category of polymers that possess low modulus, minimal hysteresis, and high toughness.[330,331] These traits hold the potential to enhance the durability and overall performance of soft tactile actuators. These SRMs have unique architectures composed of ring molecules threaded onto polymer chains with bulky end groups.[330,331] Ring molecules such as cyclodextrins (CD) are crosslinked to form figure-eight junctions, creating a topological interlocked network. In response to external forces, these junctions act as mobile crosslinks, capable of sliding along the polymer chain to equalize internal tensions. This phenomenon recognized as the pulley effect is responsible for the low modulus, high stretchability, and J-shaped stress–strain curves of SRMs. Moreover, SRMs with lower CD coverage exhibit minimal hysteresis, permitting the CD crosslinks to slide over longer distances with minimal friction (Fig. 14c).[328] Also, Du et al. suppressed hysteresis effects of slide ring polymers by introducing ionic liquid dispersants.[332] This reduced the aggregation of CDs, enhancing the freedom of sliding and thereby minimizing energy dissipation. Another advantage of SRMs is the improved fracture toughness arising from the ability of crosslinks to slide towards the ends of the polymer chains, away from the crack plane (Fig. 14d).[329,331] This elongates the strand length between crosslinks at the crack tip, resulting in enhanced fracture toughness. Leveraging on these favourable properties, SRMs have been utilized to develop soft actuators based on LCEs and SMPs, achieving improved mechanical durability.[333–335] Furthermore, the incorporation of slidable crosslinks has yielded enhanced actuation strain in LCEs and improved shape memory capabilities in SMPs. The application of SRMs in dielectric elastomer actuators (DEAs) is unsurprising given their low modulus and enhanced mechanical characteristics.[80,336] To enhance dielectric constants, Yang et al. introduced barium titanate (BTO) microparticles to SRMs,

This journal is © The Royal Society of Chemistry 2024
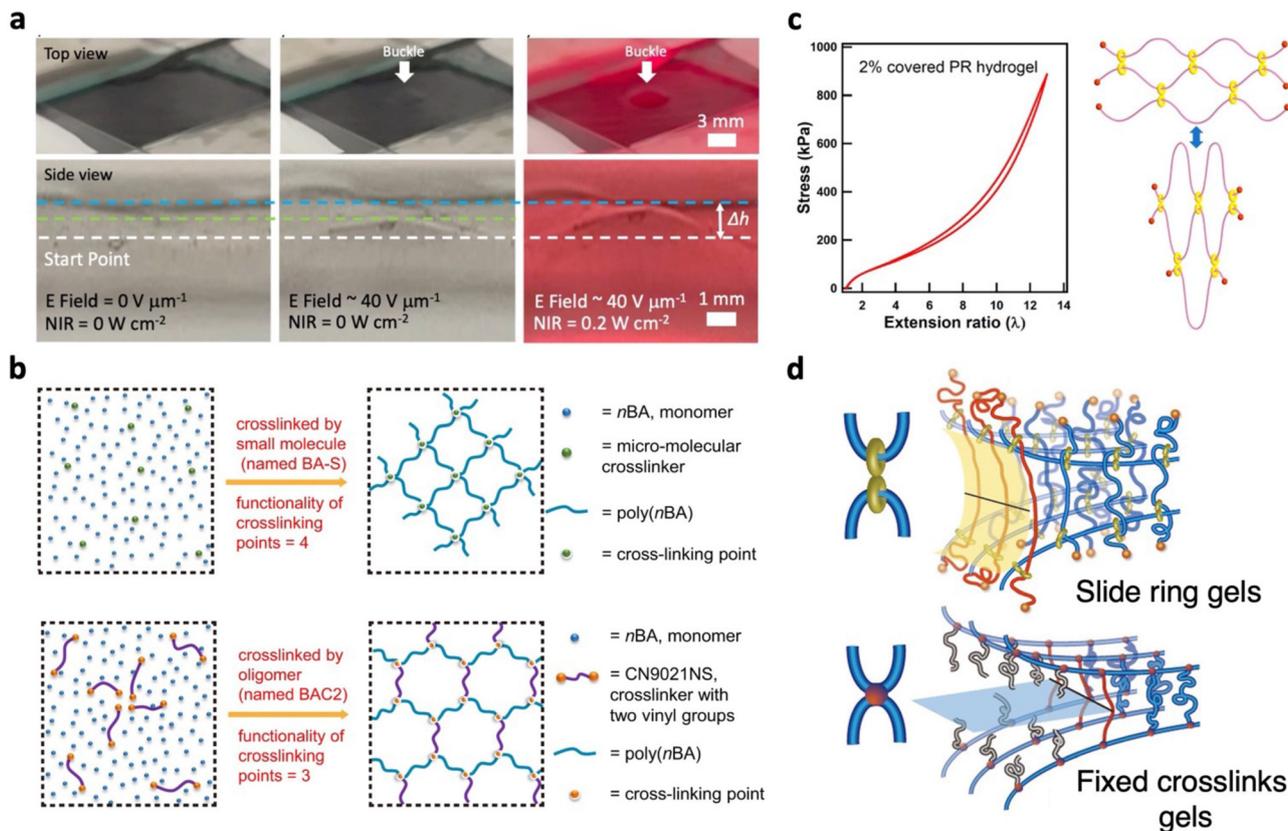
Chem. Soc. Rev., 2024, **53**, 3485–3535 | **3515**

Fig. 14 Soft actuators and polymers resistant to mechanical damage. (a) Photographs demonstrating the enhanced actuation performance of liquid metal nanocomposite DEAs achieved through the co-stimulation of an electric field and near-infrared light. Adapted from ref. 86 and published by Springer Nature under Creative Commons CC BY License. (b) Schematic representation of polymer networks composed of crosslinkers with varying molecular weights. The formation of a uniform polymer network is attributed to the molecular weight of CN9021NS macro-molecular crosslinkers. Adapted from ref. 326 and published by Springer Nature under Creative Commons CC BY License. (c) Low hysteresis observed after loading and unloading of polyrotaxane (PR) with low cyclodextrin coverage. Crosslinks are shown to slide freely upon strain, without energy dissipation. Adapted with permission from ref. 328. Copyright 2018, American Chemical Society. (d) Schematic illustrating the molecular behavior at the crack tip of gels with slide rings and fixed crosslinks. The blue strands represent the polymer chains, the red strands refer to chains that are under the highest strains, and the grey strands are the broken chains. Adapted with permission from ref. 329. Copyright 2017, American Chemical Society.

achieving actuated area strains (26%) at low electric fields (12 V μm⁻¹).[80] These SRMs have also been compared against conventional silicone and acrylic based DEAs, generating higher actuation forces (293 mN at 24.9 V mm⁻¹).[336] However, it is important to note that the lower modulus of SRMs might increase susceptibility to electromechanical instability, potentially leading to dielectric breakdown. Strategies to counteract this issue will be discussed in Section 4.22. Looking ahead, future research on SRM DEAs may focus on assessing dynamic actuation performances, particularly in the context of tactile feedback at higher frequencies.

Enhancing the long-term operational durability of soft tactile actuators requires a focus on imparting fatigue resistance. Fatigue resistance is referred to as the resistance against crack propagation under cyclic loads. While energy dissipation mechanisms improve toughness, their impact on fatigue resistance is minimal.[16] This stems from the irrecoverable depletion or slow recovery times of energy dissipation mechanisms when subjected to cyclic loading. As a result, fracture toughness and fatigue threshold tend to differ by orders of magnitude. A

promising avenue to achieve fatigue resistance is to design polymer networks with intrinsically high-energy phases.[16] These high-energy phases arrest fatigue cracks, demanding more energy for fracture compared to a single layer of polymer chains. This is demonstrated with stretchable composites featuring macro-fibers,[337–339] exhibiting favourable fracture toughness and fatigue thresholds. Guided by four principles, their design mitigates fatigue failures from fiber breakage, kink cracks, and matrix failure (Fig. 15a).[339] First, the soft matrix and hard fibers have significant modulus contrast to prevent cracks from causing severe stress concentrations in the fibers. Second, robust adhesion between the two components is crucial to prevent crack propagation through the matrix, while fibers are intact. This would also reduce hysteresis contributions from debonding and sliding between components. Third, the matrix should be resistant to large shear deformations. Lastly, adequate feature sizes prevent significant shear deformations near the crack tip, averting kink cracks. Moreover, effective mitigation of mechanical hysteresis relies on selecting low-hysteresis components, such as PDMS.[337,339] Besides macro-

3516 | *Chem. Soc. Rev.*, 2024, **53**, 3485–3535

This journal is © The Royal Society of Chemistry 2024

fibers, alternate high-energy phases with elevated fatigue thresholds include micro/nano fillers,[340,341] crystalline domains,[342,343] and phase-separated structures.[344,345] While higher fatigue resistance may be attained, application to soft actuators requires consideration, as these approaches might elevate modulus, requiring higher actuation driving forces. However, strategic distribution of higher modulus regions can yield anisotropic mechanical behaviors that steer complex actuated deformations.[346]

Polymers exhibiting strain-induced crystallization (SIC) effects offer improved fatigue performance at moderate to high strains.[350] During elongation, polymer chains align to form crystalline structures that counteract crack growth (Fig. 15b).[347,350] Upon unloading, these crystalline structures gradually revert to amorphous states. Capitalizing on this, Okui *et al.* developed pneumatic actuators composed of natural rubber (NR) which is well known for its SIC effects.[351] Instead of completely contracting the actuator during operation, partial contraction to specific strains led to enhanced fatigue resistance. By doing so, crystalline structures are sustained during contraction due to SIC hysteresis. When compared against styrene-butadiene rubber without SIC effects, NR actuators displayed a fatigue life approximately 100 times longer under identical conditions, underscoring the efficacy of SIC materials. However, various studies have shown that the SIC effects in NR diminish with strain rate and temperature.[352,353] While NR has also shown lower fatigue thresholds than most polymer networks designed with high energy phases (50 J m^{-2}),[350] its relatively low initial modulus may be advantageous for soft actuators.[354,355] Besides NR, alternatives like isoprene rubber and polychloroprene also exhibit similar SIC effects,[350] reducing the dependence on NR due to potential resource limitations. Consequently, novel polymers continue to emerge, adapting SIC effects to combat mechanical failure.[356,357] Qi *et al.* introduced SIC effects into biobased *Eucommia ulmoides* gum (EUG) through simple epoxidation modification, imparting elasticity and a low crystallization barrier under strain.[356] Crosslinking with dynamic disulfide bonds enabled recyclability, coupled with favorable mechanical toughness (30.7 MJ m^{-3}) and strain recovery (98%). Slide ring gels have also harnessed SIC effects; polyethylene glycol (PEG) chains can rapidly form and melt crystalline phases with stretching and release.[357] This is facilitated by CD rings that act as slidable crosslinks, sliding along PEG chains during strain to align them into crystalline
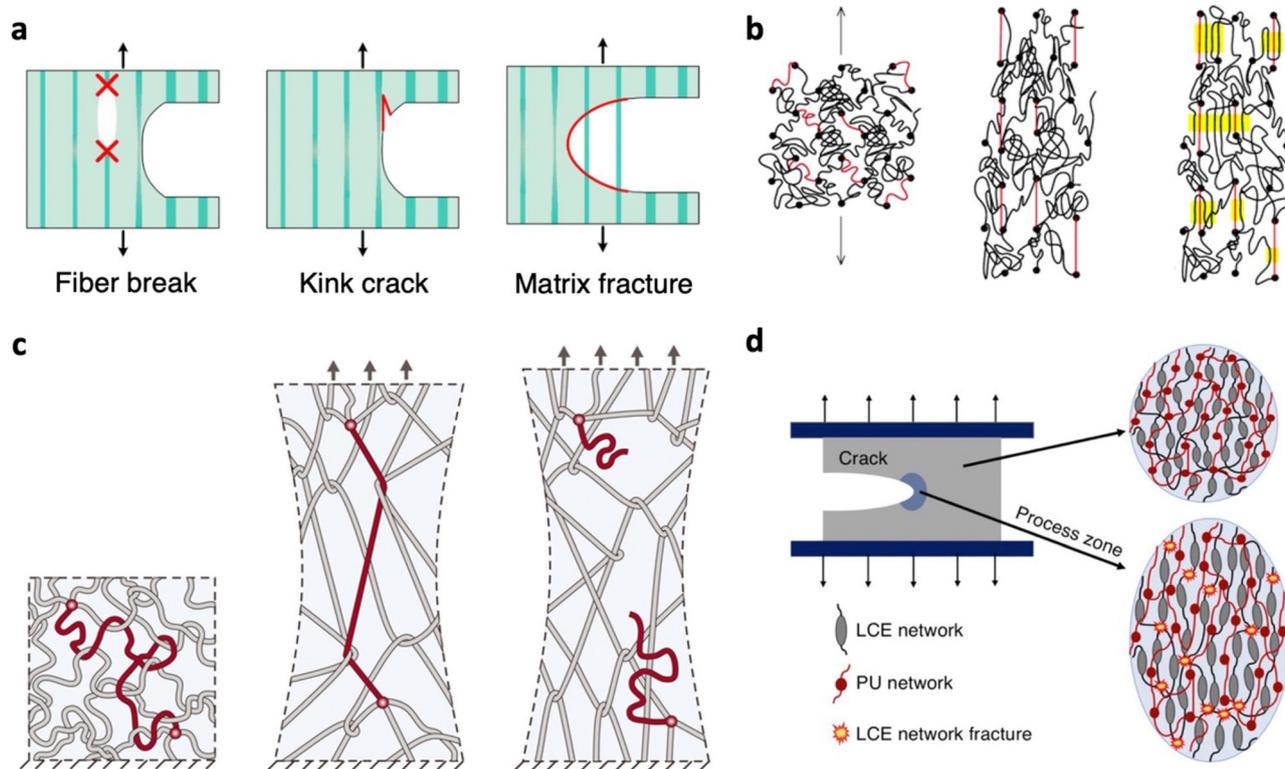

Fig. 15 Polymer network designs resistant to mechanical failure during long-term operation. (a) Failure modes of stretchable composites with macrofibers. Adapted with permission from ref. 339. Copyright 2019, Elsevier Ltd. (b) Mechanism of strain-induced crystallization, including stages before strain (left), before crystallization (middle), and strain–induced crystallization with stretched chains acting as nuclei for crystallization (right). The red strands represent short chains, the black circles symbolize crosslinks, and the yellow regions depict crystalline domains. Adapted with permission from ref. 347. Copyright 2004, American Chemical Society. (c) Polymer with a high degree of chain entanglements. The red circle represents the crosslinks. (left) Stretched polymer chain transmitting tension to other polymer chains (middle). Rupture of the stretched chain (right). Adapted with permission from ref. 348. Copyright 2021, The American Association for the Advancement of Science. (d) Toughening mechanism of a double network comprising of a liquid crystal elastomer (LCE) and polyurethane (PU). Adapted with permission from ref. 349. Copyright 2022, American Chemical Society.

This journal is © The Royal Society of Chemistry 2024

Chem. Soc. Rev., 2024, **53**, 3485–3535 | **3517**

phases. Such occurrences were realized after optimizing the CD coverage on PEG, at which low CD amounts lead to larger slidable range and extensibility. Higher concentrations of PEG further enhanced chain interactions. These slide ring gels exhibit almost no residual strains under cyclic loading and offer favorable mechanical toughness (6.6 to 22 MJ m^{-3}). Moreover, they achieve SIC effects at lower polymer concentrations compared to NR.

Recent advances have highlighted a promising avenue for achieving low hysteresis as well as enhanced fracture toughness and fatigue thresholds in polymer networks by introducing dense chain entanglements.[348,358,359] In contrast to crosslinks, these entanglements act as slip links that prevent embrittlement of the polymer (Fig. 15c). No sacrificial bonds are present as the long polymer chains do not break before material rupture, contributing to near perfect elasticity. To achieve such entanglements, polymer networks should be composed of long chains with sparse crosslinks. The high fracture toughness of these entangled polymer networks is proposed to be due to near-crack dissipation.[359] When a crack propagates, highly entangled chains are pulled out across the crack plane. The numerous interchain interactions between surrounding chains facilitate the dissipation of large amounts of energy. Scission of polymer chains extends across multiple adjacent layers surrounding the crack, resulting in the total dissipated energy surpassing that of fracturing a single polymer chain layer. Also, this distinctive feature of delocalizing tension at the crack has enabled entangled polymers to possess elevated fatigue properties. These insightful findings hold great promise for the potential application of entangled networks to soft tactile actuators.

When enhancing the durability of soft actuators, preserving their mechanical robustness under their respective actuation stimulation conditions is essential for long term operation. For instance, LCEs which respond to temperature changes exhibit diminishing fracture energies as temperature rises.[360] To address this challenge, Annapooranan et al. devised an approach involving the integration of polyurethane networks into the LCEs (Fig. 15d).[349] Despite the bulk dissipation mechanism being suppressed at higher temperatures, these double networks can maintain higher fracture toughness at elevated temperatures due to entanglements between the two networks which enlarges the process zone. Importantly, the actuation properties of these LCEs could be retained even with the additional network. The pursuit of achieving enhanced mechanical durability in soft actuators is still in its infancy, and a more comprehensive exploration of the mechanical properties of soft materials across diverse stimulation conditions remains a crucial avenue for future investigation.

4.2.2 Tolerance to electrical failure. High voltage-driven soft actuators such as piezoelectric actuators, electrostrictive actuators, DEAs and electrohydraulic actuators are prone to a common failure known as dielectric breakdown. In general, four main mechanisms for dielectric breakdown have been identified in dielectric films: electronic, thermal, electromechanical, and partial discharge.[361] Electronic breakdown occurs when electric fields cause electrons to reach unstable energy levels, leading to multiplication and increased conductivity. Thermal breakdown, on the other hand, arises when leakage current generates heat at a rate faster than it can dissipate into the surroundings. Electromechanical instability (EMI), also known as pull-in instability, occurs when electrostatic forces generate compressive stress that surpasses the material's elasticity, resulting in thinning of the dielectric layer. Moreover, defects are inherently present in polymers, leading to the concentration of local electric fields. This triggers partial discharges, gradually weakening the dielectric material. It is essential to note that in the context of soft materials, fundamental understanding of the breakdown mechanism and their interactions is still in the early stages, offering significant opportunities for further research.[66,362]

Owing to the soft nature of these actuators, EMI is a common cause of pre-mature dielectric breakdown. Early works on DEAs observed that applying pre-strains to tune the stress–strain response of elastomers led to higher breakdown strengths.[71,363] By applying pre-strains, initial strain-softening effects enable the elastomer to begin at its softest state. Thereafter, subsequent strain stiffening effects resist EMI, improving dielectric breakdown (Fig. 16a).[364,365] Despite this, these pre-strains lead to stress relaxation effects that compromise the long-term reliability of actuators. Also, pre-strains are typically applied by mounting elastomers onto rigid frames, reducing the energy density from the increased device weight. As a result, ways to develop pre-strain free DEAs have been increasingly explored.[67,366–368] One approach is through interpenetrating polymer networks (IPNs).[366,369–371] In this method, the first network is pre-strained with an external structure, followed by the addition of the second network (Fig. 16b). After the second network is polymerized, the external structures are removed. The higher rigidity of the second network allows pre-strains to be preserved within the IPN, resulting in higher dielectric breakdown. For instance, by introducing poly(trimethylolpropane trimethacrylate) as a second network to VHB network, significant actuation area strains (300%) and dielectric breakdown (420 V μm^{-1}) were realized without external structures (Fig. 16c).[369]

Another approach to achieve high dielectric breakdown without pre-strains is by tuning the chemical structures of polymers. Increasing the polymer crystallinity[372,373] or crosslinking density[367,374] has been found to induce stiffening effects that suppress EMI. However, the improvement often comes with a trade-off in actuation performances at a given driving voltage, and requires finding an optimal balance.[367,374] Thermomechanical training of triblock copolymers has proven to be an effective approach to address this trade-off.[368,375] Chen et al. demonstrated this approach on poly(styrene-b-(2-ethylhexyl acrylate)-b-styrene) with polystyrene (PS) nanodomains acting as a crosslinking point. Pre-strains were applied with the aid of an external structure, followed by stress relaxation at elevated temperatures (90 °C, 20 min) (Fig. 16d).[368] The stress relaxation temperature was selected to be close to the T_g of PS, which allowed these nanodomains to be softened. During this stage, PS nanodomains orientate from spheres to oblate

3518 | Chem. Soc. Rev., 2024, 53, 3485–3535

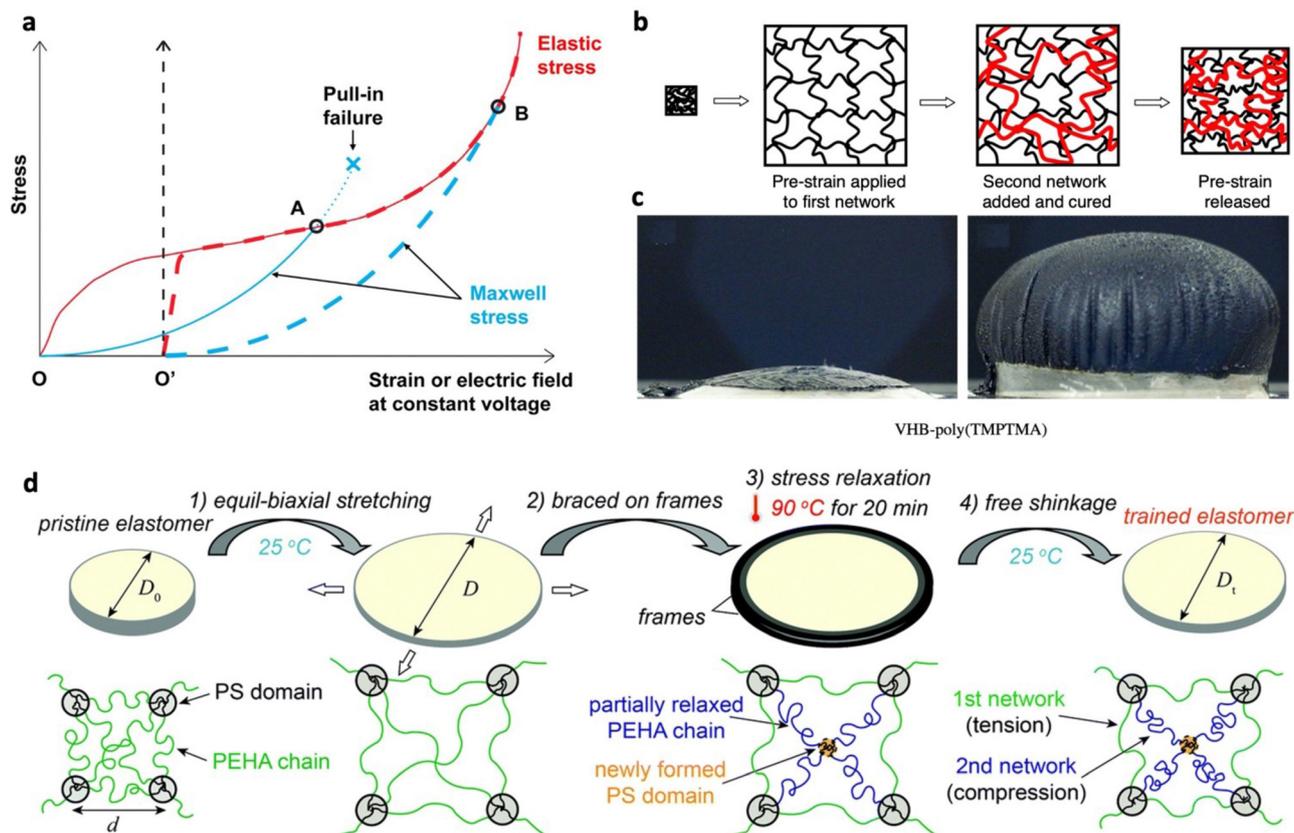This journal is © The Royal Society of Chemistry 2024

Fig. 16 Strategies to minimize electromechanical instability. (a) Stress–strain curves of dielectric elastomers under mechanical strain (red) or constant voltage (blue). The solid lines with origin O and dashed lines with origin O' represent the behavior of elastomers before pre-strain and after pre-strain, respectively. Adapted with permission from ref. 365. Copyright 2019, American Chemical Society. (b) Schematic depicting the fabrication of an interpenetrating network composed of an acrylic elastomer and trimethylolpropane trimethacrylate (TMPTMA) as the first and second networks, respectively. (c) Photograph of interpenetrating network DEA before and after actuation. (b) and (c) Are adapted with permission from ref. 369. Copyright 2007, IOP Publishing Ltd. (d) Illustration of the thermomechanical training process and the corresponding microstructure of poly(styrene-*b*-(2-ethylhexyl acrylate)-*b*-styrene) with poly(2-ethylhexyl acrylate) (PEHA) chains and polystyrene (PS) domains. Reproduced from ref. 368 with permission from the Royal Society of Chemistry.

spheroids and form some new PS nanodomains that form a second network for relaxed poly(2-ethylhexyl acrylate) strands. After cooling and releasing external structures, a freestanding trained film with semi-flexibility was obtained. Higher training strains intensified strain hardening effects but only mildly increased the elastic modulus (0.22 to 0.53 MPa). Breakdown fields were significantly enhanced from 51.0 to 158.1 V mm^{-1} due to strain hardening effects that suppressed EMI and the higher specific area of oblate spheroid PS nanodomains blocked the propagation of electrical trees/pathways. Freestanding and diaphragm DEAs based on this approach showed large actuated area strains (177%) and energy densities (18.3 J kg^{-1}), respectively.

Drawing lessons from high-voltage insulation cables, voltage stabilizers can be introduced to soft actuators to improve the breakdown field. Aromatic voltage stabilizers were incorporated through copolymerization between polydimethylsiloxane and polyphenylmethylsiloxane.[376,377] Owing to the cloud of π electrons in phenyl groups, charge trapping effects enabled higher breakdown strengths (Fig. 17a). Based on similar charge

trapping effects, octakis(phenyl)-T8-silsesquioxane (phenyl-T8) was introduced as a voltage stabilizer filler to PDMS, achieving slight improvements in breakdown strengths.[378] Despite this, the increased modulus led to lower actuation strains with increasing filler content.

Among dielectric materials, there tends to be a trade-off between dielectric constant and breakdown strength. The trade-off can be attributed to strong polarization effects in high dielectric constant materials that increases charge carrier mobility under an electric field, leading to a higher risk of breakdown.[382] Nonetheless, to enhance the capabilities of soft actuators for tactile feedback, this trade-off needs to be overcome. To increase the dielectric constant of soft actuators, ceramic and conductive fillers are often added into the polymer matrix.[70,365] However, large quantities of ceramic fillers are required to enhance dielectric constants, stiffening the polymer and reducing actuation capabilities. In contrast, conductive fillers sharply increase the dielectric constant when added near the percolation threshold. While this occurs at low quantities, the addition of conductive fillers is often accompanied with

This journal is © The Royal Society of Chemistry 2024

Chem. Soc. Rev., 2024, **53**, 3485–3535 | **3519**

charge leakages and reduced breakdown strength. To address this, combinations of ceramic and conductive fillers have been applied to soft actuators to ensure high dielectric constant and breakdown strength.[81,383,384] For instance, insulating Al_2O_3 was deposited onto conductive CNT fillers to form core–shell structures.[383] When introduced to PDMS, CNT cores largely contributed to enhancing the dielectric constant while Al_2O_3 shells suppressed leakage charges for increased breakdown strengths. Thus, diaphragm DEAs with optimal Al_2O_3-CNT fillers obtained actuated deflections that were 108% higher than pristine PDMS.

The large difference in dielectric constants between the polymer and fillers leads to electric field distortions near the interface, and concentrated electric fields at these regions are vulnerable to electrical damage. With this consideration, nano-sized fillers are preferred to minimize large local field enhancements.[382,385] The higher surface-to-volume ratio of nano-fillers forms more interfaces that can act as deep trap sites. When charges are trapped more often, they accelerate

over shorter distance and have reduced energies, prolonging the lifetime. To harness these advantages, nanoparticles must be well dispersed. This is a challenge due to their tendency to form aggregates that may bring about pores at the interface, leading to partial discharge breakdown. Thus, significant efforts have focused on surface modifications of nanoparticles to minimize interfacial energies, achieving homogeneous distributions and higher breakdown strengths. For deeper insights into the strategies to tune the polymer–nanoparticle interface, readers may refer to comprehensive reviews by Zhang et al.[385] and Luo et al.[386] The microstructure of the nanofillers, particularly the shape and orientation, plays a crucial role in improving the breakdown strength of soft actuators.[382] Large aspect ratios exhibited by nanofibers or nanosheets can increase path tortuosity of the electrical treeing/runaway process. Using a phase-field model, Shen et al. investigated the impact of microstructure on the breakdown strength of the PVDF–BaTiO₃ nanocomposite (Fig. 17b).[379] 2D simulations showed that breakdowns started from polymer–filler interfaces.
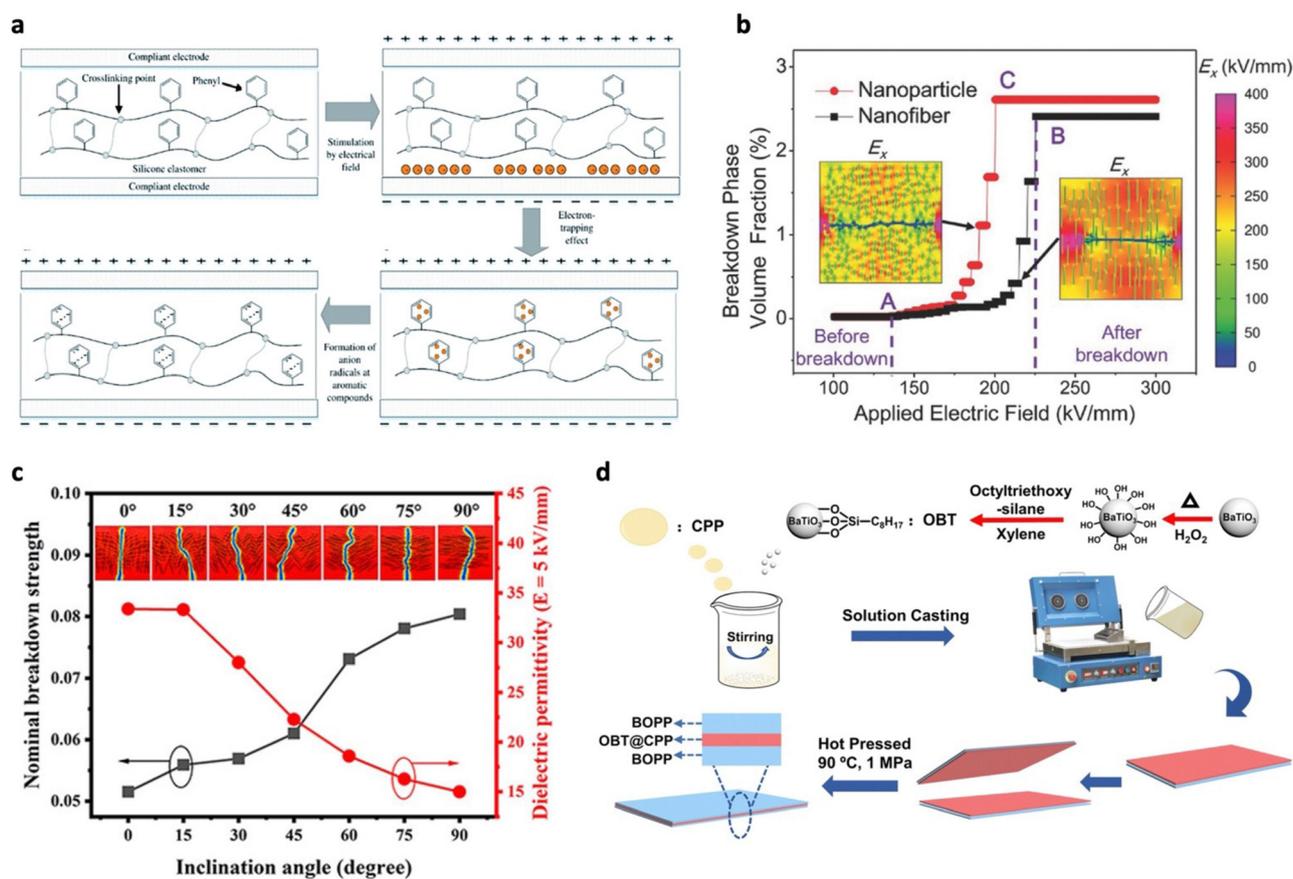

Fig. 17 Strategies to resist dielectric breakdown. (a) Illustration depicting the mechanism of aromatic voltage stabilizers that trap charges to improve dielectric breakdown strength. Adapted from ref. 376 and published by Royal Society of Chemistry under Creative Commons CC BY License. (b) Growth behavior of the breakdown phase for nanoparticles and nanofibers under an applied electric field. The insets display the electric field distribution of the nanocomposites. Adapted with permission from ref. 379. Copyright 2017, Wiley-VCH. (c) Dependence of breakdown strength and dielectric permittivity on the nanofiber inclination angle within a polymer matrix. The inset shows the breakdown path images at each inclination angle. Adapted with permission from ref. 380. Copyright 2022, American Chemical Society. (d) Schematic illustrating the fabrication of multilayer dielectric films composed of an intermediate layer with barium titanate modified with octyltriethoxysilane (OBT) and chlorinated polypropylene (CPP), sandwiched between biaxially oriented polypropylene films. Reproduced from ref. 381 with permission from the Royal Society of Chemistry.

3520 | *Chem. Soc. Rev.*, 2024, **53**, 3485–3535

This journal is © The Royal Society of Chemistry 2024

For nanoparticles, when the breakdown path grows and reaches the nanoparticle, it gets around it through the interface, leading to a twisted path. In contrast, when the breakdown path encounters the nanofiber, it tends to penetrate through. As the penetration occurs only when the electric field is high enough, larger breakdown fields are predicted for nanofiber composites. However, the enhancement depends on the orientation of the nanostructure as well. For vertically distributed nanofibers, parallel to the electric field, the electric field becomes condensed and promotes dielectric breakdown. On the other hand, parallel nanosheets dispersed the electric field, preventing the growth of the breakdown path. Separate simulations based on Landau theory indicated an opposite trend for the dielectric constant of the nanocomposites (Fig. 17c).[380] This is attributed to the reduced polarization along the electric field direction of the nanofibers. These findings provide a guide for the development of nanocomposites for high performing soft actuators.

Alternatively, both high dielectric constant and breakdown strengths can be achieved through stacking or laminating to form multilayer structures.[381,387,388] Typically, these structures are composed of alternating layers of a high dielectric constant polymer and a polymer with low leakage currents and high breakdown strengths. These multilayer structures often display improved breakdown strength due to deep traps found at the interface that limit the motion of charge carriers. Assuming that layers are linear dielectrics and have the same thickness, the local electric field across the layer is inversely proportional to the dielectric constant. This implies that the layers with high dielectric constants and lower dielectric breakdowns would experience a lower local electric field, prolonging the lifetime. Furthermore, the multilayer structure enhances the dielectric constant due to interfacial polarization contributions. For this strategy to be effective, layers must have strong interfacial adhesion as dielectric breakdown can be initiated at cavities and layer delamination.[387] Based on this approach, a dielectric layer composed of BTO modified with octyltriethoxysilane and chlorinated polypropylene (CPP) as a binder was sandwiched by BOPP (Fig. 17d).[381] Owing to CPP, strong interlayer adhesion was ensured with no observable defects. By doing so, the multilayers gave dielectric constants of 2.95 at 1 kHz, an improvement from 2.07 exhibited by commercial BOPP. The breakdown strength of multilayer films regardless of octyltriethoxysilane content showed higher or comparable breakdown strengths than BOPP, highlighting the benefits of these multilayer structures. With dielectric films such as BOPP being commonly applied for electrohydraulic actuators,[98,99,389] this strategy shows promise to lower their driving voltage while avoiding pre-mature breakdowns. Instead of a high dielectric constant layer, conductive layers have been applied to form these multilayer structures.[109,262,390] Silver nanowires were sandwiched between poly(vinylidene fluoride–trifluoroethylene–chlorotrifluoroethylene) (P(VDF–TrFE–CTFE)) films and adapted as an electrostrictive actuator.[109] While charge accumulation at the interface led to enhanced dielectric constants by 90% at 1 kHz, local intensification of the electric fields

reduced the breakdown strength by 39.1%. Compared to distributed conductive fillers, the multilayer structure lengthened the distance between conductive components, needing a higher electric field to form conductive pathways. As such, unimorph electrostrictive actuators produced force outputs of 1.92 mN at 250 V, 109% higher than the pristine P(VDF–TrFE–CTFE) actuator.

By adopting these approaches to resist electrical failure, users are provided with assurance of higher safety and long operation lifetime, encouraging the adoption of these devices. When coupled with self-healing materials discussed in the previous section, the lifetime of these devices can significantly be prolonged. Lastly, when testing at high voltages, it is crucial to have suitable safety precautions in place. This includes limiting the current output of the high voltage power supply to lower than 20 mA, leading to minimal harm of ventricular fibrillation occurring if exposed. To ensure the safe discharge of electrical current, device configurations should be designed to remain below the critical capacitance, which is calculated from the lowest possible resistance load.[391] For additional protection, electrical components such as connectors and wires that have a safe operational rating exceeding the tested voltage level may be employed.[55]

4.3 Self-cleaning actuators

In the context of generating tactile feedback, it is crucial to consider that these actuators might encounter moist skin from sweat, potentially compromising the device performance and longevity. Additionally, the presence of dust particles, falling within the micro-scale range,[392,393] similar to vibrotactile displacements, introduces the risk of negatively impacting the sensations produced if accumulated on the device surface.[11] To overcome this issue, incorporating moisture resistance and self-cleaning functionalities into soft tactile actuators becomes essential. This section highlights potential strategies encompassing both passive and active self-cleaning methods.

Passive self-cleaning relies on surfaces that are chemically or physically modified, tuning their surface energy and interaction with water droplets. Utilizing hydrophobic surfaces can provide moisture resistance and improve the self-cleaning process. Under gravity, water droplets slide or roll across surfaces, causing dust particles to adhere to the water–air interface.[394] Consequently, water droplets carry away these particles, achieving self-cleaning of the surface. These hydrophobic surfaces can be derived from low surface energy polymers such as silicones and fluropolymers,[395] commonly utilized for soft actuators. When applying these hydrophobic and self-cleaning surfaces, it is imperative that the overall actuation performance is not compromised, such as increased stiffness. With the goal of providing tactile feedback, Bubak *et al.* encapsulated ECAs with 2 mm thick Parylene coatings, showing no deterioration to blocking forces (from 50 mHz to 1 Hz) and actuation displacements (from 1 to 5 Hz).[135] Moreover, coated ECAs showed no damage even after being rinsed by water or 2-propanol. Enhanced self-cleaning effects are realized by

This journal is © The Royal Society of Chemistry 2024

Chem. Soc. Rev., 2024, **53**, 3485–3535 | **3521**

incorporating micro/nanoscale structures into low surface energy polymers, leading to rougher surfaces and superhydrophobicity (Fig. 18a). To enable spontaneous directionality of droplet motions, superhydrophobic surfaces have been imparted with wettability gradients through regulating surface chemistry and patterning surface structures.[396,397] However, droplet transport tends to be limited to short distances due to reduced driving forces and greater resistive forces with increasing liquid–solid contact area.[397]

While superhydrophobic surfaces hold promise in realizing self-cleaning in soft tactile actuators, surface heterogeneities may be prone to defects from mechanical damage or fabrication imperfections. In addition, trapped air pockets within micro/nano structures are unable to withstand pressure, causing water to penetrate these pockets.[401] This concern becomes particularly significant when wet surfaces make contact to generate tactile feedback. To address these concerns, the slippery liquid infused porous surface (SLIPS) has emerged as an alternative mechanism to repel liquids.[402,403] In general,

SLIPSs are comprised of micro/nano structured surfaces that lock in lubricants (Fig. 18b). To achieve high liquid repellence as well as low contact angle hysteresis and sliding angles, these lubricants are selected based on their immiscibility and non-reactivity with impacting liquids.[403] Compared to superhydrophobic surfaces, smoother and defect-free surfaces can be formed at the molecular scale. Furthermore, SLIPSs display intrinsic self-healing effects, wherein liquid lubricants can immediately refill damaged regions. However, factors such as evaporation and shearing may lead to the depletion of liquid lubricants, shortening the lifespan of SLIPSs.[403] To address this, efforts have focused on the development of surfaces featuring switchable states—alternating between lubricated and non-lubricated. These include utilizing phase-change lubricants,[404,405] or stimuli-responsive materials that facilitate controlled release and absorption of lubricants.[406,407] It should be highlighted that having a non-lubricated state is crucial for application to tactile actuators to avoid surfaces in contact with the SLIPS from being contaminated.
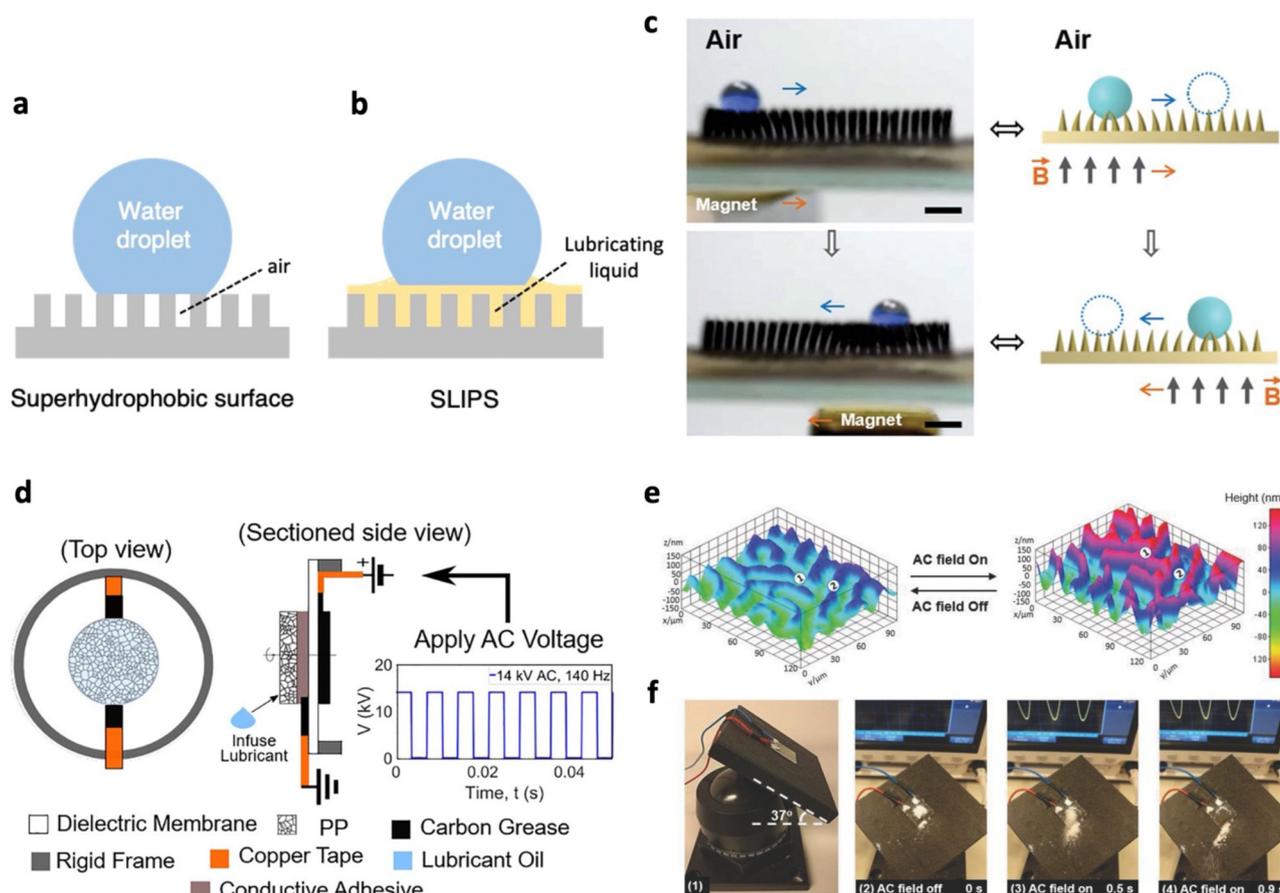

Fig. 18 Self-cleaning soft actuators. (a) Cassie–Baxter superhydrophobic surfaces with heterogeneous structures. (b) Slippery liquid infused porous surface (SLIPS), where water droplets interact with lubricating liquids locked within heterogeneous structures. (c) Manipulation of water droplets on the surface of a superhydrophobic magnetic microcilia array using a magnet. Adapted from ref. 398 and published by Wiley-VCH under Creative Commons CC BY License. (d) DEA with a SLIPS layer to combine the effects of surface vibrations and hydrophobic surfaces for water droplet removal. Adapted with permission from ref. 399. Copyright 2020, American Chemical Society. (e) Surface topographies of liquid crystal network coatings before and after actuation. (f) Photograph demonstrating self-cleaning of dry sand during actuation. (e) and (f) Are adapted from ref. 400 and published by Wiley-VCH under Creative Commons CC BY License.

3522 | *Chem. Soc. Rev.*, 2024, **53**, 3485–3535

This journal is © The Royal Society of Chemistry 2024

Active self-cleaning systems are specifically designed to exert controlled forces on particles and water droplets, ensuring efficient and targeted removal. To enhance self-cleaning efficiency, a combination of both active and passive self-cleaning approaches is often employed. Taking inspiration from nature, various studies have explored the development of artificial cilia to achieve active self-cleaning.[408,409] These synthetic cilia typically manifest as arrays of micro/nanoscale soft actuators, activated through diverse mechanisms such as magnetic fields,[398,410] light,[411] electric fields,[412] and pneumatic forces.[413] These artificial cilia are actuated to generate hydrodynamic and mechanical forces on water droplets or particles, overcoming the adhesion force with either the substrate or the cilia themselves, effectively achieving self-cleaning effects. For example, an array of superhydrophobic magnetic cilia converted from an upright to concave structure by toggling magnetic fields between off and on states (Fig. 18c).[398] Based on this structural alteration, the lateral motion of a magnet induced a resultant force on water droplets, compelling them to follow the desired trajectory. Another work showed that with a rotating magnet, artificial cilia were actuated in a tilted conical motion, capable of removing microparticles and even sand grains.[414]

Alternatively, active self-cleaning can be achieved by applying surface vibrations. Sun et al. performed in depth analysis of the vibration detachment mechanism of droplets on a superhydrophobic surface.[415] During vibration, energy is transferred from the substrate to the droplet at which detachment occurs when the droplet energy (sum of the surface energy and kinetic energy) exceeds the surface adhesion energy. Only a small vibrational amplitude is required for detachment at the resonance frequency. This is attributed to the high energy maintenance efficiency at resonance, with the droplet accumulating energy from the vibrating substrate. To vibrate at high frequencies, soft actuators driven by an electric field are commonly employed.[399,400,416] For instance, a nanoporous and flexible polypropylene SLIPS was attached onto a DEA to improve the removal of condensed water droplets (Fig. 18d).[399] By actuating the DEA at resonance frequencies, additional depinning forces on the droplet reduced departing droplet's radius (38.8%) and increased departing droplet's speed (8.6 times), achieving better removal of condensates than static SLIPS. Another approach involves generating surface vibrations with a liquid crystal network (LCN) coating to effectively eliminate debris and dust (Fig. 18e and f).[400] These vibrations are initiated by the reduction in the order parameter of closely packed mesogens when the LCN is subjected to an alternating electric field. Moreover, self-cleaning is achieved under dry conditions, without the typical reliance on water. Given that most active self-cleaning approaches utilize the same types of soft actuators that are employed to generate tactile feedback, their integration is highly feasible. This potential integration holds the promise of ensuring dependable operation of soft tactile actuators, even when they encounter sweaty hands or are exposed to dusty conditions. This alignment of self-cleaning and tactile functionality not only

enhances the versatility of these actuators but also contributes to their overall reliability and usability.

4.4 Temperature-stable actuators

Soft tactile actuators find applications in diverse environments, with some being exposed to extreme temperatures or large temperature variations. For instance, soft tactile actuators such as electrohydraulic actuators can be placed on the steering wheel to provide a haptic interface for drivers.[417,418] The temperature in the passenger compartment of cars could increase to 76 °C in summer and go down to below zero degree in winter, which challenges soft tactile actuators.[419] Temperature fluctuations could lead to changes in mechanical and electrical properties, compromising actuation performance and reliability. Significant amount of work has focused on imparting temperature stability to ionic conductors used within soft tactile actuators. This is due to their high water content, which at high or low temperatures leads to evaporation and freezing.

The anti-freezing properties of materials can be realized by two strategies: one is by inhibiting the nucleation of ice using colligative cryoprotectants, and the other is by preventing the ice growth by constructing a hybrid hydrophobic/hydrophilic heterostructure to restrict the growth of ice crystals and prevent their expansion.[420] The cryoprotectants used in the first method include organic agents (e.g., ethylene glycol, DMSO), acids (e.g., sulfuric acid, phosphoric acid), zwitterions (e.g., proline, betaine), ionic liquids (e.g., 1-methyl-3-pentylimidazolium tetrafluoroborate, 1-ethyl-3-methylimidazolium dicyanamide), and inorganic salts (e.g., iron(III) sulfate, iron(III) chloride), which can create rich and strong hydrogen bonding or electrostatic interactions to prevent the formation of ordered networks during the freezing process. For instance, the organohydrogel based on water–DMSO solvent can maintain its mechanical properties at −70 °C.[421] A hydraulic actuator based on PVA/DMSO gel could lift a 100 g weight at −45 °C to the same level at 20 °C (Fig. 19a), owing to the good mechanical properties and low freezing point which are the result of salting-out and co-nonsolvency effects, respectively.[422] However, it is noted that these cryoprotectants may lead to low electrical conductivity, reduced flexibility and elasticity, or potential toxicity, etc. In the second strategy, the heterostructures are demonstrated by core–shell nanostructures,[423] hydrophilic elastomers with hydrophobic coatings,[424] and interpenetrating polymer networks.[425]

Some organohydrogels constructed with binary water–organic solvent can obtain not only freezing tolerance but also heat tolerance, which makes these gels useful for actuators working at subzero and elevated temperatures. Gao et al. reported an ionic organohydrogel using a water–glycerol mixture with good conductivity from −20 to 80 °C, which could work as an electrode for DEA grippers and maintain capturing capability at both high (80 °C) and low (−10 °C) temperatures (Fig. 19b).[426] Also, this binary solvent used for the P(SPMA-r-MMA) gel could tolerate 100 °C. This was demonstrated as the gel was utilized as electrodes for DEAs, at which the resultant DEA maintained over 60% of its original area strain, after being
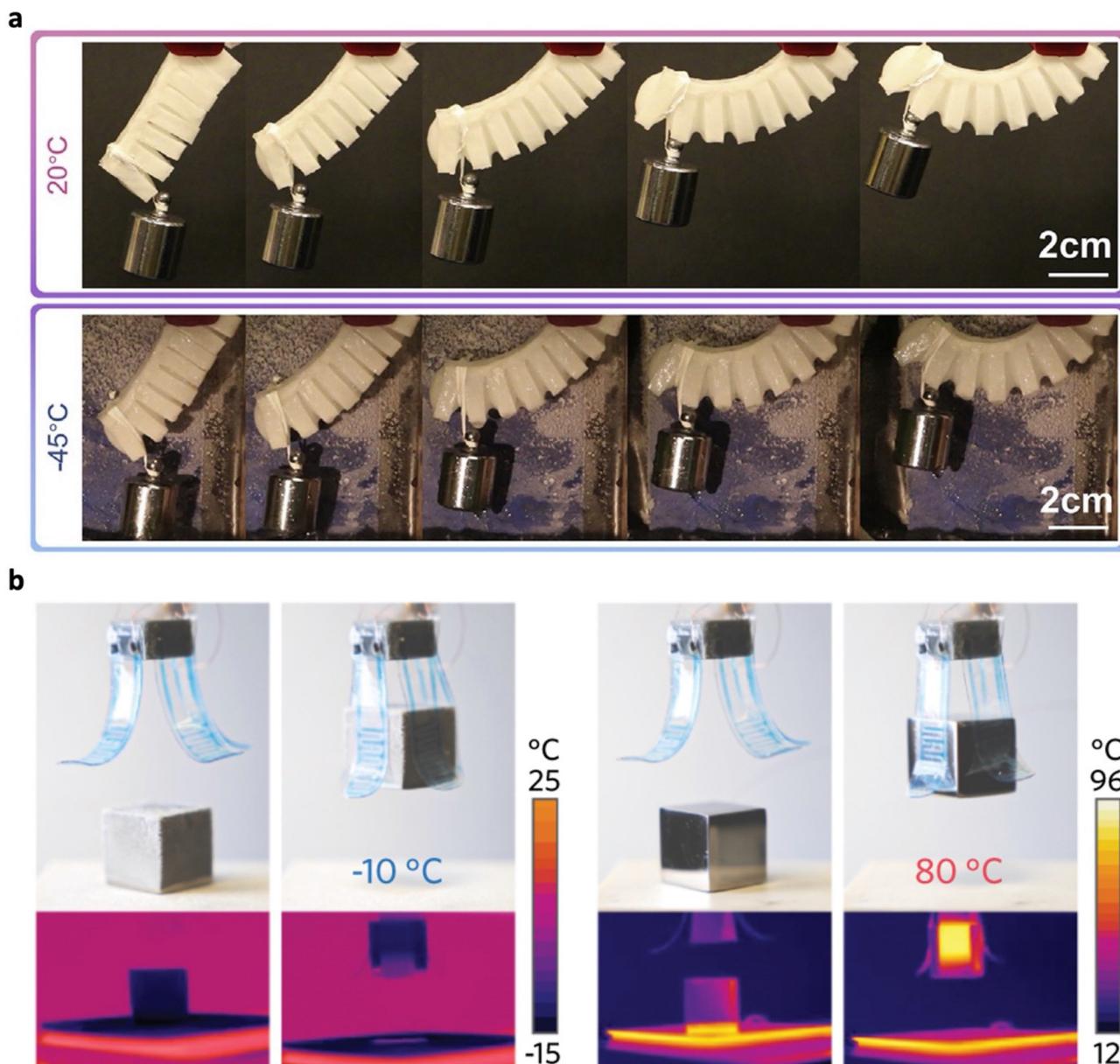
Fig. 19 Temperature-stable actuators. (a) Demonstration of a soft hydraulic actuator composed of anti-freezing polyvinyl alcohol gels, lifting a 100 g weight at both 20 °C and −45 °C. Adapted from ref. 422 and published by Elsevier under Creative Commons CC BY License. (b) Illustration of a dielectric elastomer gripper with ionic organohydrogel electrodes, showcasing its ability to maintain a grip on hot (80 °C) and cold (−10 °C) objects. Adapted from ref. 426 and published by Springer Nature under Creative Commons CC BY License.

subjected to 100 °C for 420 min.[427] Lou *et al.* introduced a solvent system of ethylene glycol solution of LiCl (EG/LiCl) to a hydrogel, which demonstrated good stretchability ($\sim$200%) and conductivity (0.07–7.7 S m^{-1}) from −20 to 120 °C.[428] These works provide foundations for not only soft actuators based on deformation of gels, but also other kinds of soft actuators with gel electrodes.

5. Conclusions and outlook

In this review, we highlight the progress, key challenges and requirements of various types of soft tactile actuators to achieve high actuation capabilities that will enhance the user's tactile experiences. Based on their driving stimuli, these tactile actuators come with their advantages and disadvantages, as summarized in Table 4. As the field advances, new materials and actuation technologies may be explored to realize tactile feedback. Hydrogel actuators have recently utilized electro-osmotic effects and turgor pressure to realize fast and high tactile force.[429] Despite the need for liquid containment, similar configurations as thermo-responsive hydrogels may be adopted to provide tactile feedback. Soft actuators responsive to solvent vapors or humidity have been applied as grippers and soft robots,[430–432] but have yet to be demonstrated for tactile

3524 | *Chem. Soc. Rev.*, 2024, **53**, 3485–3535

This journal is © The Royal Society of Chemistry 2024

Table 4 Comparison of various types of soft tactile actuators

Soft tactile actuators	Advantages	Disadvantages
Dielectric elastomer actuators (DEAs)	Wide frequency operation, rapid response, high actuation strains, high force output for stacked DEAs, low power consumption	High driving voltage (10^2–10^3 V), limited force output from single layer, tethered, soft elastomers susceptible to puncture
Electrohydraulic actuators	Wide frequency operation, rapid response, high actuation displacements and output force, high energy density, low power consumption	High driving voltage (10^3 V), tethered, soft shells susceptible to puncture
Piezoelectric and electrostrictive actuators	Wide frequency operation, rapid response, moderate driving voltage (10^1–10^2 V), high force output when stacked	Low actuation displacement, tethered, limited force output from single layer
Electrochemical actuators	Low driving voltage (<10 V), large bending actuation, low power consumption	Limited frequency operation, low force outputs, short device lifetime in air due to water evaporation
Pneumatic actuators	High actuation force and displacements, easy implementation	Bulky pump often required, susceptibility to puncture
Shape memory polymers (SMPs)	Programmable shapes	Slow response, re-programming is needed for one-way SMPs
Liquid crystal elastomers	Reversible actuation, high actuation strains, anisotropic behaviors	Slow response, low energy conversion efficiency, require additional alignment processing
Thermo-responsive hydrogels	Simple control, reversible actuation	Slow response, poor mechanical properties, susceptibility to external damage, require liquid containment
Liquid–vapor phase transition	Simple control, reversible actuation	Poor cyclic stability, require sealings with low gas permeability
Electromagnetic actuators	Wide frequency operation, rapid response, untethered, large actuation displacement and force, low to moderate power consumption	Heat generation from applied current, rigid magnets limit deformations
Magnetorheological actuators	Tuneable surface stiffness, rapid response, untethered, large actuation forces	High power consumption, bulky configurations

feedback. While these actuators exhibit slow responses, their gradual actuation can potentially provide tactile cues from the environment. Also, given the close contact of our clothes with the skin, soft actuators in the form of fibers can be further explored. Upon the addition of stimuli, these fibers contract or expand, potentially imparting tactile feedback when integrated with commercial cloth.[432,433]

To ensure that these tactile actuators can withstand real world conditions, it is critical to ensure sufficient durability to withstand and recover from damage caused by external factors. Thus, the strategies and innovations to impart durability to soft actuators are further examined in this review. However, the concurrent combination of performance and durability is particularly challenging, giving rise to various trade-offs. For instance, while adding high energy phases to soft actuators can improve fracture toughness and fatigue thresholds, this tends to increase the elastic modulus that may require higher actuation driving forces. Careful optimization of material parameters is needed to achieve the ideal combination of performance and durability. Machine learning methods can be incorporated to reduce tedious trial-and-error methods for achieving this goal. Their current application for predicting the properties and performances of soft materials and robotics[434–436] highlights the feasibility of these methods to realize soft durable tactile actuators.

Although this review focuses on soft actuators to achieve tactile feedback, tactile devices for the real world require actuators to be portable and autonomous. This is achieved through the integration of sensors, controllers, and power sources.[50,437] Material approaches discussed in this review to impart durability to soft actuators may be extended to other soft components. In addition, self-sensing capabilities displayed in soft actuators[100,306,438] can be utilized to trigger self-healing and self-cleaning effects for durability, reducing the payload from multiple integrated devices.

Increasing the operational lifespan of soft tactile actuators prolongs the generation of waste, one of the key principles of circular design.[14,439] However, this is incomplete without proper end-of-life management that closes the loop. Thus, increasing attention has been focused on imparting biodegradability and recyclability to soft materials and actuators.[440,441] Moreover, a large portion of polymers are derived from fossil fuels, contributing to CO_2 emissions. This has resulted in a growing trend of utilizing natural polymers to design soft actuators.[442] Moving forward, these approaches may complement durable soft tactile actuators bringing us closer to a sustainable future.

In conclusion, the pursuit of durability in soft tactile actuators is paramount for their practical adoption and long-term functionality. As detailed in this review, achieving this goal necessitates a multifaceted approach that includes advances in material development, design optimization, and tailored fabrication processes. Ultimately, by implementing these advancements, users can benefit from extended operational lifespan, heightened reliability, and enhanced overall performance, paving the way for broader and impactful applications in various fields.

Author contributions

Conceptualization: M. W. M. T. and P. S. L.; writing – original draft: M. W. M. T., H. W., D. G. and P. G.; writing – review &

This journal is © The Royal Society of Chemistry 2024

Chem. Soc. Rev., 2024, **53**, 3485–3535 | **3525**

Conflicts of interest

There are no conflicts to declare.

Acknowledgements

References

1 S. Ipakchian Askari, G. Huisman, A. Haans and W. A. IJsselsteijn, *Front. Comput. Sci.*, 2022, **4**, 795927.

2 J. Yin, R. Hinchet, H. Shea and C. Majidi, *Adv. Funct. Mater.*, 2021, **31**, 2007428.

3 S. Biswas and Y. Visell, *Adv. Funct. Mater.*, 2021, **31**, 2008186.

4 D. Rus and M. T. Tolley, *Nature*, 2015, **521**, 467–475.

5 F. Sorgini, R. Caliò, M. C. Carrozza and C. M. Oddo, *Disability Rehabilitation: Assistive Technology*, 2018, **13**, 394–421.

6 P. B. Shull and D. D. Damian, *J. NeuroEngineering Rehabil*, 2015, **12**, 59.

7 H. Bai, S. Li and R. F. Shepherd, *Adv. Funct. Mater.*, 2021, **31**, 2009364.

8 C. Pacchierotti, S. Scheggi, D. Prattichizzo and S. Misra, *Front. Robotics AI*, 2016, **3**, 53.

9 M. Li, A. Pal, A. Aghakhani, A. Pena-Francesch and M. Sitti, *Nat. Rev. Mater.*, 2022, **7**, 235–249.

10 S. Terryn, J. Langenbach, E. Roels, J. Brancart, C. Bakkali-Hassani, Q.-A. Poutrel, A. Georgopoulou, T. George Thuruthel, A. Safaei, P. Ferrentino, T. Sebastian, S. Norvez, F. Iida, A. W. Bosman, F. Tournilhac, F. Clemens, G. Van Assche and B. Vanderborght, *Mater. Today*, 2021, **47**, 187–205.

11 T.-H. Yang, J. R. Kim, H. Jin, H. Gil, J.-H. Koo and H. J. Kim, *Adv. Funct. Mater.*, 2021, **31**, 2008831.

12 A. Aabloo, J. Belikov, V. Kaparin and Ü. Kotta, *IEEE Access*, 2020, **8**, 121059–121073.

13 F. B. Albuquerque and H. Shea, *Smart Mater. Struct.*, 2021, **30**, 125022.

14 B. Suárez-Eiroa, E. Fernández, G. Méndez-Martínez and D. Soto-Oñate, *J. Cleaner Prod.*, 2019, **214**, 952–961.

15 N. El-Atab, R. B. Mishra, F. Al-Modaf, L. Joharji, A. A. Alsharif, H. Alamoudi, M. Diaz, N. Qaiser and M. M. Hussain, *Adv. Intell. Syst.*, 2020, **2**, 2000128.

16 X. Zhao, X. Chen, H. Yuk, S. Lin, X. Liu and G. Parada, *Chem. Rev.*, 2021, **121**, 4309–4372.

17 J. Ekeocha, C. Ellingford, M. Pan, A. M. Wemyss, C. Bowen and C. Wan, *Adv. Mater.*, 2021, **33**, 2008052.

18 R. S. Dahiya, G. Metta, M. Valle and G. Sandini, *IEEE Trans. Rob.*, 2009, **26**, 1–20.

19 P. Delmas, J. Hao and L. Rodat-Despoix, *Nat. Rev. Neurosci.*, 2011, **12**, 139–153.

20 J. Scheibert, S. Leurent, A. Prevost and G. Debregeas, *Science*, 2009, **323**, 1503–1506.

21 Y. H. Jung, J.-Y. Yoo, A. Vázquez-Guardado, J.-H. Kim, J.-T. Kim, H. Luan, M. Park, J. Lim, H.-S. Shin, C.-J. Su, R. Schloen, J. Trueb, R. Avila, J.-K. Chang, D. S. Yang, Y. Park, H. Ryu, H.-J. Yoon, G. Lee, H. Jeong, J. U. Kim, A. Akhtar, J. Cornman, T. Kim, Y. Huang and J. A. Rogers, *Nat. Electron.*, 2022, **5**, 374–385.

22 X. Yu, Z. Xie, Y. Yu, J. Lee, A. Vazquez-Guardado, H. Luan, J. Ruban, X. Ning, A. Akhtar, D. Li, B. Ji, Y. Liu, R. Sun, J. Cao, Q. Huo, Y. Zhong, C. Lee, S. Kim, P. Gutruf, C. Zhang, Y. Xue, Q. Guo, A. Chempakasseril, P. Tian, W. Lu, J. Jeong, Y. Yu, J. Cornman, C. Tan, B. Kim, K. Lee, X. Feng, Y. Huang and J. A. Rogers, *Nature*, 2019, **575**, 473–479.

23 K. O. Johnson, *Curr. Opin. Neurobiol.*, 2001, **11**, 455–461.

24 E. R. Kandel, J. H. Schwartz, T. M. Jessell, S. Siegelbaum, A. J. Hudspeth and S. Mack, *Principles of neural science*, McGraw-hill, New York, 2000, vol. 4.

25 A. Zimmerman, L. Bai and D. D. Ginty, *Science*, 2014, **346**, 950–954.

26 J. Dargahi and S. Najarian, *Int. J. Med. Rob. Comput. Assisted Surgery*, 2004, **1**, 23–35.

27 K. O. Johnson, T. Yoshioka and F. Vega–Bermudez, *J. Clin. Neurophysiol.*, 2000, **17**, 539.

28 J. C. Craig and K. B. Lyle, *Perception Psychophysics*, 2001, **63**, 337–347.

29 V. B. Mountcastle, *The sensory hand: neural mechanisms of somatic sensation*, Harvard University Press, 2005.

30 in *Engineering Haptic Devices: A Beginner's Guide*, ed. C. Hatzfeld and T. A. Kern, Springer, London, 2014.

31 S. J. Bensmaıa and M. Hollins, *J. Acoust. Soc. Am.*, 2000, **108**, 1236–1245.

32 I. Birznieks, S. McIntyre, H. M. Nilsson, S. S. Nagi, V. G. Macefield, D. A. Mahns and R. M. Vickery, *eLife*, 2019, **8**, e46510.

33 G. S. Harrington and J. Hunter Downs III, *Brain Res.*, 2001, **897**, 188–192.

34 K. S. Hale and K. M. Stanney, *IEEE Comput. Graph. Appl.*, 2004, **24**, 33–39.

35 D. Deflorio, M. Di Luca and A. M. Wing, *Front. Hum. Neurosci.*, 2022, **16**, 862344.

36 Y. H. Jung, J.-H. Kim and J. A. Rogers, *Adv. Funct. Mater.*, 2021, **31**, 2008805.

37 Y. Roudaut, A. Lonigro, B. Coste, J. Hao, P. Delmas and M. Crest, *Channels*, 2012, **6**, 234–245.

38 L. Djouhri, *Neurosci. Biobehav. Rev.*, 2016, **61**, 225–238.

39 S. G. Lechner and G. R. Lewin, *Physiology*, 2013, **28**, 142–150.

3526 | *Chem. Soc. Rev.*, 2024, **53**, 3485–3535

This journal is © The Royal Society of Chemistry 2024

40 V. E. Abraira and D. D. Ginty, *Neuron*, 2013, **79**, 618–639.

41 A. Wilska, *Acta Physiol. Scand.*, 1954, **31**, 285–289.

42 F. Mancini, A. Bauleo, J. Cole, F. Lui, C. A. Porro, P. Haggard and G. D. Iannetti, *Ann. Neurol.*, 2014, **75**, 917–924.

43 S. Allin, Y. Matsuoka and R. Klatzky, *Proceedings 10th Symposium on Haptic Interfaces for Virtual Environment and Teleoperator Systems. HAPTICS 2002*, 2002, pp. 299–302.

44 X. D. Pang, H. Z. Tan and N. I. Durlach, *Perception Psychophys.*, 1991, **49**, 531–540.

45 K. L. Woodward, *Somatosens. Res.*, 1993, **10**, 63–67.

46 A. Abdouni, G. Moreau, R. Vargiolu and H. Zahouani, *Sci. Rep.*, 2018, **8**, 14240.

47 S. Chen, M. W. M. Tan, X. Gong and P. S. Lee, *Adv. Intell. Syst.*, 2021, **4**, 2100075.

48 Ankit, T. Y. K. Ho, A. Nirmal, M. R. Kulkarni, D. Accoto and N. Mathews, *Adv. Intell. Syst.*, 2022, **4**, 2100061.

49 I. Koo, K. Jung, J. Koo, J. Nam, Y. Lee and H. R. Choi, *Proceedings 2006 IEEE International Conference on Robotics and Automation, 2006. ICRA 2006*, 2006, pp. 2220–2225.

50 X. Ji, X. Liu, V. Cacucciolo, Y. Civet, A. El Haitami, S. Cantin, Y. Perriard and H. Shea, *Adv. Funct. Mater.*, 2021, **31**, 2006639.

51 J.-H. Youn, H. Mun and K.-U. Kyung, *IEEE Access*, 2021, **9**, 30206–30215.

52 H. Phung, C. T. Nguyen, T. D. Nguyen, C. Lee, U. Kim, D. Lee, J. Nam, H. Moon, J. C. Koo and H. R. Choi, *Meccanica*, 2015, **50**, 2825–2837.

53 J. Son, S. Lee, G. Y. Bae, G. Lee, M. Duduta and K. Cho, *Adv. Funct. Mater.*, 2023, 2213589.

54 H. Boys, G. Frediani, M. Ghilardi, S. Poslad, J. C. Busfield and F. Carpi, *2018 IEEE International Conference on Soft Robotics (RoboSoft)*, 2018, pp. 270–275.

55 H. Zhao, A. M. Hussain, A. Israr, D. M. Vogt, M. Duduta, D. R. Clarke and R. J. Wood, *Soft Robot.*, 2020, **7**, 451–461.

56 E. Leroy, R. Hinchet and H. Shea, *Adv. Mater.*, 2020, **32**, 2002564.

57 E. Leroy and H. Shea, *Adv. Mater. Technol.*, 2023, **8**, 2300242.

58 G. Grasso, S. Rosset and H. Shea, *Adv. Funct. Mater.*, 2023, 2213821.

59 Y. Shao, S. Ma, S. H. Yoon, Y. Visell and J. Holbery, *2020 IEEE Haptics Symposium (HAPTICS)*, 2020, pp. 815–820.

60 G.-Y. Yun, J. Kim, J.-H. Kim and S.-Y. Kim, *Sens. Actuators, A*, 2010, **164**, 68–73.

61 Y. Shouji, T. Sekine, K. Ito, N. Ito, T. Yasuda, Y.-F. Wang, Y. Takeda, D. Kumaki, F. D. D. Santos, A. Miyabo and S. Tokito, *Adv. Electron. Mater.*, 2023, 2201040.

62 G. C. Schmidt, J. M. Werner, T. Weissbach, J. Strutwolf, R. Eland, W.-G. Drossel and A. C. Hübler, *Sensors*, 2022, **22**, 3796.

63 Q. Van Duong, V. P. Nguyen, A. T. Luu and S. T. Choi, *Sci. Rep.*, 2019, **9**, 13290.

64 W.-E. Ju, Y.-J. Moon, C.-H. Park and S. T. Choi, *Smart Mater. Struct.*, 2014, **23**, 074004.

65 S. G. Lu, X. Chen, T. Levard, P. J. Diglio, L. J. Gorny, C. D. Rahn and Q. M. Zhang, *Sci. Rep.*, 2015, **5**, 11361.

66 E. Hajiesmaili and D. R. Clarke, *J. Appl. Phys.*, 2021, **129**, 151102.

67 M. Vatankhah-Varnoosfaderani, W. F. M. Daniel, A. P. Zhushma, Q. Li, B. J. Morgan, K. Matyjaszewski, D. P. Armstrong, R. J. Spontak, A. V. Dobrynin and S. S. Sheiko, *Adv. Mater.*, 2017, **29**, 1604209.

68 M. Duduta, E. Hajiesmaili, H. Zhao, R. J. Wood and D. R. Clarke, *Proc. Natl. Acad. Sci. U. S. A.*, 2019, **116**, 2476–2481.

69 J. Pu, Y. Meng, Z. Xie, Z. Peng, J. Wu, Y. Shi, R. Plamthottam, W. Yang and Q. Pei, *Sci. Adv.*, 2022, **8**, eabm6200.

70 L. J. Romasanta, M. A. Lopez-Manchado and R. Verdejo, *Prog. Polym. Sci.*, 2015, **51**, 188–211.

71 R. Pelrine, R. Kornbluh, Q. Pei and J. Joseph, *Science*, 2000, **287**, 836–839.

72 R. Lundström, H. Dahlqvist, M. Hagberg and T. Nilsson, *Clin. Neurophys. Practice*, 2018, **3**, 33–39.

73 C. Zippenfennig, B. Wynands and T. L. Milani, *J. Clin. Med.*, 2021, **10**, 3083.

74 M. Morioka, D. J. Whitehouse and M. J. Griffin, *Somatosens. Res.*, 2008, **25**, 101–112.

75 S. Gratz-Kelly, G. Rizzello, M. Fontana, S. Seelecke and G. Moretti, *Adv. Funct. Mater.*, 2022, **32**, 2201889.

76 M. W. M. Tan, G. Thangavel and P. S. Lee, *NPG Asia Mater.*, 2019, **11**, 62.

77 J. Liu, Y.-L. Lu, M. Tian, F. Li, J. Shen, Y. Gao and L. Zhang, *Adv. Funct. Mater.*, 2013, **23**, 1156–1163.

78 S. Ho, H. Banerjee, Y. Y. Foo, H. Godaba, W. M. M. Aye, J. Zhu and C. H. Yap, *J. Intell. Mater. Syst. Struct.*, 2017, **28**, 3054–3065.

79 J. Huang, X. Zhang, R. Liu, Y. Ding and D. Guo, *Nat. Commun.*, 2023, **14**, 1483.

80 D. Yang, F. Ge, M. Tian, N. Ning, L. Zhang, C. Zhao, K. Ito, T. Nishi, H. Wang and Y. Luan, *J. Mater. Chem. A*, 2015, **3**, 9468–9479.

81 M. Poikelispää, A. Shakun, A. Das and J. Vuorinen, *J. Appl. Polym. Sci.*, 2016, **133**, 44116.

82 H. Sun, X. Liu, H. Yan, Z. Feng, B. Yu, N. Ning, M. Tian and L. Zhang, *Polymer*, 2019, **165**, 1–10.

83 J. von Szczepanski and D. M. Opris, *Adv. Mater. Technol.*, 2023, **8**, 2201372.

84 Y. Ni, D. Yang, Q. Wei, L. Yu, J. Ai and L. Zhang, *Compos. Sci. Technol.*, 2020, **195**, 108202.

85 F. Galantini, F. Carpi and G. Gallone, *Smart Mater. Struct.*, 2013, **22**, 104020.

86 M. W. M. Tan, H. Bark, G. Thangavel, X. Gong and P. S. Lee, *Nat. Commun.*, 2022, **13**, 6769.

87 D. M. Opris, *Adv. Mater.*, 2018, **30**, 1703678.

88 I. M. Koo, K. Jung, J. C. Koo, J.-D. Nam, Y. K. Lee and H. R. Choi, *IEEE Trans. Rob.*, 2008, **24**, 549–558.

89 Q. Pei, M. Rosenthal, S. Stanford, H. Prahlad and R. Pelrine, *Smart Mater. Struct.*, 2004, **13**, N86–N92.

90 H. Zhao, A. M. Hussain, M. Duduta, D. M. Vogt, R. J. Wood and D. R. Clarke, *Adv. Funct. Mater.*, 2018, **28**, 1804328.

This journal is © The Royal Society of Chemistry 2024

Chem. Soc. Rev., 2024, **53**, 3485–3535 | **3527**

91 M. A. Srinivasan and R. H. LaMotte, *J. Neurophysiol.*, 1995, **73**, 88–101.

92 F. Carpi, G. Frediani, S. Tarantino and D. De Rossi, *Polym. Int.*, 2010, **59**, 407–414.

93 G. Frediani, H. Boys, M. Ghilardi, S. Poslad, J. J. C. Busfield and F. Carpi, *Adv. Mater. Technol.*, 2021, **6**, 2100016.

94 P. Rothemund, N. Kellaris, S. K. Mitchell, E. Acome and C. Keplinger, *Adv. Mater.*, 2021, **33**, e2003375.

95 M. Taghavi, T. Helps and J. Rossiter, *Sci. Robot.*, 2018, **3**, eaau9795.

96 E. Acome, S. K. Mitchell, T. G. Morrissey, M. B. Emmett, C. Benjamin, M. King, M. Radakovitz and C. Keplinger, *Science*, 2018, **359**, 61–65.

97 P. Rothemund, S. Kirkman and C. Keplinger, *Proc. Natl. Acad. Sci. U. S. A.*, 2020, **117**, 16207–16213.

98 N. Kellaris, V. Gopaluni Venkata, G. M. Smith, S. K. Mitchell and C. Keplinger, *Sci. Robot.*, 2018, **3**, eaar3276.

99 X. Wang, S. K. Mitchell, E. H. Rumley, P. Rothemund and C. Keplinger, *Adv. Funct. Mater.*, 2020, **30**, 1908821.

100 Z. Yoder, D. Macari, G. Kleinwaks, I. Schmidt, E. Acome and C. Keplinger, *Adv. Funct. Mater.*, 2023, **33**, 2209080.

101 S. K. Mitchell, T. Martin and C. Keplinger, *Adv. Mater. Technol.*, 2022, **7**, 2101469.

102 S. Wang and Q. Li, *IET Nanodielectrics*, 2018, **1**, 80–91.

103 I. Chae, C. K. Jeong, Z. Ounaies and S. H. Kim, *ACS Appl. Bio Mater.*, 2018, **1**, 936–953.

104 S. H. Yoon, S. Ma, W. S. Lee, S. Thakurdesai, D. Sun, F. P. Ribeiro and J. D. Holbery, *Proceedings of the 32nd Annual ACM Symposium on User Interface Software and Technology*, ACM, New Orleans LA USA, 2019, pp. 949–961.

105 Q. Van Duong, V. P. Nguyen, F. Domingues Dos Santos and S. T. Choi, *ACS Appl. Mater. Interfaces*, 2019, **11**, 33292–33301.

106 T. Wongwirat, Z. Zhu, G. Rui, R. Li, P. Laoratanakul, H. He, H. Manuspiya and L. Zhu, *Macromolecules*, 2020, **53**, 10942–10954.

107 B. Qiao, X. Wang, S. Tan, W. Zhu and Z. Zhang, *Macromolecules*, 2019, **52**, 9000–9011.

108 Y. Liang, T. Cui and L. Liu, *Polymer*, 2021, **235**, 124279.

109 T. H. T. Fook, J. H. Jeon and P. S. Lee, *Adv. Mater. Technol.*, 2020, **5**, 1900762.

110 Z. Zhang, X. Wang, S. Tan and Q. Wang, *J. Mater. Chem. A*, 2019, **7**, 5201–5208.

111 F. Carpi, R. Kornbluh, P. Sommer-Larsen and G. Alici, *Bioinspir. Biomim.*, 2011, **6**, 045006.

112 H. Kim, F. Torres, D. Villagran, C. Stewart, Y. Lin and T.-L. B. Tseng, *Macromol. Mater. Eng.*, 2017, **302**, 1700229.

113 H. Zhang, Z. Lin, Y. Hu, S. Ma, Y. Liang, L. Ren and L. Ren, *Advanced Science*, 2023, **10**, 2206135.

114 S. Ma, Y. Zhang, Y. Liang, L. Ren, W. Tian and L. Ren, *Adv. Funct. Mater.*, 2020, **30**, 1908508.

115 J. Wang, C. Xu, M. Taya and Y. Kuga, *Smart Mater. Struct.*, 2007, **16**, S214.

116 D. Guo, Y. Han, J. Huang, E. Meng, L. Ma, H. Zhang and Y. Ding, *ACS Appl. Mater. Interfaces*, 2019, **11**, 2386–2397.

117 D. M. Correia, J. C. Barbosa, C. M. Costa, P. M. Reis, J. M. S. S. Esperança, V. de Zea Bermudez and S. Lanceros-Méndez, *J. Phys. Chem. C*, 2019, **123**, 12744–12752.

118 C. Lu, Y. Yang, J. Wang, R. Fu, X. Zhao, L. Zhao, Y. Ming, Y. Hu, H. Lin, X. Tao, Y. Li and W. Chen, *Nat. Commun.*, 2018, **9**, 752.

119 Y. Yan, T. Santaniello, L. G. Bettini, C. Minnai, A. Bellacicca, R. Porotti, I. Denti, G. Faraone, M. Merlini, C. Lenardi and P. Milani, *Adv. Mater.*, 2017, **29**, 1606109.

120 C. Liu, S. Cao and M. Yoshio, *Adv. Funct. Mater.*, 2023, **33**, 2300538.

121 S. Y. Kim, Y. Kim, C. Cho, H. Choi, H. W. Park, D. Lee, E. Heo, S. Park, H. Lee and D. H. Kim, *ACS Appl. Mater. Interfaces*, 2019, **11**, 29350–29359.

122 M. Konyo, S. Tadokoro, A. Yoshida and N. Saiwaki, *2005 IEEE/RSJ International Conference on Intelligent Robots and Systems*, 2005, pp. 3965–3971.

123 G.-H. Feng and S.-Y. Hou, *2015 Transducers - 2015 18th International Conference on Solid-State Sensors, Actuators and Microsystems (TRANSDUCERS)*, 2015, pp. 835–838.

124 M. Konyo, K. Akazawa, S. Tadokoro and T. Takamori, *J. Robot. Mechatronics*, 2003, **15**, 219–226.

125 M. Konyo, K. Akazawa, S. Tadokoro and T. Takamori, Proceedings 2003 IEEE/RSJ International Conference on Intelligent Robots and Systems (IROS 2003) (Cat. No. 03CH37453), 2003, vol. 4, pp. 3744–3750 vol. 3.

126 G.-H. Feng and S.-Y. Hou, *Sens. Actuators, A*, 2018, **275**, 137–147.

127 K. Fukuda, T. Sekitani, U. Zschieschang, H. Klauk, K. Kuribara, T. Yokota, T. Sugino, K. Asaka, M. Ikeda, H. Kuwabara, T. Yamamoto, K. Takimiya, T. Fukushima, T. Aida, M. Takamiya, T. Sakurai and T. Someya, *Adv. Funct. Mater.*, 2011, **21**, 4019–4027.

128 M. Konyo, S. Tadokoro and T. Takamori, *Proceedings 2000 ICRA. Millennium Conference. IEEE International Conference on Robotics and Automation. Symposia Proceedings (Cat. No. 00CH37065)*, 2000, vol. 4, pp. 3416–3421.

129 P. Rinne, I. Põldsalu, U. Johanson, T. Tamm, K. Põhako-Esko, A. Punning, D. van den Ende and A. Aabloo, *Smart Mater. Struct.*, 2019, **28**, 074002.

130 J. Barramba, J. Silva and P. J. Costa Branco, *Sens. Actuators, A*, 2007, **140**, 232–238.

131 P. Rinne, I. Põldsalu, V. Zadin, U. Johanson, T. Tamm, K. Põhako-Esko, A. Punning, D. van den Ende and A. Aabloo, *Sci. Rep.*, 2022, **12**, 21589.

132 P. Jaakson, A. Aabloo and T. Tamm, *Electroactive Polymer Actuators and Devices (EAPAD) 2016*, SPIE, 2016, vol. 9798, pp. 402–409.

133 S. Ebrahimi Takalloo, A. Fannir, G. T. M. Nguyen, C. Plesse, F. Vidal and J. D. W. Madden, *Robotics*, 2019, **8**, 60.

134 S. Naficy, N. Stoboi, P. G. Whitten, G. M. Spinks and G. G. Wallace, *Smart Mater. Struct.*, 2013, **22**, 075005.

135 G. Bubak, D. Gendron, L. Ceseracciu, A. Ansaldo and D. Ricci, *ACS Appl. Mater. Interfaces*, 2015, **7**, 15542–15550.

136 S. J. Kim, I. T. Lee, H.-Y. Lee and Y. H. Kim, *Smart Mater. Struct.*, 2006, **15**, 1540.

3528 | *Chem. Soc. Rev.*, 2024, **53**, 3485–3535

This journal is © The Royal Society of Chemistry 2024

137 W. Peng, Y. Zhang, J. Gao, Y. Wang, Y. Chen and Y. Zhou, *Sens. Actuators, A*, 2019, **299**, 111613.

138 Y. Dong, K.-W. Yeung, C.-Y. Tang, W.-C. Law, G. C.-P. Tsui and X. Xie, *Nanotechnol. Rev.*, 2021, **10**, 99–116.

139 F. Yu, J.-H. Ciou, S. Chen, W. C. Poh, J. Chen, J. Chen, K. Haruethai, J. Lv, D. Gao and P. S. Lee, *Nat. Commun.*, 2022, **13**, 390.

140 S. Roy, J. Kim, M. Kotal, R. Tabassian, K. J. Kim and I.-K. Oh, *Adv. Funct. Mater.*, 2019, **29**, 1900161.

141 Y.-X. Shi, Y. Wu, S.-Q. Wang, Y.-Y. Zhao, T. Li, X.-Q. Yang and T. Zhang, *J. Am. Chem. Soc.*, 2021, **143**, 4017–4023.

142 M. Garai, M. Mahato, S. Nam, E. Kim, D. Seo, Y. Lee, V. H. Nguyen, S. Oh, P. Sambyal, H. Yoo, A. K. Taseer, S. A. Syed, H. Han, C. W. Ahn, J. Kim and I.-K. Oh, *Adv. Funct. Mater.*, 2023, **33**, 2212252.

143 Z. Chen and X. Tan, *Sens. Actuators, A*, 2010, **157**, 246–257.

144 J.-H. Jeon and I.-K. Oh, *Thin Solid Films*, 2009, **517**, 5288–5292.

145 J.-H. Jeon, S.-W. Yeom and I.-K. Oh, *Composites, Part A*, 2008, **39**, 588–596.

146 J. D. Carrico, N. W. Traeden, M. Aureli and K. K. Leang, *Smart Mater. Struct.*, 2015, **24**, 125021.

147 J. D. Carrico, T. Hermans, K. J. Kim and K. K. Leang, *Sci. Rep.*, 2019, **9**, 17482.

148 Y. Wang, Y. Liang, A. Bansode, X. Lou, X. Zhang, B. S. Beckingham and M. L. Auad, *Macromol. Mater. Eng.*, 2023, **308**, 2200440.

149 C. Bian, Z. Zhu, W. Bai, H. Chen and Y. Li, *Smart Mater. Struct.*, 2020, **29**, 035014.

150 K. Jung, J. Nam and H. Choi, *Sens. Actuators, A*, 2003, **107**, 183–192.

151 G. Wu, X. Wu, Y. Xu, H. Cheng, J. Meng, Q. Yu, X. Shi, K. Zhang, W. Chen and S. Chen, *Adv. Mater.*, 2019, **31**, 1806492.

152 C. Lu, Q. Huang and X. Chen, *J. Mater. Chem. A*, 2020, **8**, 9228–9238.

153 F. Wang, Q. Li, J.-O. Park, S. Zheng and E. Choi, *Adv. Funct. Mater.*, 2021, **31**, 2007749.

154 M. S. Xavier, C. D. Tawk, A. Zolfagharian, J. Pinskier, D. Howard, T. Young, J. Lai, S. M. Harrison, Y. K. Yong, M. Bodaghi and A. J. Fleming, *IEEE Access*, 2022, **10**, 59442–59485.

155 X. Wu, S.-H. Kim, H. Zhu, C.-H. Ji and M. G. Allen, *J. Microelectromech. Syst.*, 2012, **21**, 908–916.

156 A. Talhan, H. Kim and S. Jeon, *IEEE Access*, 2020, **8**, 957–966.

157 S. Kanjanapas, C. M. Nunez, S. R. Williams, A. M. Okamura and M. Luo, *IEEE Robot. Automation Lett.*, 2019, **4**, 1365–1371.

158 E. Doh, H. Lee, J. Park and K.-S. Yun, *2011 16th International Solid-State Sensors, Actuators and Microsystems Conference*, 2011, pp. 2418–2421.

159 K. Song, S. H. Kim, S. Jin, S. Kim, S. Lee, J.-S. Kim, J.-M. Park and Y. Cha, *Sci. Rep.*, 2019, **9**, 8988.

160 R. S. Diteesawat, T. Helps, M. Taghavi and J. Rossiter, *Sci. Robot.*, 2021, **6**, eabc3721.

161 R. H. Heisser, C. A. Aubin, O. Peretz, N. Kincaid, H. S. An, E. M. Fisher, S. Sobhani, P. Pepiot, A. D. Gat and R. F. Shepherd, *Proc. Natl. Acad. Sci. U. S. A.*, 2021, **118**, e2106553118.

162 V. Vallem, E. Roosa, T. Ledinh, S. R. Nadimi, A. Kiani and M. D. Dickey, *Soft Matter*, 2022, **18**, 9291–9298.

163 Q. He, Z. Wang, Y. Wang, A. Minori, M. T. Tolley and S. Cai, *Sci. Adv.*, 2019, **5**, eaax5746.

164 J. M. Boothby, J. C. Gagnon, E. McDowell, T. Van Volkenburg, L. Currano and Z. Xia, *Soft Robot.*, 2022, **9**, 154–162.

165 Y. Ji, Y. Y. Huang, R. Rungsawang and E. M. Terentjev, *Adv. Mater.*, 2010, **22**, 3436–3440.

166 N. Torras, K. E. Zinoviev, J. E. Marshall, E. M. Terentjev and J. Esteve, *Appl. Phys. Lett.*, 2011, **99**, 254102.

167 L. Yang, K. Setyowati, A. Li, S. Gong and J. Chen, *Adv. Mater.*, 2008, **20**, 2271–2275.

168 C. Li, Y. Liu, X. Huang and H. Jiang, *Adv. Funct. Mater.*, 2012, **22**, 5166–5174.

169 Z. Cheng, T. Wang, X. Li, Y. Zhang and H. Yu, *ACS Appl. Mater. Interfaces*, 2015, **7**, 27494–27501.

170 Y. Yang, W. Zhan, R. Peng, C. He, X. Pang, D. Shi, T. Jiang and Z. Lin, *Adv. Mater.*, 2015, **27**, 6376–6381.

171 Y. Wang, A. Dang, Z. Zhang, R. Yin, Y. Gao, L. Feng and S. Yang, *Adv. Mater.*, 2020, **32**, 2004270.

172 J. Xu, S. Chen, W. Yang, B. Qin, X. Wang, Y. Wang, M. Cao, Y. Gao, C. Li and Y. Dong, *Soft Matter*, 2019, **15**, 6116–6126.

173 J. Zhang, D. Sun, B. Zhang, Q. Sun, Y. Zhang, S. Liu, Y. Wang, C. Liu, J. Chen, J. Chen, Y. Song and X. Liu, *Mater. Horiz.*, 2022, **9**, 1045–1056.

174 Y. Zhai, Z. Wang, K.-S. Kwon, S. Cai, D. J. Lipomi and T. N. Ng, *Adv. Mater.*, 2021, **33**, 2002541.

175 A. Lendlein and S. Kelch, *Angew. Chem., Int. Ed.*, 2002, **41**, 2034–2057.

176 Y. Xia, Y. He, F. Zhang, Y. Liu and J. Leng, *Adv. Mater.*, 2021, **33**, 2000713.

177 A. Lendlein and O. E. C. Gould, *Nat. Rev. Mater.*, 2019, **4**, 116–133.

178 N. Besse, S. Rosset, J. J. Zarate and H. Shea, *Adv. Mater. Technol.*, 2017, **2**, 1700102.

179 X. Niu, X. Yang, P. Brochu, H. Stoyanov, S. Yun, Z. Yu and Q. Pei, *Adv. Mater.*, 2012, **24**, 6513–6519.

180 C. J. Camargo, H. Campanella, J. E. Marshall, N. Torras, K. Zinoviev, E. M. Terentjev and J. Esteve, *Macromol. Rapid Commun.*, 2011, **32**, 1953–1959.

181 C. J. Camargo, H. Campanella, J. E. Marshall, N. Torras, K. Zinoviev, E. M. Terentjev and J. Esteve, *J. Micromech. Microeng.*, 2012, **22**, 075009.

182 N. Torras, K. E. Zinoviev, C. J. Camargo, E. M. Campo, H. Campanella, J. Esteve, J. E. Marshall, E. M. Terentjev, M. Omastová, I. Krupa, P. Teplický, B. Mamojka, P. Bruns, B. Roeder, M. Vallribera, R. Malet, S. Zuffanelli, V. Soler, J. Roig, N. Walker, D. Wenn, F. Vossen and F. M. H. Crompvoets, *Sens. Actuators, A*, 2014, **208**, 104–112.

183 N. Besse, S. Rosset, J. J. Zárate, E. Ferrari, L. Brayda and H. Shea, *IEEE Trans. Haptics*, 2018, **11**, 30–38.

This journal is © The Royal Society of Chemistry 2024

Chem. Soc. Rev., 2024, **53**, 3485–3535 | **3529**

184 T. Hu, S. Xuan, Y. Gao, Q. Shu, Z. Xu, S. Sun, J. Li and X. Gong, *Adv. Mater. Technol.*, 2022, **7**, 2100777.

185 Z.-Y. Xu, L. Li, L.-Y. Shi, K.-K. Yang and Y.-Z. Wang, *Macromolecules*, 2022, **55**, 5104–5114.

186 Y. Wu, J. Hu, J. Han, Y. Zhu, H. Huang, J. Li and B. Tang, *J. Mater. Chem. A*, 2014, **2**, 18816–18822.

187 S. Chen, J. Hu and H. Zhuo, *Compos. Sci. Technol.*, 2010, **70**, 1437–1443.

188 S. W. Ula, N. A. Traugutt, R. H. Volpe, R. R. Patel, K. Yu and C. M. Yakacki, *Liquid Cryst. Rev.*, 2018, **6**, 78–107.

189 K. M. Herbert, H. E. Fowler, J. M. McCracken, K. R. Schlafmann, J. A. Koch and T. J. White, *Nat. Rev. Mater.*, 2022, **7**, 23–38.

190 T. J. White and D. J. Broer, *Nat. Mater.*, 2015, **14**, 1087–1098.

191 H. Wermter and H. Finkelmann, *e-Polymers*, 2001, **1**, 013.

192 N. Torras, K. E. Zinoviev, J. Esteve and A. Sánchez-Ferrer, *J. Mater. Chem. C*, 2013, **1**, 5183–5190.

193 Z. Pei, Y. Yang, Q. Chen, E. M. Terentjev, Y. Wei and Y. Ji, *Nat. Mater*, 2014, **13**, 36–41.

194 G. E. Bauman, J. M. McCracken and T. J. White, *Angew. Chem., Int. Ed.*, 2022, **61**, e202202577.

195 J. C. Breger, C. Yoon, R. Xiao, H. R. Kwag, M. O. Wang, J. P. Fisher, T. D. Nguyen and D. H. Gracias, *ACS Appl. Mater. Interfaces*, 2015, **7**, 3398–3405.

196 X. Hu, Z. Ge, X. Wang, N. Jiao, S. Tung and L. Liu, *Composites, Part B*, 2022, **228**, 109451.

197 A. S. Gladman, E. A. Matsumoto, R. G. Nuzzo, L. Mahadevan and J. A. Lewis, *Nat. Mater.*, 2016, **15**, 413–418.

198 J. Liu, L. Jiang, S. He, J. Zhang and W. Shao, *Chem. Eng. J.*, 2022, **433**, 133496.

199 A. Richter and G. Paschew, *Adv. Mater.*, 2009, **21**, 979–983.

200 R. B. Yilmaz, Y. Chaabane and V. Mansard, *ACS Appl. Mater. Interfaces*, 2023, **15**, 7340–7352.

201 M. Shikida, T. Imamura, S. Ukai, T. Miyaji and K. Sato, *J. Micromech. Microeng.*, 2008, **18**, 065012.

202 M. Blander and J. L. Katz, *AIChE J.*, 1975, **21**, 833–848.

203 H. Yu, Z. Li, Y. Tao, J. Sha and Y. Chen, *J. Phys. Chem. C*, 2019, **123**, 3482–3490.

204 Y. Kim and X. Zhao, *Chem. Rev.*, 2022, **122**, 5317–5364.

205 H. Song, H. Lee, J. Lee, J. K. Choe, S. Lee, J. Y. Yi, S. Park, J.-W. Yoo, M. S. Kwon and J. Kim, *Nano Lett.*, 2020, **20**, 5185–5192.

206 W. Hu, G. Z. Lum, M. Mastrangeli and M. Sitti, *Nature*, 2018, **554**, 81–85.

207 A. S. Algamili, M. H. M. D. Khir, J. O. Dennis, A. Y. Ahmed, S. S. Alabsi, S. S. Ba Hashwan and M. M. Junaid, *Nanoscale Res. Lett.*, 2021, **16**, 16.

208 Y. Huang, K. Yao, J. Li, D. Li, H. Jia, Y. Liu, C. K. Yiu, W. Park and X. Yu, *Mater. Today Phys.*, 2022, **22**, 100602.

209 Y. Guo, Q. Tong, P. Zhao, Y. Zhang and D. Wang, *IEEE Trans. Ind. Electron.*, 2023, **70**, 10344–10352.

210 F. Pece, J. J. Zarate, V. Vechev, N. Besse, O. Gudozhnik, H. Shea and O. Hilliges, *Proceedings of the 30th Annual ACM Symposium on User Interface Software and Technology*, ACM, Québec City QC Canada, 2017, pp. 143–154.

211 X. Yu, Z. Xie, Y. Yu, J. Lee, A. Vazquez-Guardado, H. Luan, J. Ruban, X. Ning, A. Akhtar, D. Li, B. Ji, Y. Liu, R. Sun, J. Cao, Q. Huo, Y. Zhong, C. Lee, S. Kim, P. Gutruf, C. Zhang, Y. Xue, Q. Guo, A. Chempakasseril, P. Tian, W. Lu, J. Jeong, Y. Yu, J. Cornman, C. Tan, B. Kim, K. Lee, X. Feng, Y. Huang and J. A. Rogers, *Nature*, 2019, **575**, 473–479.

212 D. Li, J. He, Z. Song, K. Yao, M. Wu, H. Fu, Y. Liu, Z. Gao, J. Zhou, L. Wei, Z. Zhang, Y. Dai, Z. Xie and X. Yu, *Microsyst. Nanoeng.*, 2021, **7**, 1–9.

213 D. Li, J. Zhou, K. Yao, S. Liu, J. He, J. Su, Q. Qu, Y. Gao, Z. Song, C. Yiu, C. Sha, Z. Sun, B. Zhang, J. Li, L. Huang, C. Xu, T. H. Wong, X. Huang, J. Li, R. Ye, L. Wei, Z. Zhang, X. Guo, Y. Dai, Z. Xie and X. Yu, *Sci. Adv.*, 2022, **8**, eade2450.

214 Z. Wu, S. Zhang, A. Vorobyev, K. Gamstedt, K. Wu, C. Guo and S. H. Jeong, *Mater. Today Phys.*, 2018, **4**, 28–35.

215 A. B. M. T. Haque, D. Hwang and M. D. Bartlett, *Adv. Mater. Technol.*, 2022, **7**, 2101241.

216 N. D. Kohls, N. Colonnese, Y. C. Mazumdar and P. Agarwal, *IEEE/ASME Trans. Mechatronics*, 2023, **28**, 1948–1956.

217 T. N. Do, H. Phan, T.-Q. Nguyen and Y. Visell, *Adv. Funct. Mater.*, 2018, **28**, 1800244.

218 M. Vural, M. Mohammadi, L. Seufert, S. Han, X. Crispin, A. Fridberger, M. Berggren and K. Tybrandt, *ACS Appl. Mater. Interfaces*, 2023, **15**, 30653–30662.

219 H. Ishizuka and N. Miki, *Jpn. J. Appl. Phys.*, 2017, **56**, 06GN19.

220 L. Cestarollo, S. Smolenski and A. El-Ghazaly, *ACS Appl. Mater. Interfaces*, 2022, **14**, 19002–19011.

221 G. Mao, M. Drack, M. Karami-Mosammam, D. Wirthl, T. Stockinger, R. Schwödiauer and M. Kaltenbrunner, *Sci. Adv.*, 2020, **6**, eabc0251.

222 N. D. Kohls, R. Balak, B. P. Ruddy and Y. C. Mazumdar, *Soft Robot.*, 2023, **10**, 912–922.

223 N. Kohls, I. Abdeally, B. P. Ruddy and Y. C. Mazumdar, *ASME Lett. Dyn. Systems Control.*, 2021, **1**, 031011.

224 H. Ishizuka, T. Nakadegawa and N. Miki, *2015 International Conference on Electronics Packaging and iMAPS All Asia Conference (ICEP-IAAC)*, 2015, pp. 409–412.

225 A. Alkhalaf, A. Hooshiar and J. Dargahi, *Composites, Part B*, 2020, **190**, 107888.

226 G. Zhang, Y. Li, H. Wang and J. Wang, *Front. Mater.*, 2019, **6**, 56.

227 S. M. A. Tarmizi, N. A. Nordin, S. A. Mazlan, N. Mohamad, H. A. Rahman, S. A. A. Aziz, N. Nazmi and M. A. Azmi, *J. Mater. Res. Technol.*, 2020, **9**, 15566–15574.

228 L. A. Makarova, Yu. A. Alekhina, A. S. Omelyanchik, D. Peddis, V. V. Spiridonov, V. V. Rodionova and N. S. Perov, *J. Magn. Magn. Mater.*, 2019, **485**, 413–418.

229 J. S. Kumar, P. S. Paul, G. Raghunathan and D. G. Alex, *Int. J. Mech. Mater. Eng.*, 2019, **14**, 13.

230 Y. Li, J. Li, W. Li and H. Du, *Smart Mater. Struct.*, 2014, **23**, 123001.

231 A. K. Bastola, M. Paudel, L. Li and W. Li, *Smart Mater. Struct.*, 2020, **29**, 123002.

3530 | *Chem. Soc. Rev.*, 2024, **53**, 3485–3535

This journal is © The Royal Society of Chemistry 2024

232 R. A. Bilodeau and R. K. Kramer, *Front. Robot. AI*, 2017, **4**, 48.

233 Y. Zhang, H. Khanbareh, J. Roscow, M. Pan, C. Bowen and C. Wan, *Matter*, 2020, **3**, 989–1008.

234 S. Bonardd, M. Nandi, J. I. Hernández García, B. Maiti, A. Abramov and D. Díaz Díaz, *Chem. Rev.*, 2023, **123**, 736–810.

235 S. Utrera-Barrios, R. Verdejo, M. A. López-Manchado and M. H. Santana, *Mater. Horiz.*, 2020, **7**, 2882–2902.

236 B. J. Blaiszik, S. L. B. Kramer, S. C. Olugebefola, J. S. Moore, N. R. Sottos and S. R. White, *Annu. Rev. Mater. Res.*, 2010, **40**, 179–211.

237 S. Samanta, S. Kim, T. Saito and A. P. Sokolov, *J. Phys. Chem. B*, 2021, **125**, 9389–9401.

238 Y. Yang and M. W. Urban, *Chem. Soc. Rev.*, 2013, **42**, 7446–7467.

239 Y. Yang and M. W. Urban, *Adv. Mater. Interfaces*, 2018, **5**, 1800384.

240 Y. Yang, X. Ding and M. W. Urban, *Prog. Polym. Sci.*, 2015, **49–50**, 34–59.

241 P. Chakma and D. Konkolewicz, *Angew. Chem., Int. Ed.*, 2019, **58**, 9682–9695.

242 A. Pena-Francesch, H. Jung, M. C. Demirel and M. Sitti, *Nat. Mater.*, 2020, **19**, 1230–1235.

243 Y. Zhang, M. Li, B. Qin, L. Chen, Y. Liu, X. Zhang and C. Wang, *Chem. Mater.*, 2020, **32**, 6310–6317.

244 L. Duan, J.-C. Lai, C.-H. Li and J.-L. Zuo, *ACS Appl. Mater. Interfaces*, 2020, **12**, 44137–44146.

245 H. Sun, X. Liu, S. Liu, B. Yu, N. Ning, M. Tian and L. Zhang, *Chem. Eng. J.*, 2020, **384**, 123242.

246 M. W. M. Tan, G. Thangavel and P. S. Lee, *Adv. Funct. Mater.*, 2021, **31**, 2103097.

247 C. Ellingford, R. Zhang, A. M. Wemyss, Y. Zhang, O. B. Brown, H. Zhou, P. Keogh, C. Bowen and C. Wan, *ACS Appl. Mater. Interfaces*, 2020, **12**, 7595–7604.

248 H. Guo, C. Liang, T.-P. Ruoko, H. Meteling, B. Peng, H. Zeng and A. Priimagi, *Angew. Chem., Int. Ed.*, 2023, **62**, e202309402.

249 B. Ni, H.-L. Xie, J. Tang, H.-L. Zhang and E.-Q. Chen, *Chem. Commun.*, 2016, **52**, 10257–10260.

250 L. Ding, S. Zhang, Q. Wang, Y. Wang, S. Xuan, X. Gong and D. Zhang, *Compos. Sci. Technol.*, 2022, **223**, 109430.

251 S. Terryn, J. Brancart, D. Lefeber, G. Van Assche and B. Vanderborght, *Sci. Robot.*, 2017, **2**, eaan4268.

252 A. Costa Cornellà, S. K. Tabrizian, P. Ferrentino, E. Roels, S. Terryn, B. Vanderborght, G. Van Assche and J. Brancart, *ACS Sustainable Chem. Eng.*, 2023, **11**, 3437–3450.

253 Z. Wang, H. Tian, Q. He and S. Cai, *ACS Appl. Mater. Interfaces*, 2017, **9**, 33119–33128.

254 L. Chen, H. K. Bisoyi, Y. Huang, S. Huang, M. Wang, H. Yang and Q. Li, *Angew. Chem., Int. Ed.*, 2021, **60**, 16394–16398.

255 X. Qi, C. Pan, L. Zhang and D. Yue, *ACS Appl. Mater. Interfaces*, 2023, **15**, 3497–3506.

256 R.-P. Nie, H. Lin, Y. Li, H.-D. Huang, D.-X. Yan, K. Dai, J. Lei and Z.-M. Li, *Chem. Eng. J.*, 2022, **439**, 135683.

257 J. Kang, D. Son, G.-J. N. Wang, Y. Liu, J. Lopez, Y. Kim, J. Y. Oh, T. Katsumata, J. Mun, Y. Lee, L. Jin, J. B.-H. Tok and Z. Bao, *Adv. Mater.*, 2018, **30**, 1706846.

258 C.-H. Li, C. Wang, C. Keplinger, J.-L. Zuo, L. Jin, Y. Sun, P. Zheng, Y. Cao, F. Lissel, C. Linder, X.-Z. You and Z. Bao, *Nat. Chem.*, 2016, **8**, 618–624.

259 Y. Wang, Q. Guo, G. Su, J. Cao, J. Liu and X. Zhang, *Adv. Funct. Mater.*, 2019, **29**, 1906198.

260 S. Nomimura, M. Osaki, J. Park, R. Ikura, Y. Takashima, H. Yamaguchi and A. Harada, *Macromolecules*, 2019, **52**, 2659–2668.

261 J. Xu, X. Ren and G. Gao, *Polymer*, 2018, **150**, 194–203.

262 H. Wang, M. W. M. Tan, W. C. Poh, D. Gao, W. Wu and P. S. Lee, *J. Mater. Chem. A*, 2023, **11**, 14159–14168.

263 J. Dai, Z. Wang, Z. Wu, Z. Fang, S. Heliu, W. T. Yang, Y. Bai and X. Zhang, *ACS Appl. Polym. Mater.*, 2023, **5**, 2575–2582.

264 H. Guo, Y. Han, W. Zhao, J. Yang and L. Zhang, *Nat. Commun.*, 2020, **11**, 2037.

265 Y. Cao, H. Wu, S. I. Allec, B. M. Wong, D.-S. Nguyen and C. Wang, *Adv. Mater.*, 2018, **30**, 1804602.

266 Z. Cheng, W. Feng, Y. Zhang, L. Sun, Y. Liu, L. Chen and C. Wang, *Adv. Mater.*, 2023, **35**, 2301005.

267 L. Liu, W. Zhang, N. Ning and L. Zhang, *Chem. Eng. J.*, 2019, **375**, 121993.

268 C. Ellingford, R. Zhang, A. M. Wemyss, C. Bowen, T. McNally, Ł. Figiel and C. Wan, *ACS Appl. Mater. Interfaces*, 2018, **10**, 38438–38448.

269 Y. Zhang, C. Ellingford, R. Zhang, J. Roscow, M. Hopkins, P. Keogh, T. McNally, C. Bowen and C. Wan, *Adv. Funct. Mater.*, 2019, **29**, 1808431.

270 H. Sun, X. Liu, S. Liu, B. Yu, N. Ning, M. Tian and L. Zhang, *J. Mater. Chem. A*, 2020, **8**, 23330–23343.

271 R.-P. Nie, W.-B. Tang, C. Chen, H.-D. Huang, Y. Li, K. Dai, J. Lei and Z.-M. Li, *J. Mater. Chem. C*, 2021, **9**, 12239–12247.

272 Y. Yao, N. Ning, L. Zhang, T. Nishi and M. Tian, *RSC Adv.*, 2015, **5**, 23719–23726.

273 X. Qiu, Q. Guo, Y. Wang, X. Huang, J. Cao, Z. Zheng and X. Zhang, *ACS Appl. Mater. Interfaces*, 2020, **12**, 41981–41990.

274 H. Hu, M. Nie, M. Galluzzi, X. Yu and X. Du, *Adv. Funct. Mater.*, 2023, **33**, 2304634.

275 Z. Liu, Y. Ma, Z. Zhang, Z. Shi and J. Gao, *Langmuir*, 2022, **38**, 4812–4819.

276 Z. Jiang, B. Diggle, I. C. G. Shackleford and L. A. Connal, *Adv. Mater.*, 2019, **31**, 1904956.

277 X. Luo, Y. Wu, M. Guo, X. Yang, L. Xie, J. Lai, Z. Li and H. Zhou, *J. Appl. Polym. Sci.*, 2021, **138**, 50827.

278 J. Xiong, G. Thangavel, J. Wang, X. Zhou and P. S. Lee, *Sci. Adv.*, 2020, **6**, eabb4246.

279 B. T. Worrell, M. K. McBride, G. B. Lyon, L. M. Cox, C. Wang, S. Mavila, C.-H. Lim, H. M. Coley, C. B. Musgrave, Y. Ding and C. N. Bowman, *Nat. Commun.*, 2018, **9**, 2804.

280 J. Ma, Y. Yang, C. Valenzuela, X. Zhang, L. Wang and W. Feng, *Angew. Chem., Int. Ed.*, 2022, **61**, e202116219.

281 S. Terryn, J. Brancart, E. Roels, G. Van Assche and B. Vanderborght, *IEEE Robot. Automation Magazine*, 2020, **27**, 44–55.

This journal is © The Royal Society of Chemistry 2024

Chem. Soc. Rev., 2024, **53**, 3485–3535 | 3531

282 S. Terryn, G. Mathijssen, J. Brancart, D. Lefeber, G. V. Assche and B. Vanderborght, *Bioinspir. Biomim.*, 2015, **10**, 046007.

283 S. Terryn, J. Brancart, D. Lefeber, G. Van Assche and B. Vanderborght, *IEEE Robot. Automation Lett.*, 2018, **3**, 16–21.

284 S. Terryn, E. Roels, J. Brancart, G. Van Assche and B. Vanderborght, *Actuators*, 2020, **9**, 34.

285 E. Roels, S. Terryn, J. Brancart, G. Van Assche and B. Vanderborght, *2019 2nd IEEE International Conference on Soft Robotics (RoboSoft)*, 2019, pp. 316–321.

286 E. F. Gomez, S. V. Wanasinghe, A. E. Flynn, O. J. Dodo, J. L. Sparks, L. A. Baldwin, C. E. Tabor, M. F. Durstock, D. Konkolewicz and C. J. Thrasher, *ACS Appl. Mater. Interfaces*, 2021, **13**, 28870–28877.

287 J.-H. Lee, J. Bae, J. H. Hwang, M.-Y. Choi, Y. S. Kim, S. Park, J.-H. Na, D.-G. Kim and S. Ahn, *Adv. Funct. Mater.*, 2022, **32**, 2110360.

288 Y. Wu, Y. Wei and Y. Ji, *Polym. Chem.*, 2020, **11**, 5297–5320.

289 C. Valenzuela, Y. Chen, L. Wang and W. Feng, *Chem. – Eur. J.*, 2022, **28**, e202201957.

290 G. Das, H. Jo and S.-Y. Park, *Chem. Eng. J.*, 2023, **466**, 143368.

291 Y. Amamoto, H. Otsuka, A. Takahara and K. Matyjaszewski, *Adv. Mater.*, 2012, **24**, 3975–3980.

292 C. Choi, J. L. Self, Y. Okayama, A. E. Levi, M. Gerst, J. C. Speros, C. J. Hawker, J. Read de Alaniz and C. M. Bates, *J. Am. Chem. Soc.*, 2021, **143**, 9866–9871.

293 K. Imato, M. Nishihara, T. Kanehara, Y. Amamoto, A. Takahara and H. Otsuka, *Angew. Chem.*, 2012, **124**, 1164–1168.

294 H. Bai, Y. S. Kim and R. F. Shepherd, *Sci. Adv.*, 2022, **8**, eabq2104.

295 Z. Peng, Y. Shi, N. Chen, Y. Li and Q. Pei, *Adv. Funct. Mater.*, 2021, **31**, 2008321.

296 W. Yuan, L. B. Hu, Z. B. Yu, T. Lam, J. Biggs, S. M. Ha, D. J. Xi, B. Chen, M. K. Senesky, G. Grüner and Q. Pei, *Adv. Mater.*, 2008, **20**, 621–625.

297 H. Stoyanov, P. Brochu, X. Niu, C. Lai, S. Yun and Q. Pei, *RSC Adv.*, 2013, **3**, 2272–2278.

298 W. Yuan, P. Brochu, S. M. Ha and Q. Pei, *Sens. Actuators, A*, 2009, **155**, 278–284.

299 J. Xu, Y. Dong, Z. Jiang, L. Tang, X. Chen, Z. Yao and K. Cao, *Composites, Part A*, 2021, **149**, 106519.

300 S. Hunt, T. G. McKay and I. A. Anderson, *Appl. Phys. Lett.*, 2014, **104**, 113701.

301 S. K. Mitchell, X. Wang, E. Acome, T. Martin, K. Ly, N. Kellaris, V. G. Venkata and C. Keplinger, *Adv. Sci.*, 2019, **6**, 1900178.

302 W. Tang, C. Zhang, Y. Zhong, P. Zhu, Y. Hu, Z. Jiao, X. Wei, G. Lu, J. Wang, Y. Liang, Y. Lin, W. Wang, H. Yang and J. Zou, *Nat. Commun.*, 2021, **12**, 2247.

303 J. Huang, Z. Gong and Y. Chen, *Polymer*, 2022, **242**, 124569.

304 W. Alabiso, T. M. Hron, D. Reisinger, D. Bautista-Anguís and S. Schlögl, *Polym. Chem.*, 2021, **12**, 5704–5714.

305 Z. P. Zhang, M. Z. Rong and M. Q. Zhang, *Prog. Polym. Sci.*, 2023, **144**, 101724.

306 L. F. Fan, M. Z. Rong, M. Q. Zhang and X. D. Chen, *ACS Appl. Mater. Interfaces*, 2018, **10**, 38538–38546.

307 L. F. Fan, M. Z. Rong, M. Q. Zhang and X. D. Chen, *Macromol. Rapid Commun.*, 2017, **38**, 1700124.

308 R. Xu, G. S. Cañón Bermúdez, O. V. Pylypovskyi, O. M. Volkov, E. S. Oliveros Mata, Y. Zabila, R. Illing, P. Makushko, P. Milkin, L. Ionov, J. Fassbender and D. Makarov, *Nat. Commun.*, 2022, **13**, 6587.

309 K. Cerdan, G. Van Assche, P. van Puyvelde and J. Brancart, *Polymer*, 2020, **204**, 122819.

310 Y. Huang, Y. Huang, M. Zhu, W. Meng, Z. Pei, C. Liu, H. Hu and C. Zhi, Magnetic-Assisted, Self-Healable, Yarn-Based Supercapacitor, DOI: **10.1021/acsnano.5b01602**, (accessed July 27, 2023).

311 D. Garcia-Gonzalez, T. Ter-Yesayants, M. A. Moreno-Mateos and M. L. Lopez-Donaire, *Composites, Part B*, 2023, **248**, 110357.

312 C. B. Cooper, S. E. Root, L. Michalek, S. Wu, J.-C. Lai, M. Khatib, S. T. Oyakhire, R. Zhao, J. Qin and Z. Bao, *Science*, 2023, **380**, 935–941.

313 H. Wang, Y. Yang, M. Zhang, Q. Wang, K. Xia, Z. Yin, Y. Wei, Y. Ji and Y. Zhang, *ACS Appl. Mater. Interfaces*, 2020, **12**, 14315–14322.

314 C. Xu, B. Ma, S. Yuan, C. Zhao and H. Liu, *Adv. Electron. Mater.*, 2020, **6**, 1900721.

315 S. Kashef Tabrizian, S. Terryn, A. C. Cornellà, J. Brancart, J. Legrand, G. Van Assche and B. Vanderborght, *Sci. Rep.*, 2023, **13**, 8820.

316 J. Orellana, I. Moreno-Villoslada, R. K. Bose, F. Picchioni, M. E. Flores and R. Araya-Hermosilla, *Polymers*, 2021, **13**, 649.

317 S. K. Tabrizian, F. Sahraeeazartamar, J. Brancart, E. Roels, P. Ferrentino, J. Legrand, G. Van Assche, B. Vanderborght and S. Terryn, *IEEE Robot. Automation Lett.*, 2022, **7**, 4574–4581.

318 J. Liu, L. Zhang, N. Wang, H. Zhao and C. Li, *Nano Energy*, 2022, **96**, 107108.

319 P. Mazurek, S. Vudayagiri and A. Ladegaard Skov, *Chem. Soc. Rev.*, 2019, **48**, 1448–1464.

320 S. Zakaria, F. B. Madsen and A. L. Skov, *Polym.-Plast. Technol. Eng.*, 2017, **56**, 83–95.

321 C. Chen, Z. Wang and Z. Suo, *Extreme Mech. Lett.*, 2017, **10**, 50–57.

322 X. Zhao, *Proc. Natl. Acad. Sci. U. S. A.*, 2017, **114**, 8138–8140.

323 T. Nakajima, *Polym. J.*, 2017, **49**, 477–485.

324 G. E. Fantner, E. Oroudjev, G. Schitter, L. S. Golde, P. Thurner, M. M. Finch, P. Turner, T. Gutsmann, D. E. Morse, H. Hansma and P. K. Hansma, *Biophys. J.*, 2006, **90**, 1411–1418.

325 X. Wu, J. Wang, J. Huang and S. Yang, *ACS Appl. Mater. Interfaces*, 2019, **11**, 7387–7396.

326 L.-J. Yin, Y. Zhao, J. Zhu, M. Yang, H. Zhao, J.-Y. Pei, S.-L. Zhong and Z.-M. Dang, *Nat. Commun.*, 2021, **12**, 4517.

327 Z. Chen, Y. Xiao, J. Fang, J. He, Y. Gao, J. Zhao, X. Gao and Y. Luo, *Chem. Eng. J.*, 2021, **405**, 126634.

328 L. Jiang, C. Liu, K. Mayumi, K. Kato, H. Yokoyama and K. Ito, *Chem. Mater.*, 2018, **30**, 5013–5019.

3532 | *Chem. Soc. Rev.*, 2024, **53**, 3485–3535

This journal is © The Royal Society of Chemistry 2024

329 C. Liu, H. Kadono, K. Mayumi, K. Kato, H. Yokoyama and K. Ito, *ACS Macro Lett.*, 2017, **6**, 1409–1413.

330 Y. Noda, Y. Hayashi and K. Ito, *J. Appl. Polym. Sci.*, 2014, **131**, 40509.

331 K. Mayumi, C. Liu, Y. Yasuda and K. Ito, *Gels*, 2021, **7**, 91.

332 R. Du, T. Bao, T. Zhu, J. Zhang, X. Huang, Q. Jin, M. Xin, L. Pan, Q. Zhang and X. Jia, *Adv. Funct. Mater.*, 2023, **33**, 2212888.

333 S. Choi, B. Kim, S. Park, J.-H. Seo and S. Ahn, *ACS Appl. Mater. Interfaces*, 2022, **14**, 32486–32496.

334 Y. Wang, X. Li, Y. Pan, Z. Zheng, X. Ding and Y. Peng, *RSC Adv.*, 2014, **4**, 17156–17160.

335 R. Wu, J. Lai, Y. Pan, Z. Zheng and X. Ding, *Soft Matter*, 2018, **14**, 4558–4568.

336 J. Shintake, K. Matsuno, S. Kumegawa, K. Baba and H. Takeuchi, *Smart Mater. Struct.*, 2022, **31**, 025028.

337 Z. Wang, C. Xiang, X. Yao, P. Le Floch, J. Mendez and Z. Suo, *Proc. Natl. Acad. Sci. U. S. A.*, 2019, **116**, 5967–5972.

338 G. Zhang, T. Yin, G. Nian and Z. Suo, *Extreme Mech. Lett.*, 2021, **48**, 101434.

339 C. Xiang, Z. Wang, C. Yang, X. Yao, Y. Wang and Z. Suo, *Mater. Today*, 2020, **34**, 7–16.

340 D. Sun, Y. Gao, Y. Zhou, M. Yang, J. Hu, T. Lu and T. Wang, *ACS Appl. Mater. Interfaces*, 2022, **14**, 49389–49397.

341 J. Xu, Y. Li, T. Liu, D. Wang, F. Sun, P. Hu, L. Wang, J. Chen, X. Wang, B. Yao and J. Fu, *Adv. Mater.*, 2023, **35**, 2300937.

342 M. Hua, S. Wu, Y. Ma, Y. Zhao, Z. Chen, I. Frenkel, J. Strzalka, H. Zhou, X. Zhu and X. He, *Nature*, 2021, **590**, 594–599.

343 S. Lin, X. Liu, J. Liu, H. Yuk, H.-C. Loh, G. A. Parada, C. Settens, J. Song, A. Masic, G. H. McKinley and X. Zhao, *Sci. Adv.*, 2019, **5**, eaau8528.

344 X. Li, K. Cui, T. L. Sun, L. Meng, C. Yu, L. Li, C. Creton, T. Kurokawa and J. P. Gong, *Proc. Natl. Acad. Sci. U. S. A.*, 2020, **117**, 7606–7612.

345 Y. Zheng, R. Kiyama, T. Matsuda, K. Cui, X. Li, W. Cui, Y. Guo, T. Nakajima, T. Kurokawa and J. P. Gong, *Chem. Mater.*, 2021, **33**, 3321–3334.

346 Y. Xiao, Y. Song, X. Cao, Z. Chen, X. Lu, J. Mao, Q. Rao, S. Fu, T. Li and Y. Luo, *Chem. Eng. J.*, 2022, **449**, 137734.

347 M. Tosaka, S. Murakami, S. Poompradub, S. Kohjiya, Y. Ikeda, S. Toki, I. Sics and B. S. Hsiao, *Macromolecules*, 2004, **37**, 3299–3309.

348 J. Kim, G. Zhang, M. Shi and Z. Suo, *Science*, 2021, **374**, 212–216.

349 R. Annapooranan, Y. Wang and S. Cai, *ACS Appl. Mater. Interfaces*, 2022, **14**, 2006–2014.

350 W. V. Mars and A. Fatemi, *Rubber Chem. Technol.*, 2004, **77**, 391–412.

351 M. Okui, A. Kojima, I. Hisamichi, S. Kuriyama, T. Kojima, T. Tsuji and T. Nakamura, *Polym. Test.*, 2023, **117**, 107800.

352 B. Ruellan, J.-B. Le Cam, I. Jeanneau, F. Canévet, F. Mortier and E. Robin, *Int. J. Fatigue*, 2019, **124**, 544–557.

353 N. Candau, R. Laghmach, L. Chazeau, J.-M. Chenal, C. Gauthier, T. Biben and E. Munch, *Eur. Polym. J.*, 2015, **64**, 244–252.

354 S. Amnuaypornsri, S. Toki, B. S. Hsiao and J. Sakdapipanich, *Polymer*, 2012, **53**, 3325–3330.

355 W. Xing, J. Wu, G. Huang, H. Li, M. Tang and X. Fu, *Polym. Int.*, 2014, **63**, 1674–1681.

356 X. Qi, L. Wang, Y. Zhang, M. Jia, L. Zhang and D. Yue, *Macromolecules*, 2022, **55**, 2758–2767.

357 C. Liu, N. Morimoto, L. Jiang, S. Kawahara, T. Noritomi, H. Yokoyama, K. Mayumi and K. Ito, *Science*, 2021, **372**, 1078–1081.

358 G. Nian, J. Kim, X. Bao and Z. Suo, *Adv. Mater.*, 2022, **34**, 2206577.

359 D. Zheng, S. Lin, J. Ni and X. Zhao, *Extreme Mech. Lett.*, 2022, **51**, 101608.

360 R. Annapooranan and S. Cai, *Eng. Fract. Mech.*, 2022, **269**, 108584.

361 L. A. Dissado and J. C. Fothergill, *Electrical Degradation and Breakdown in Polymers*, IET Digital Library, 1992.

362 J. Wei and L. Zhu, *Prog. Polym. Sci.*, 2020, **106**, 101254.

363 H. R. Choi, K. Jung, N. H. Chuc, M. Jung, I. Koo, J. Koo, J. Lee, J. Lee, J. Nam, M. Cho and Y. Lee, *Smart Structures and Materials 2005: Electroactive Polymer Actuators and Devices (EAPAD)*, SPIE, 2005, vol. 5759, pp. 283–291.

364 L. Yu and A. L. Skov, *Macromol. Rapid Commun.*, 2018, **39**, 1800383.

365 Y. Qiu, E. Zhang, R. Plamthottam and Q. Pei, *Acc. Chem. Res.*, 2019, **52**, 316–325.

366 S. M. Ha, W. Yuan, Q. Pei, R. Pelrine and S. Stanford, *Adv. Mater.*, 2006, **18**, 887–891.

367 X. Niu, H. Stoyanov, W. Hu, R. Leo, P. Brochu and Q. Pei, *J. Polym. Sci., Part B: Polym. Phys.*, 2013, **51**, 197–206.

368 Z. Chen, Z. Ma, J. Tang, Y. Xiao, J. Mao, Y. Cai, J. Zhao, X. Gao, T. Li and Y. Luo, *Mater. Horiz.*, 2021, **8**, 2834–2841.

369 S. M. Ha, W. Yuan, Q. Pei, R. Pelrine and S. Stanford, *Smart Mater. Struct.*, 2007, **16**, S280.

370 P. Brochu, H. Stoyanov, X. Niu and Q. Pei, *Smart Mater. Struct.*, 2013, **22**, 055022.

371 C. Tugui, G. Stiubianu, M. Iacob, C. Ursu, A. Bele, S. Vlad and M. Cazacu, *J. Mater. Chem. C*, 2015, **3**, 8963–8969.

372 M. Rahimabady, K. Yao, S. Arabnejad, L. Lu, V. P. W. Shim and D. Cheong Wun Chet, *Appl. Phys. Lett.*, 2012, **100**, 252907.

373 J. Claude, Y. Lu, K. Li and Q. Wang, *Chem. Mater.*, 2008, **20**, 2078–2080.

374 X. Zhang, M. Wissler, B. Jaehne, R. Breonnimann and G. Kovacs, *Smart Structures and Materials 2004: Electroactive Polymer Actuators and Devices (EAPAD)*, SPIE, 2004, vol. 5385, pp. 78–86.

375 Y. Xiao, Z. Chen, J. Mao, X. Cao, J. He, T. Yang, L. Chen, X. Yang, J. Zhao, T. Li and Y. Luo, *Macromol. Mater. Eng.*, 2021, **306**, 2000732.

376 A. H. A. Razak and A. L. Skov, *RSC Adv.*, 2017, **7**, 468–477.

377 A. H. A. Razak, L. Yu and A. Ladegaard Skov, *RSC Adv.*, 2017, 7, 17848–17856.

378 M. Dascalu, M. Iacob, C. Tugui, A. Bele, G.-T. Stiubianu, C. Racles and M. Cazacu, *J. Appl. Polym. Sci.*, 2021, **138**, 50161.

This journal is © The Royal Society of Chemistry 2024

Chem. Soc. Rev., 2024, **53**, 3485–3535 | **3533**

379 Z.-H. Shen, J.-J. Wang, Y. Lin, C.-W. Nan, L.-Q. Chen and Y. Shen, *Adv. Mater.*, 2018, **30**, 1704380.

380 Z. Wang, Z. Feng, H. Tang, J. Wang, Z. Cai, K. Bi and Y. Hao, *ACS Appl. Mater. Interfaces*, 2022, **14**, 42513–42521.

381 Y. Gong, D. Chen, J. Duan, X. Zhang, Y. Ma, C. Zhao and W. Yang, *J. Mater. Chem. C*, 2022, **10**, 13074–13083.

382 M. Guo, J. Jiang, Z. Shen, Y. Lin, C.-W. Nan and Y. Shen, *Mater. Today*, 2019, **29**, 49–67.

383 J. Zhang, F. Zhao, Y. Zuo, Y. Zhang, X. Chen, B. Li, N. Zhang, G. Niu, W. Ren and Z. Ye, *Compos. Sci. Technol.*, 2020, **200**, 108393.

384 Z. Zhou, H. Wang, Z. Zhu, H. Yang and Q. Zhang, *Colloids Surf., A*, 2019, **563**, 59–67.

385 X. Zhang, B.-W. Li, L. Dong, H. Liu, W. Chen, Y. Shen and C.-W. Nan, *Adv. Mater. Interfaces*, 2018, **5**, 1800096.

386 H. Luo, X. Zhou, C. Ellingford, Y. Zhang, S. Chen, K. Zhou, D. Zhang, C. R. Bowen and C. Wan, *Chem. Soc. Rev.*, 2019, **48**, 4424–4465.

387 M. Feng, Y. Feng, T. Zhang, J. Li, Q. Chen, Q. Chi and Q. Lei, *Adv. Sci.*, 2021, **8**, 2102221.

388 K. Yin, Z. Zhou, D. E. Schuele, M. Wolak, L. Zhu and E. Baer, *ACS Appl. Mater. Interfaces*, 2016, **8**, 13555–13566.

389 Y. Tian, J. Liu, W. Wu, X. Liang, M. Pan, C. Bowen, Y. Jiang, J. Sun, T. McNally, D. Wu, Y. Huang and C. Wan, *Adv. Intell. Syst.*, 2022, **4**, 2100239.

390 Z. Xu, S. Zheng, X. Wu, Z. Liu, R. Bao, W. Yang and M. Yang, *Composites, Part A*, 2019, **125**, 105527.

391 S. Pourazadi, A. Shagerdmootaab, H. Chan, M. Moallem and C. Menon, *Smart Mater. Struct.*, 2017, **26**, 115007.

392 C. Lanzerstorfer, *J. Environ. Sci. Health, Part A*, 2017, **52**, 770–777.

393 L. Mølhave, T. Schneider, S. K. Kjærgaard, L. Larsen, S. Norn and O. Jørgensen, *Atmos. Environ.*, 2000, **34**, 4767–4779.

394 T. Heckenthaler, S. Sadhujan, Y. Morgenstern, P. Natarajan, M. Bashouti and Y. Kaufman, *Langmuir*, 2019, **35**, 15526–15534.

395 V. A. Ganesh, H. K. Raut, A. S. Nair and S. Ramakrishna, *J. Mater. Chem.*, 2011, **21**, 16304–16322.

396 J. Wu, K. Yin, S. Xiao, Z. Wu, Z. Zhu, J.-A. Duan and J. He, *Adv. Mater. Interfaces*, 2021, **8**, 2001610.

397 S. Lin, B. Li, Y. Xu, A. A. Mehrizi and L. Chen, *Adv. Mater. Interfaces*, 2021, **8**, 2001441.

398 S. Ben, T. Zhou, H. Ma, J. Yao, Y. Ning, D. Tian, K. Liu and L. Jiang, *Adv. Sci.*, 2019, **6**, 1900834.

399 I. Oh, H. Cha, J. Chen, S. Chavan, H. Kong, N. Miljkovic and Y. Hu, *ACS Nano*, 2020, **14**, 13367–13379.

400 W. Feng, D. J. Broer and D. Liu, *Adv. Mater.*, 2018, **30**, 1704970.

401 C. Wang and Z. Guo, *Nanoscale*, 2020, **12**, 22398–22424.

402 T.-S. Wong, S. H. Kang, S. K. Y. Tang, E. J. Smythe, B. D. Hatton, A. Grinthal and J. Aizenberg, *Nature*, 2011, **477**, 443–447.

403 X. Chen, G. Wen and Z. Guo, *Mater. Horiz.*, 2020, **7**, 1697–1726.

404 Z. Gao, T. Xu, X. Miao, J. Lu, X. Zhu, Y. Song, G. Ren, Y. Jia and X. Li, *Surf. Interfaces*, 2021, **24**, 101022.

405 W. Gao, J. Wang, X. Zhang, L. Sun, Y. Chen and Y. Zhao, *Chem. Eng. J.*, 2020, **381**, 122612.

406 H. Qian, B. Liu, D. Wu, F. Zhang, X. Wang, L. Jin, J. Wang, D. Zhang and X. Li, *Surf. Coat. Technol.*, 2021, **406**, 126742.

407 Z. Tong, L. Song, S. Chen, J. Hu, Y. Hou, Q. Liu, Y. Ren, X. Zhan and Q. Zhang, *Adv. Funct. Mater.*, 2022, **32**, 2201290.

408 T. ul Islam, Y. Wang, I. Aggarwal, Z. Cui, H. E. Amirabadi, H. Garg, R. Kooi, B. B. Venkataramanachar, T. Wang, S. Zhang, P. R. Onck and J. M. J. den Toonder, *Lab Chip*, 2022, **22**, 1650–1679.

409 S. Peerlinck, E. Milana, E. De Smet, M. De Volder, D. Reynaerts and B. Gorissen, *Adv. Funct. Mater.*, 2023, **33**, 2300856.

410 J. H. Kim, S. M. Kang, B. J. Lee, H. Ko, W.-G. Bae, K. Y. Suh, M. K. Kwak and H. E. Jeong, *Sci. Rep.*, 2015, **5**, 17843.

411 R. J. H. van Raak, S. J. A. Houben, A. P. H. J. Schenning and D. J. Broer, *Adv. Mater. Technol.*, 2022, **7**, 2101619.

412 B. Dai, S. Li, T. Xu, Y. Wang, F. Zhang, Z. Gu and S. Wang, *ACS Appl. Mater. Interfaces*, 2018, **10**, 42979–42984.

413 E. Milana, R. Zhang, M. R. Vetrano, S. Peerlinck, M. De Volder, P. R. Onck, D. Reynaerts and B. Gorissen, *Sci. Adv.*, 2020, **6**, eabd2508.

414 S. Zhang, Y. Wang, P. R. Onck and J. M. J. den Toonder, *Adv. Funct. Mater.*, 2019, **29**, 1806434.

415 K. Sun, L. Shu, F. Jia, Z. Li and T. Wang, *Phys. Fluids*, 2022, **34**, 053319.

416 I. Oh, C. Keplinger, J. Cui, J. Chen, G. M. Whitesides, J. Aizenberg and Y. Hu, *Adv. Funct. Mater.*, 2018, **28**, 1802632.

417 H. Kim, J. Nam, M. Kim and K.-U. Kyung, *IEEE Robot. Automation Lett.*, 2021, **6**, 8245–8252.

418 Y. Gaffary and A. Lécuyer, *Front. ICT*, 2018, **5**, 5.

419 A. Grundstein, V. Meentemeyer and J. Dowd, *Int. J. Biometeorol.*, 2009, **53**, 255–261.

420 Z. Wang, C. Valenzuela, J. Wu, Y. Chen, L. Wang and W. Feng, *Small*, 2022, **18**, 2201597.

421 Y. Ye, Y. Zhang, Y. Chen, X. Han and F. Jiang, *Adv. Funct. Mater.*, 2020, **30**, 2003430.

422 S. Duan, S. Wu, M. Hua, D. Wu, Y. Yan, X. Zhu and X. He, *iScience*, 2021, **24**, 102989.

423 C. Wang, C. G. Wiener, P. I. Sepulveda-Medina, C. Ye, D. S. Simmons, R. Li, M. Fukuto, R. A. Weiss and B. D. Vogt, *Chem. Mater.*, 2019, **31**, 135–145.

424 W. Xie, J. Duan, H. Wang, J. Li, R. Liu, B. Yu, S. Liu and J. Zhou, *J. Mater. Chem. A*, 2018, **6**, 24114–24119.

425 H. Gao, Z. Zhao, Y. Cai, J. Zhou, W. Hua, L. Chen, L. Wang, J. Zhang, D. Han, M. Liu and L. Jiang, *Nat. Commun.*, 2017, **8**, 15911.

426 D. Gao, G. Thangavel, J. Lee, J. Lv, Y. Li, J.-H. Ciou, J. Xiong, T. Park and P. S. Lee, *Nat. Commun.*, 2023, **14**, 1990.

427 J. Lee, M. W. M. Tan, K. Parida, G. Thangavel, S. A. Park, T. Park and P. S. Lee, *Adv. Mater.*, 2020, **32**, 1906679.

428 D. Lou, C. Wang, Z. He, X. Sun, J. Luo and J. Li, *Chem. Commun.*, 2019, **55**, 8422–8425.

429 H. Na, Y.-W. Kang, C. S. Park, S. Jung, H.-Y. Kim and J.-Y. Sun, *Science*, 2022, **376**, 301–307.

3534 | *Chem. Soc. Rev.*, 2024, **53**, 3485–3535

This journal is © The Royal Society of Chemistry 2024

430 W. Pu, F. Wei, L. Yao and S. Xie, *J. Mater. Sci.*, 2022, **57**, 12202–12235.

431 H. Lin, J. Gong, H. Miao, R. Guterman, H. Song, Q. Zhao, J. W. C. Dunlop and J. Yuan, *ACS Appl. Mater. Interfaces*, 2017, **9**, 15148–15155.

432 J. Gong, H. Lin, J. W. C. Dunlop and J. Yuan, *Adv. Mater.*, 2017, **29**, 1605103.

433 J. Xiong, J. Chen and P. S. Lee, *Adv. Mater.*, 2021, **33**, 2002640.

434 D. Kim, S.-H. Kim, T. Kim, B. B. Kang, M. Lee, W. Park, S. Ku, D. Kim, J. Kwon, H. Lee, J. Bae, Y.-L. Park, K.-J. Cho and S. Jo, *PLoS One*, 2021, **16**, e0246102.

435 H. P. Anwar Ali, Z. Zhao, Y. J. Tan, W. Yao, Q. Li and B. C. K. Tee, *ACS Appl. Mater. Interfaces*, 2022, **14**, 52486–52498.

436 B. Shih, D. Shah, J. Li, T. G. Thuruthel, Y.-L. Park, F. Iida, Z. Bao, R. Kramer-Bottiglio and M. T. Tolley, *Sci. Robot.*, 2020, **5**, eaaz9239.

437 S. I. Rich, R. J. Wood and C. Majidi, *Nat. Electron.*, 2018, **1**, 102–112.

438 A. (Leo) Li, S. Lee, H. Shahsa and M. Duduta, *Soft Matter.*, 2022, **18**, 7123–7130.

439 M. C. den Hollander, C. A. Bakker and E. J. Hultink, *J. Ind. Ecol.*, 2017, **21**, 517–525.

440 F. Hartmann, M. Baumgartner and M. Kaltenbrunner, *Adv. Mater.*, 2021, **33**, 2004413.

441 B. von Vacano, H. Mangold, G. W. M. Vandermeulen, G. Battagliarin, M. Hofmann, J. Bean and A. Künkel, *Angew. Chem., Int. Ed.*, 2023, **62**, e202210823.

442 D. Gao, J. Lv and P. S. Lee, *Adv. Mater.*, 2022, **34**, 2105020.

This journal is © The Royal Society of Chemistry 2024

Chem. Soc. Rev., 2024, **53**, 3485–3535 | **3535**